Politecnico di Torino

ScuDo
Scuola di Dottorato ~ Doctoral School
WHAT YOU ARE, TAKES YOU FAR

Doctoral Dissertation
Doctoral Program in Electrical, Electronics, and Communications Engineering
(34^{th}cycle)

UAV-based Far-Field and Near-Field Antenna Measurements

By

Lorenzo Ciorba

******

Supervisor(s):
Prof. G. Vecchi, Supervisor
Dr. G. Virone, Co-Supervisor
Dr. M. Righero, Co-Supervisor

Doctoral Examination Committee:
Prof. Manuel Sierra Castañer, Referee, Universidad Politécnica de Madrid
Prof. Paolo Rocca, Referee, Università di Trento

Politecnico di Torino
2022

Declaration

I hereby declare that, the contents and organization of this dissertation constitute my own original work and does not compromise in any way the rights of third parties, including those relating to the security of personal data.

Lorenzo Ciorba
2022

* This dissertation is presented in partial fulfillment of the requirements for **Ph.D. degree** in the Graduate School of Politecnico di Torino (ScuDo).

A mamma, papà e Matteo.

Acknowledgements

Acknowledgements are written in Italian.
Ringrazio il relatore di questa tesi Giuseppe Vecchi e i co-relatori Giuseppe Virone e Marco Righero per il loro contributo fondamentale.
Un grande grazie ai prof. Renato Orta e Paolo Tilli per aver condiviso con me la loro professionalità e passione per il loro lavoro.
Ringrazio i miei colleghi Giuseppe Addamo, Fabio Paonessa, Oscar Peverini, Mauro Lumia, Azeddine Atrass, Giorgio Giordanengo, Pietro Bolli.
Ringrazio infine i miei compagni di viaggio Marcello Zucchi, Barbara Cappello, David Rodriguez, Jorge Alberto Tobon Vasquez, Antonio Mastropietro.

Abstract

In recent years, Unmanned Aerial Vehicle technology has been experimented as antenna measurement solution for very large antennas that cannot be placed in an anechoic chamber or have to be characterized in-situ. The UAV already proved to be a powerful tool for Far-Field (FF) measurements, thanks to its portability, low cost, and ability to perform arbitrary paths. In the first part of this thesis, UAV-based FF measurements of a Square Kilometre Array prototype station in VHF band are presented. One full SKA-Low station consists of 256 digital-beam-formed dual-polarized elements randomly distributed on a 40-m size area. This activity demonstrated the usage of the UAV to verify the large electromagnetic models of the SKA in harsh environments such as the Australian desert.
However, Near-Field (NF) strategies become necessary when the Antenna Under Test (AUT) is so large that the Fraunhofer distance is no longer compliant with flight altitude regulations (hundreds of meters). In these cases, a Near Field to Far Field (NF-FF) transformation must be used to determine the FF quantities of interest from NF data. Such technique generally requires the knowledge of both magnitude and phase of the sampled NF signal. However, in the UAV-based measurement setup, where source and receiver are generally not connected, the measured phase is continuously drifting during the flight. In current literature, different solutions have been exploited in order to retrieve the correct phase information, e.g., a fiber optic link connecting the UAV to the ground or phaseless techniques. In the second part of this thesis, a known antenna (called reference antenna) placed in the proximity of the AUT is instead used to reconstruct the phase of the measured NF signal. UAV-based NF measurements on a SKA-Low prototype at 175 MHz are presented to demonstrate the feasibility of the approach. The UAV equipped with a RF source is exploited as a large (40 m x 40 m) horizontal planar NF scanner. An inverse source NF-FF transformation is applied to such NF acquisitions. In this way, FF Embedded Element Patterns, array calibration coefficients and pattern are obtained. NF-FF

transformed results are validated with simulations and FF measurements.
The promising results suggest the usage of the presented technique in other applications such as radars, base stations and satellite antenna measurements.

Contents

List of Figures

List of Tables

Chapter 1

Introduction

In recent years, the Unmanned Aerial Vehicle (UAV) technology has become relevant in a variety of electromagnetic topics and applications such as multispectral imaging, electromagnetic field measurements and communications. For example, high-resolution images have been acquired using a Synthetic Aperture Radar (SAR) on a UAV [2]. Furthermore, a UAV-based measurement system has been developed for Radio Frequency (RF) exposure assessment [3]. As far as remote sensing is concerned, a thermal imager mounted on a UAV has been exploited in order to obtain land surface temperature [4]. Moreover, UAV-mounted base stations have been proposed to improve network performances during some occasional especially crowded events [5]. A UAV equipped with a camera has been also used in antenna diagnostics to acquire images of base-station antennas in order to spot possible defects [6].

The UAV has proved to be a powerful tool also for the antenna measurement community [7]. In particular, a UAV-based procedure has been recently added to the IEEE Recommended Practice for Antenna Measurements [8] to characterize an Antenna Under Test (AUT) in terms of its radiation pattern. For example, a UAV equipped with a power sensor can be used to acquire the radiation patten of a transmitting AUT. Alternatively, the UAV can mount a transmitter if the AUT operates in receiving mode. In both cases, the UAV allows to easily reach the Far-Field (FF) distance of the AUT with virtually no need of infrastructures. However, when the AUT is very large, the FF distance (greater than hundreds of meters) is no longer compliant with flight altitude regulations. In this case, Near-Field (NF) approaches become necessary and a Near Field to Far Field (NF-FF) transformation can be used to determine the FF

quantities of interest from NF data.
The following Section summarizes the state of the art for UAV-based antenna measurements. Finally, aim and problems addressed in this thesis are described in Section 1.2.

1.1 UAV-based Antenna Measurements: state of the art

UAV-based FF measurements have been extensively addressed in recent literature. For example, radiation patterns of log-periodic antennas have been measured through a flying multicopter at 408 MHz [9], 433 MHz [10] and 750 MHz [11]. Furthermore, a biconical antenna have been characterized in its principal planes through a flying hexacopter at 150 MHz [9].
Radio telescopes represent an ideal application of UAVs, as they are usually placed in open areas and can be characterized with simple flights with few safety-related issues. This is particularly true for low-frequency radio telescopes based on phased-array scheme, where UAVs have been employed also for the array calibration. For example, experimental tests of the Low-Band Antennas (LBA) of the LOw Frequency ARray (LOFAR) have been performed exploiting astronomical calibration sources and RF sources mounted on cranes [12] or drones [13]. In-situ measurements of radio telescope prototypes have also been performed in the 50 - 450 MHz frequency band [14][1], [15], [16], [17]. Furthermore, dual-polarized dipoles of an hydrogen observatory instrument have been calibrated at 137 MHz using a multi-rotor UAV [18]. A 6-m dish antenna radio telescope for solar spectrography have been also characterized at 328 MHz using an octocopter [19]. Moreover, an antenna array prototype (6 m x 6 m) made of printed dipoles for mid-frequency radio astronomy has been characterized at 350 MHz [20]. A UAV-mounted test source has been also developed for a Q-band polarimeter, i.e., the Large-Scale Polarization Explorer (LSPE) [21].
As far as radar antennas are concerned, radiation pattern of an HF oceanographic radar has been measured through a quad-rotor UAV [22]. Measurements at HF and X band have been also performed [23], [24]. Furthermore, a radar prototype for the analysis of the icy crust of Jupiter's moon Europa has been characterized at 60 MHz

[1] Chapter 3 of this thesis contains part of the work published in [14].

[25].
As far as mobile networks and broadcast systems are concerned, radiation patterns of base station antennas have been validated through an antenna (e.g., biconical or commercial mobile phone antenna) and a portable receiver mounted on a UAV [26], [27], [28].
For the sake of readability, Table 1.1 (first part) summarizes the previously cited works on UAV-based FF measurements. These references are arranged in chronological order. The year of publication, the working frequency, if the UAV-mounted antenna operates in transmitting (TX) or receiving (RX) mode, the UAV-mounted antenna and the AUT are reported on columns. It can be seen from Table 1.1 that in VHF and UHF bands the UAV-mounted antenna is usually a low-directive element such as a monopole, biconical or dipole antenna. This choice of such low-directive probes is usually made to reduce possible errors from wrong sampling of the UAV position and orientation, e.g., due to abrupt movements of the UAV flying in adverse wind conditions. In addition to Table 1.1, in other works in literature [35], [36] the UAV does not rigorously satisfy the FF conditions but flies close to the FF region of the AUT, obtaining good results.
NF strategies [31], [33] become necessary when the AUT is so large that the Fraunhofer distance $2D^2/\lambda$ (greater than hundreds of meters; where D is the AUT size and λ is the wavelength) is no longer compliant with flight altitude regulations. In these cases, a NF-FF transformation can be used to determine the FF quantities of interest from NF data. Such technique generally requires the knowledge of both magnitude and phase of the sampled NF signal. However, in a UAV-based measurement setup, where source and receiver are generally not connected, the measured phase is continuously drifting during the flight. One solution to overcome this problem is to use an additional (known) antenna placed in the proximity of the AUT [34][2].
Another solution is to connect (tether) the UAV to the ground equipment with a RF-over-fiber link [32], [37] to provide a valid phase reference. This is a reliable method, suitable with certain flight strategies. However, the UAV flight is constrained by the presence of the cable that makes the flight more difficult to perform and to setup. This is especially cumbersome for horizontal scans where the UAV flies above the AUT.
Phaseless techniques have also been applied to UAV-based measurements [29], [30].

[2]The author of this thesis is the first author of [34]. Chapter 4 of this thesis contains part of the work published in [34].

Table 1.1 Summary of UAV-based antenna measurements. FF (first part) and NF (second part) measurements are separated by the horizontal line. On columns: year of publication, the working frequency, if the UAV-mounted antenna operates in transmitting (TX) or receiving (RX) mode, the UAV-mounted antenna and the AUT. A label "ND" is reported when information is not available.

Year	**Freq.**	**TX-RX**	**UAV-antenna**	**AUT**	**Ref.**
2014	150-408MHz	TX	dipole	wire antennas	[9]
2014	433MHz	TX	monopole	log-periodic	[10]
2015	30-80MHz	TX	biconical	LBA-LOFAR	[12]
2015	328MHz	TX	monopole	dish	[19]
2015	408MHz	TX	dipole	MAD	[16]
2016	250-450MHz	TX	dipole	MAD-SAD	[17]
2016	598MHz	RX	ND	ND	[26]
2016	3-50MHz	TX	dipole	ND	[22]
2017	9GHz	TX	monopole	surface-wave-ant.	[24]
2017	137MHz	TX	biconical	dipole	[18]
2018	750MHz	TX	dipole	log-periodic	[11]
2018	57MHz	TX	dipole	LBA-LOFAR	[13]
2018	350MHz	TX	dipole	array	[20]
2018	2GHz	RX	phone	ND	[27]
2018	473MHz	RX	directional	tower	[28]
2018	60MHz	RX	biconical	dipole	[25]
2019	13MHz	TX	monopole	ND	[23]
2020	44GHz	TX	horn	horn	[21]
2020	50-320MHz	TX	dipole	AAVS1.5-EDA2	[14]-[15]
2017-9	4.65GHz	RX	monopole	horn array	[29]- [30]
2018	70MHz	TX	dipole	LBA-LOFAR	[31]
2019	2.7GHz	RX	patch	horn	[32]
2022	120-180MHz	TX	dipole	HBA-LOFAR	[33]
2022	175MHz	TX	dipole	pre-AAVS1	[34]

In this case, phase information is not acquired (i.e., magnitude-only measurements are performed) and the measurement setup is highly simplified. However, these methods minimize a non linear and non convex cost functional. For this reason, these techniques could lead to an ill-posed problem that suffers of local minima.
As far as UAV-based NF measurements are concerned, NF measurements have been compared with NF simulations [31] (without the application of a NF-FF transformation). Furthermore, the NF focusing method has been used to validate the radiation pattern of the High-Band Antennas of LOFAR within a limited angular range around the beam axis [33]. On the contrary, in [29], [30], [32], [34][3] a NF-FF transformation has been applied to the measured NF data.
UAV-based NF measurements are reported in the second part of Table 1.1 (after the horizontal black line). It is evident that so far NF strategies have not been exploited as much as the FF ones.
To summarize, UAV-based antenna measurements are particularly convenient when an in-situ validation of the AUT is required, i.e., the AUT must be characterized in its operating environment, considering all possible reflections of the ground or near scatterers. Moreover, the UAV measurement procedure is advantageous when it is not convenient to mount the AUT inside an anechoic chamber either due to its excessive dimension (e.g., the case of an antenna array in VHF band) or the low operating frequency (at which the wall absorbers exhibit poor performance). As a last remark, the UAV measurement setup is usually cheaper with respect to the one found in anechoic chambers.
However, the UAV procedure introduces new challenges and difficulties to overcome. For example, rigorously speaking, the UAV structure is not of the time-harmonic type. This is because the UAV rotor blades are always rotating, i.e., the source geometry is continuously changing during the flight. The impact of UAV rotor blades and propellers on electromagnetic measurements has been recently studied [38], [39], [40]. Furthermore, the non-regularity of the UAV path and orientation makes the post-processing of measurements (e.g., AUT gain computation, NF-FF transformation) more complex.
In conclusion, UAV-based FF measurements have been extensively studied in recent years. On the other hand, UAV-based NF measurements are gaining a lot of attention thanks to their practicability (a flight at small distance from the AUT can be

[3]Chapter 4 of this thesis contains part of the work published in [34].

performed). However, this measurement setup is more challenging and still presents open problems.

1.2 Doctoral Research Activity

This thesis represents the natural evolution of [41], [9], [14], [13], [16], [17], [31] and is focused on the characterization of antennas in terms of their radiation pattern from FF or NF measurements performed using a UAV. In the previous works, UAV-based measurements on reference antennas, small array demonstrators, and partially deployed stations have been mostly presented. The FF distance was therefore satisfied. NF measurements have also been performed [31] and compared with NF simulations (without the application of a NF-FF transformation).
In this thesis, array of active antennas in VHF band with digital beamforming are considered as AUT. More precisely, the AUT is represented either by an array element (embedded element) or a subset of antennas (cluster) or a full station of the Square Kilometre Array (SKA). The SKA is a radio-telescope under construction in Australia and South Africa and it will be the biggest radio-telescope in the world. SKA-low covers the low frequency part of the SKA, i.e., from 50 to 350 MHz. One full SKA-low station consists of 256 digital-beamformed dual-polarized elements pseudo-randomly distributed on a 40-m size area. Each element is equipped with a Low Noise Amplifier (LNA) on top. Moreover, the two polarizations of each element are connected to the analog inputs of a Tile Processing Module (TPM) [42] which samples and digitizes the received signals in magnitude and phase (e.g., complex voltages). Due to the presence of such acquisition system, the UAV is therefore equipped with a continuous-wave synthesizer and a dipole antenna. While the UAV flies over the array according to a pre-defined path, the signal received at each array element is acquired through the TPM. During the UAV flight, the position of the UAV is usually recorded by the drone through a differential Global Navigation Satellite System (GNSS) which guarantees a few centimetres of accuracy (such position accuracy can be considered acceptable at the considered VHF band). Furthermore, the UAV orientation is also acquired during the flight in order to reach the required measurement accuracy.
Because of the huge size of the considered AUT, the Fraunhofer distance can be greater than hundreds of meters. This is not compliant with flight altitude regulations,

i.e., the FF region is not accessible using a UAV. For this reason, NF strategies are much more convenient. As a drawback, a NF-FF transformation must be applied to the measured NF data.
In this thesis, FF and NF measurements of SKA prototypes using a UAV are presented and analyzed. In particular, a NF-FF transformation is applied to UAV-based NF measurements. In this way, Embedded Element Patterns (EEPs)[4] and array pattern of the AUT are computed.
The measurement setup considered in this thesis should be distinguished from the Over-The-Air (OTA) testing [43] of an antenna. In OTA testing, the AUT port is usually not accessible and cannot be physically connected to the test equipment. Furthermore, the considered signals are usually not time-harmonic (i.e., not sinusoidal). In the UAV-based measurement setup considered in this thesis, source and receiver are not connected, e.g., the UAV is not tethered to the ground through cables. Hence, the measured phase is continuously drifting during the flight. In this thesis, the correct phase information is retrieved through a known antenna (herein after referred to as the reference antenna) that is placed in the proximity of the AUT. Signals from both the AUT and reference antenna are sampled (magnitude and phase) by a common receiver that is not phase-locked to the continuous-wave source placed on-board the UAV. A phase reconstruction method is hence proposed. It uses the measured phase difference between AUT and the reference antenna signals. This method can be seen as a generalization of the standard procedure [44] found in FF test ranges which uses a reference antenna to retrieve the phase information. However, in the standard procedure, source and reference antenna are fixed while the AUT rotates. In the present UAV-based measurement setup, the source is instead moving with respect to both the AUT and the reference antenna. The proposed technique allows to maintain the advantages of a non-tethered flight. Furthermore, the NF-FF transformation problem remains linear through the availability of the reconstructed phase information.
This thesis is organized as follows.
In Chapter 2, the phase retrieval method using the reference antenna is presented.
In Chapter 3, UAV-based FF measurements of SKA prototypes located in Australia are considered. An element of the array under test (whose FF pattern is known from simulations) is chosen as reference antenna for the phase retrieval method (described

[4]The EEP of an array element is the radiation pattern of an array with one element excited and all the others terminated on a specified load.

in Chapter 2). EEPs (magnitude and phase) are extracted and shown. Moreover, a synoptic visualization of the agreement between measurements and simulations is reported. Active element gain measurements and a position error estimation method of array clusters are shown and discussed.
In Chapter 4, UAV-based FF and NF measurements of an SKA prototype located in the United Kingdom are considered. The phase retrieval method through the reference antenna proposed in Chapter 2 is applied to FF and NF measurements. The considered reference antenna is a known external antenna which is placed approximately 15 m away from the array under test. Using the phase information retrieved through the reference antenna, an inverse source NF-FF transformation is applied to measured data. NF-FF transformed results are validated with measurements and simulations.
In Chapter 5, some conclusions are drawn.
In Appendix A, a proof of the uniqueness of the inverse source problem is reported[5].
In Appendix B, theoretical remarks on the inverse source NF-FF transformation and reciprocity [6] are drawn.

[5]Understand the well-posedness of such problem is fundamental for the correct application of the inverse source NF-FF transformation in Chapter 4

[6]It should be recalled that in the considered measurement setup the UAV-mounted antenna operates in transmitting mode and the AUT in receving mode.

Chapter 2

Phase Reconstruction using a Reference Antenna

In the simplest types of UAV-based measurement setups, where source and receiver are not connected, the measured phase is continuously drifting during the flight. Several phase retrieval algorithms [45], [46] (e.g., alternating minimization methods, least squares formulations and lifting methods) have been proposed in literature. These methods rely on magnitude-only measurements and minimize a non linear and non convex cost functional. For this reason, these techniques could lead to an ill-posed problem that suffers of local minima. A linear reconstruction method based on multi-probe measurements to mitigate all these issues has been also recently proposed [47]. Another possible solution to avoid phase measurements is the usage of auxiliary hardware, e.g., other antennas, cables, and RF components. For this purpose, an additional antenna and the cross-correlation between its signal and the AUT signal can be exploited [48]. Other solutions rely on interferometric or holographic techniques. In interferometric techniques [49], [50] magnitude-only measurements of combinations of signals coming from two probes are exploited in order to compute the required phase difference between signals. In holographic techniques [51], [52], the signal under test is superimposed with the source signal, forming the hologram. The signal under test is then reconstructed through magnitude-only measurements of the summed signal.

In this thesis, the correct phase information is retrieved through a known antenna (herein after referred to as the reference antenna) that is placed in the proximity of the AUT. The distance between the reference antenna and the AUT must be sufficiently

large in order not to perturb their field distribution. Signals from both the AUT and reference antenna are sampled (magnitude and phase) by a common receiver that is not phase-locked to the continuous-wave source placed on-board the UAV.
In the next part, an introductory analysis on AUT and reference antenna signals and their phase difference is considered. The center frequency of the receiver is denoted with f_0 whereas the frequency of the continuous-wave transmitter on the UAV is denoted by $f_0 + \Delta f$, where Δf represents the frequency offset between transmitter and receiver. If the UAV has a stationary position (i.e., its position is fixed), voltages v_{RX} and v_{ref} received at the AUT and reference antenna in time-domain are of time-harmonic type, i.e.,

$$\begin{cases} v_{RX}(t) = A_{RX}\cos(\omega_0 t + \Delta\omega t + \phi_{RX}) \\ v_{ref}(t) = A_{ref}\cos(\omega_0 t + \Delta\omega t + \phi_{ref}) \end{cases} \tag{2.1}$$

where $w_0 = 2\pi f_0$ and $\Delta\omega = 2\pi\Delta f$ represent the angular frequencies whereas A_{RX}, A_{ref} and ϕ_{RX}, ϕ_{ref} represent the magnitudes and phases of the AUT and reference antenna signals. The receiver output usually consists of magnitude and phase of each signal, i.e., A_{RX} and $\Delta\omega t + \phi_{RX}$ for the AUT and A_{ref} and $\Delta\omega t + \phi_{ref}$ for the reference antenna. Of course, such quantities are sampled on a set of discrete and finite time instants; here, a continuous time index t is instead considered for simplicity. It should be noted that the measured phase continuously drifts in time due to the presence of the term $\Delta\omega t$. Considering the difference between the AUT and reference antenna measured phases, one obtains the actual phase difference of the signals, i.e.,

$$\Delta\omega t + \phi_{RX} - (\Delta\omega t + \phi_{ref}) = \phi_{RX} - \phi_{ref} \tag{2.2}$$

In this way, the phase drifting term $\Delta\omega t$ is cancelled.
During the flight, i.e., with the UAV which is moving in space, the received signals in (2.1) become amplitude and frequency modulated, i.e.,

$$\begin{cases} v_{RX}(t) = A_{RX}(t)\cos(\omega_0 t + \Delta\omega(t)t + \phi_{RX}(t)) \\ v_{ref}(t) = A_{ref}(t)\cos(\omega_0 t + \Delta\omega(t)t + \phi_{ref}(t)) \end{cases} \tag{2.3}$$

Nevertheless, the measured phase difference in (2.2) is still independent on the frequency shift $\Delta\omega$. Such frequency shift $\Delta\omega$ generally depends on the time, i.e., $\Delta\omega = \Delta\omega(t)$, because of possible instabilities at the transmitter (e.g., due to vibra-

tions or temperature variations). However, if the transmitter is sufficiently stable, the term $\Delta\omega$ can be assumed to be almost constant during the flight.
In the following Section, a phase reconstruction method that uses the measured phase difference between AUT and the reference antenna signals is proposed. In Section 2.1, the UAV and AUT are assumed to be in FF each other whereas in Section 2.2 the NF case (i.e., the UAV can fly in the NF of the AUT) is analyzed.

2.1 Phase Reconstruction for Far-Field Measurements

Part of the theory presented in this Section has been already published in [33].
UAV-based FF measurements have been extensively studied in recent years (see Chapter 1). In particular, a lot of attention has been devoted to gain measurements. In the latter configuration, magnitude-only measurements are usually sufficient (the phase of the signal is usually not sampled). However, as far as phased arrays are concerned, the array pattern is computed by summation of the EEPs of all the array elements. It is therefore necessary to acquire the complex signals from each embedded element in order to correctly compute all the EEPs in their magnitude and phase. In this Section, the phase retrieval method based on the phase difference between AUT and reference antenna signals is considered. First, the single antenna case is analyzed (see Section 2.1.1). Then, the general case of an antenna array is considered (see Section 2.1.2). Equations for the computation of the phases of the EEPs are shown and analyzed.
In this Section, the AUT and the UAV are assumed to be in FF each other. The same condition is assumed between UAV and reference antenna. Furthermore, a free-space approximation is made (reflections of the ground are not considered).

2.1.1 Single Element

In this Section, the case of a single element (not an array of elements) is analyzed. A schematic of the measurement setup is shown in Fig. 2.1. The received open-circuit voltage V_{RX}^{oc} at the AUT is given by

$$V_{RX}^{oc}(\mathbf{r}) = \mathbf{h}_{AUT}(\hat{\mathbf{r}}) \cdot \mathbf{E}_s(\mathbf{r}) \tag{2.4}$$

where $\mathbf{h}_{AUT}$ is the effective height of the AUT and $\mathbf{E}_s$ is the incident field to the AUT from the UAV source, with position $\mathbf{r} = r\hat{\mathbf{r}}$. The dependency of $\mathbf{E}_s$ on the UAV orientation is understood and suppressed. Because of the FF assumption, $\mathbf{E}_s$ can be represented as

$$\mathbf{E}_s(\mathbf{r}) = \frac{e^{-jkr}}{4\pi r}\mathbf{e}_s(\hat{\mathbf{r}}) \tag{2.5}$$

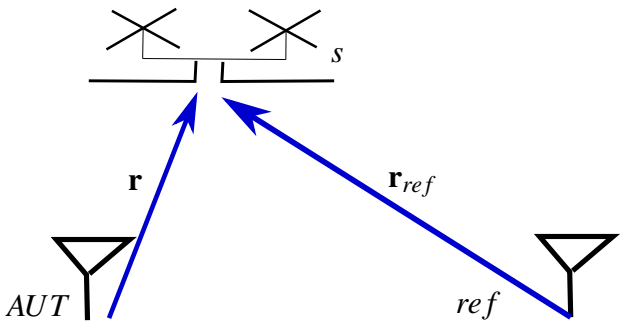

Fig. 2.1 Measurement schematics: the UAV (s), AUT and reference antenna. Position vectors $\mathbf{r}$ and $\mathbf{r}_{ref}$ are considered with respect to a reference system centered in the AUT and reference antenna, respectively. Picture from [1].

where $\mathbf{e}_s$ is the FF pattern of the UAV-mounted source and k is the free-space wavenumber. For reciprocity, the effective height $\mathbf{h}_s$ of the source and its FF pattern $\mathbf{e}_s$ are related by

$$\mathbf{e}_s = -j\frac{Z_0}{2\lambda}4\pi I_s \mathbf{h}_s \tag{2.6}$$

where $Z_0 \simeq 377\Omega$ is the free-space impedance and I_s is the current source on the UAV. Voltage V_s and current I_s of the UAV-mounted source are related through the impedance Z_s by $V_s = Z_s I_s$ (or equivalently through the admittance $Y_s = 1/Z_s$, i.e., $I_s = Y_s V_s$). Substituting (2.5) and (2.6) in (2.4), it can be proved that

$$V_{RX}^{oc}(\mathbf{r}) = -j\frac{Z_0}{2\lambda}4\pi Y_s V_s |\mathbf{h}_{AUT}(\hat{\mathbf{r}})||\mathbf{h}_s(-\hat{\mathbf{r}})|\frac{e^{-jkr}}{4\pi r}\hat{\mathbf{p}}_{AUT}(\hat{\mathbf{r}})\cdot\hat{\mathbf{p}}_s(-\hat{\mathbf{r}}) \tag{2.7}$$

where the polarization unit vectors are defined by $\hat{\mathbf{p}}_{AUT} = \mathbf{h}_{AUT}/|\mathbf{h}_{AUT}|$ and $\hat{\mathbf{p}}_s = \mathbf{h}_s/|\mathbf{h}_s|$. A similar equation can be written for the received open-circuit voltage V_{ref}^{oc} at the reference antenna

$$V_{ref}^{oc}(\mathbf{r}) = -j\frac{Z_0}{2\lambda}4\pi Y_s V_s |\mathbf{h}_{ref}(\hat{\mathbf{r}}_{ref})||\mathbf{h}_s(-\hat{\mathbf{r}}_{ref})|\frac{e^{-jkr_{ref}}}{4\pi r_{ref}}\hat{\mathbf{p}}_{ref}(\hat{\mathbf{r}}_{ref})\cdot\hat{\mathbf{p}}_s(-\hat{\mathbf{r}}_{ref}) \tag{2.8}$$

where $\mathbf{h}_{ref}$ is the effective height of the reference antenna, the polarization unit vector is $\hat{\mathbf{p}}_{ref} = \mathbf{h}_{ref}/|\mathbf{h}_{ref}|$ and $\mathbf{r}_{ref} = r_{ref}\hat{\mathbf{r}}_{ref}$ is the position of the UAV with respect to the reference antenna (see Fig. 2.1).
Dividing (2.7) by (2.8), once obtains

$$\frac{V_{RX}^{oc}(\mathbf{r})}{V_{ref}^{oc}(\mathbf{r}_{ref})} = e^{-jk(r-r_{ref})}\frac{r_{ref}}{r}\frac{|\mathbf{h}_{AUT}(\hat{\mathbf{r}})||\mathbf{h}_s(-\hat{\mathbf{r}})|}{|\mathbf{h}_{ref}(\hat{\mathbf{r}}_{ref})||\mathbf{h}_s(\hat{\mathbf{r}}_{ref})|}\frac{\hat{\mathbf{p}}_{AUT}(\hat{\mathbf{r}})\cdot\hat{\mathbf{p}}_s(-\hat{\mathbf{r}})}{\hat{\mathbf{p}}_{ref}(\hat{\mathbf{r}}_{ref})\cdot\hat{\mathbf{p}}_s(-\hat{\mathbf{r}}_{ref})} \tag{2.9}$$

Considering the phase of (2.9), one finally obtains the phase difference

$$\angle V_{RX}^{oc} - \angle V_{ref}^{oc} = \angle(\hat{\mathbf{p}}_{AUT} \cdot \hat{\mathbf{p}}_s) - \angle(\hat{\mathbf{p}}_{ref} \cdot \hat{\mathbf{p}}_s) - k(r - r_{ref}) \tag{2.10}$$

where $\angle$ returns the phase of a complex number and the $\mathbf{r}$ dependence is understood. Of course, all these phase equalities are valid up to addition of a multiple integer of 2π.

Let's consider unit vectors $\hat{\mathbf{u}}, \hat{\mathbf{v}} : S^2 \longrightarrow \mathbb{R}^3$ such that $\{\hat{\mathbf{u}}(\hat{\mathbf{r}}), \hat{\mathbf{v}}(\hat{\mathbf{r}})\}$ forms a basis of the plane (passing through the origin) with unit normal vector $\hat{\mathbf{r}}$, where S^2 is the sphere of unit radius in $\mathbb{R}^3$ (e.g., $\hat{\mathbf{u}} = \hat{\theta}$, $\hat{\mathbf{v}} = \hat{\phi}$ can be the unit vectors of spherical coordinates). Hence, polarization unit vectors can be written as $\hat{\mathbf{p}}_s = \hat{p}_{s,v}\hat{\mathbf{v}} + \hat{p}_{s,u}\hat{\mathbf{u}}$ and $\hat{\mathbf{p}}_{AUT} = \hat{p}_{AUT,v}\hat{\mathbf{v}} + \hat{p}_{AUT,u}\hat{\mathbf{u}}$.

Phase of AUT pattern. Case: linearly polarized source, i.e., $\hat{\mathbf{p}}_s = p_{s,v}\hat{\mathbf{v}}$

If the source is linearly polarized along $\hat{\mathbf{v}}$, i.e., $\hat{\mathbf{p}}_s = p_{s,v}\hat{\mathbf{v}}$ then the phase of the FF pattern of the AUT can be extracted from (2.10) by

$$\angle \hat{p}_{AUT,v} = \angle V_{RX}^{oc} - \angle V_{ref}^{oc} + \angle(\hat{\mathbf{p}}_{ref} \cdot \hat{\mathbf{p}}_s) - \angle \hat{p}_{s,\theta} + k(r - r_{ref}) \tag{2.11}$$

where the $\mathbf{r}$ and $\mathbf{r}_{ref}$ dependence is understood. Because the right hand side of (2.11) is fully known, the phase of the FF pattern ($v-$component) can be computed.

Phase of AUT pattern. General case: $\hat{\mathbf{p}}_s = \hat{p}_{s,v}\hat{\mathbf{v}} + \hat{p}_{s,u}\hat{\mathbf{u}}$

The AUT pattern can be in principle be computed also when the source is not linearly polarized (not yet applied to experimental data). However, two measurements must be performed (ideally, the second with the probe 90° rotated with respect to the first measurement).

When the source is not linearly polarized, both components of $\hat{\mathbf{p}}_s$ must be taken into account $\hat{\mathbf{p}}_s = \hat{p}_{s,v}\hat{\mathbf{v}} + \hat{p}_{s,u}\hat{\mathbf{u}}$. From (2.9), it can be easily shown that

$$\mathbf{h}_s(-\hat{\mathbf{r}}) \cdot \mathbf{h}_{AUT}(\hat{\mathbf{r}}) = \frac{r}{r_{ref}} e^{jk(r-r_{ref})} \frac{V_{RX}^{oc}}{V_{ref}^{oc}} \mathbf{h}_{ref}(\hat{\mathbf{r}}_{ref}) \cdot \mathbf{h}_s(-\hat{\mathbf{r}}_{ref}) \tag{2.12}$$

In this case, for each direction $\hat{\mathbf{r}}$ two different UAV measurements (labeled by $n = 1$ and $n = 2$) are required, e.g., in the second measurement the UAV dipole direction is orthogonal to the one of the first measurement. For each acquired direction $\hat{\mathbf{r}}$, a linear system can be written

$$\begin{bmatrix} h_{s,1,v} & h_{s,1,u} \\ h_{s,2,v} & h_{s,2,u} \end{bmatrix} \begin{bmatrix} h_{AUT,v} \\ h_{AUT,u} \end{bmatrix} = \begin{bmatrix} b_1 \\ b_2 \end{bmatrix} \tag{2.13}$$

where b_n is a known term that comes from the right-hand-side of (2.12) and $\mathbf{h}_{s,n}$ is the effective height of the source for n-th measurement, for $n = 1, 2$. The matrix on the left-hand-side of (2.13) is sometimes called Jones matrix [53] and its condition number is linked to the intrinsic cross-polarization ratio (IXR) of the UAV-mounted source.

2.1.2 Array

In this Section, the phase retrieval method is presented for an antenna array. In this Section, FF interaction between the array and the UAV is assumed. Similarly to the single element case (see (2.9)) the ratio between the received open-circuit voltage V_{RX}^{oc} at the $n-$th array element and the received open-circuit voltage V_{ref}^{oc} at the reference antenna is

$$\frac{V_{RX}^{oc,n}(\mathbf{r})}{V_{ref}^{oc}(\mathbf{r}_{ref})} = e^{-jk(r-r_{ref})}\frac{r_{ref}}{r}\frac{|\mathbf{h}^n(\hat{\mathbf{r}})||\mathbf{h}_s(-\hat{\mathbf{r}})|}{|\mathbf{h}_{ref}(\hat{\mathbf{r}}_{ref})||\mathbf{h}_s(\hat{\mathbf{r}}_{ref})|}\frac{\hat{\mathbf{p}}^n(\hat{\mathbf{r}})\cdot\hat{\mathbf{p}}_s(-\hat{\mathbf{r}})}{\hat{\mathbf{p}}_{ref}(\hat{\mathbf{r}}_{ref})\cdot\hat{\mathbf{p}}_s(-\hat{\mathbf{r}}_{ref})} \tag{2.14}$$

where $\mathbf{h}^n$ is the effective height of the $n-$th element (considered as embedded element, $\mathbf{h}^n$ takes into account mutual-coupling phenomena) and r is the distance between the array center and the UAV. Briefly, omitting the $\mathbf{r}$ dependence, (2.14) becomes:

$$\frac{V_{RX}^{oc,n}}{V_{ref}^{oc}} = e^{-jk(r-r_{ref})}\frac{r_{ref}}{r}\left(\frac{1}{|\mathbf{h}_{ref}||\mathbf{h}_s|}\frac{1}{\hat{\mathbf{p}}_{ref}\cdot\hat{\mathbf{p}}_s}\right)|\mathbf{h}^n||\mathbf{h}_s|\hat{\mathbf{p}}^n\cdot\hat{\mathbf{p}}_s \tag{2.15}$$

Similarly to the single element case (see (2.11)), if the source is linearly polarized, i.e., $\hat{\mathbf{p}}_s = p_{s,v}\hat{\mathbf{v}}$ then the phase of the FF pattern of the $n-$th array element can be extracted from (2.15) by

$$\angle\hat{p}_v^n = \angle V_{RX}^{oc,n} - \angle V_{ref}^{oc} + \angle(\hat{\mathbf{p}}_{ref}\cdot\hat{\mathbf{p}}_s) - \angle\hat{p}_{s,v} + k(r-r_{ref}) \tag{2.16}$$

2.2 Phase Reconstruction for Near-Field Measurements

Part of the work presented in this Section has been previously published in [1], [34]. In this Section, the phase retrieval method based on the phase difference between AUT and reference antenna signals is considered for NF measurements, i.e., the UAV can fly in the NF of the AUT. FF approximation between UAV and reference antenna is assumed. Furthermore, a free-space approximation is made (reflections of the ground are not considered[1]).
The phase difference needed to apply the NF-FF transformation to the n-th array element can be expressed as $\angle V_{RX}^{n} - \angle V_s$. From the transmission equation between reference antenna and UAV-mounted source, see (2.8), once obtains

$$\angle V_{ref}^{oc} = \angle V_s - kr_{ref} + \angle(\hat{\mathbf{p}}_{ref}(\hat{\mathbf{r}}_{ref}) \cdot \hat{\mathbf{p}}_s(-\hat{\mathbf{r}}_{ref})) \tag{2.17}$$

It should be noted that V_{ref}^{oc} does not generally coincide with the measured voltage V_{ref} (see Section 2.1). The two voltages are related by $V_{ref} = C_{ref} V_{ref}^{oc}$, where $C_{ref} = Z_{RX,ref}/(Z_{RX,ref} + Z_{A,ref})$ is an adimensional constant and $Z_{A,ref}$ and $Z_{RX,ref}$ are the reference antenna and receiver impedances. More precisely, $Z_{RX,ref}$ takes into account all RF components from the reference antenna toward the digitizer i.e., cables, LNA and the receiver. It should be noted that if such RF components are known and characterized then C_{ref} is known. However, in this thesis, the constant C_{ref} was not known. It should be noted that the constant C_{ref} depends on the chosen reference antenna polarization but is independent on the UAV position (it can depend on instabilities due to temperature variations). In Section 2.2.1, a procedure to compensate the phase shift between signals coming from the two reference antenna polarizations is presented.
From (2.17), the received phase at the reference antenna is hence related to the transmitter phase through

$$\angle V_{ref} = \angle V_{ref}^{oc} + \angle C_{ref} = \angle V_s - kr_{ref} + \angle(\hat{\mathbf{p}}_{ref}(\hat{\mathbf{r}}_{ref}) \cdot \hat{\mathbf{p}}_s(-\hat{\mathbf{r}}_{ref})) + \angle C_{ref} \tag{2.18}$$

[1] this approximation is verified because antennas considered in this thesis are placed over a ground plane. For a more accurate model, reflections of the UAV field from the ground and scattering from the AUT to the reference antenna (and viceversa) must be taken into account.

The desired phase difference $\angle V^n_{RX} - \angle V_s$ is hence obtained from 2.18 by

$$\angle V^n_{RX} - \angle V_s = \angle V^n_{RX} - \angle V_{ref} - kr_{ref} + \angle(\hat{\mathbf{p}}_{ref}(\hat{\mathbf{r}}_{ref}) \cdot \hat{\mathbf{p}}_s(-\hat{\mathbf{r}}_{ref})) + \angle C_{ref} \quad (2.19)$$

Equation (2.19) can be used when only one component of the electric field is measured (as in [1]), say the y-component. Then, NF-FF transformations exploiting only the y-component of the field are applicable. For this purpose, only one flight (e.g., a y-oriented raster, see Fig. 4.3) is needed and the constant phase shift $\angle C_{ref}$ does not affect the reconstruction and its presence in (2.19) can be neglected. However, as it will be shown in Chapter 4 (Fig. 4.20), the usage of only one NF component in the NF-FF transformation leads to inaccurate cross-polarization values in the computed FF pattern.

2.2.1 Phase Reconstruction using a Dual-Polarized Reference Antenna

The procedure presented in this Section will be applied to UAV-based antenna measurements in Chapter 4 where a dual-polarized reference antenna (with polarizations x and y) is available. When both components of the electric NF have to be considered (e.g., as input for a NF-FF transformation), samples along two orthogonal UAV flights must be acquired (e.g., in Chapter 4 an x-oriented and a y-oriented raster is performed, see Fig. 4.4). In this case, when the source polarization is orthogonal (or quasi-orthogonal) to the chosen reference antenna polarization, the signal received at the reference antenna may have a low signal-to-noise ratio. This degradation of the received signal may result in a poor phase reconstruction. For this reason, a dual-polarized reference antenna should be used, and the signal received through the polarization that matches the one of the source should be exploited. More precisely, for the data acquired along the x-oriented raster the x-polarized reference antenna must be used whereas for the data acquired along the y-oriented raster the y-polarized reference antenna must be exploited. In this way, polarization-matching between source and reference antenna is obtained and high signal-to-noise ratio for the measured receiving signal is ensured. For this purpose, the constants $C_{ref,x}$ and $C_{ref,y}$ such that $V_{ref,x} = C_{ref,x} V^{oc}_{ref,x}$ and $V_{ref,y} = C_{ref,y} V^{oc}_{ref,y}$ are considered, where $V_{ref,x}$, $V_{ref,y}$ and $V^{oc}_{ref,x}$, $V^{oc}_{ref,y}$ are the measured and open-circuit voltages at the x and y polarized reference antenna, respectively. The phase transmission equation for the

x and y reference antenna polarization (i.e., (2.18) with $C_{ref} = C_{ref,y}$ and (2.18) with $C_{ref} = C_{ref,x}$) would read

$$\angle V_{ref,x} = \angle V_s - kr_{ref} + \angle(\hat{\mathbf{p}}_{ref,x}(\hat{\mathbf{r}}_{ref}) \cdot \hat{\mathbf{p}}_s(-\hat{\mathbf{r}}_{ref})) + \angle C_{ref,x} \tag{2.20}$$

$$\angle V_{ref,y} = \angle V_s - kr_{ref} + \angle(\hat{\mathbf{p}}_{ref,y}(\hat{\mathbf{r}}_{ref}) \cdot \hat{\mathbf{p}}_s(-\hat{\mathbf{r}}_{ref})) + \angle C_{ref,y} \tag{2.21}$$

where $\hat{\mathbf{p}}_{ref,x}$ and $\hat{\mathbf{p}}_{ref,y}$ are the polarization unit vectors of the x and y polarized reference antenna, respectively. Since $C_{ref,y}$ is generally different from $C_{ref,x}$ (hence $\angle C_{ref,y} \neq \angle C_{ref,x}$) the phase reconstruction procedure leads to an unknown constant phase shift $\angle C_{ref,y} - \angle C_{ref,x}$ between the two phase reconstructions from the two orthogonal flights. Due to this phase shift, the whole phase reconstruction is not coherent and cannot be directly used as input for a NF-FF transformation. The unknown phase shift $\angle C_{ref,y} - \angle C_{ref,x}$ can be evaluated performing the difference between equations (2.21) and (2.20) i.e., eliminating the common term $\angle V_s$

$$\begin{aligned} \angle C_{ref,y} - \angle C_{ref,x} = \angle V_{ref,y} - \angle V_{ref,x} - \angle(\hat{\mathbf{p}}_{ref,y}(\hat{\mathbf{r}}_{ref}) \cdot \hat{\mathbf{p}}_s(-\hat{\mathbf{r}}_{ref})) + \\ + \angle(\hat{\mathbf{p}}_{ref,x}(\hat{\mathbf{r}}_{ref}) \cdot \hat{\mathbf{p}}_s(-\hat{\mathbf{r}}_{ref})) \end{aligned} \tag{2.22}$$

Applying (2.22), the phase reconstructions of the two orthogonal flights can be equalized through

$$\begin{aligned} \angle\left(\frac{V_{RX}^n}{V_s C_{ref,x}}\right) = \angle V_{RX}^n - \angle V_s - \angle C_{ref,x} = \\ = \angle V_{RX}^n - \angle V_{ref,x} - kr_{ref} + \angle(\hat{\mathbf{p}}_{ref,x}(\hat{\mathbf{r}}_{ref}) \cdot \hat{\mathbf{p}}_s(-\hat{\mathbf{r}}_{ref})) \end{aligned} \tag{2.23}$$

and

$$\begin{aligned} \angle\left(\frac{V_{RX}^n}{V_s C_{ref,x}}\right) = \angle V_{RX}^n - \angle V_s - \angle C_{ref,x} = \\ = \angle V_{RX}^n - \angle V_{ref,y} - kr_{ref} + \angle(\hat{\mathbf{p}}_{ref,y}(\hat{\mathbf{r}}_{ref}) \cdot \hat{\mathbf{p}}_s(-\hat{\mathbf{r}}_{ref})) + \left[\angle C_{ref,y} - \angle C_{ref,x}\right] \end{aligned} \tag{2.24}$$

Finally, the phase reconstructions of the two orthogonal flights are now consistent to each other and the NF-FF transformation can be applied.

Coupling between x- and y-polarized Reference Antenna

In general, the x-polarized reference antenna and the y-polarized reference antenna are coupled together and mutual coupling phenomena must be taken into account. In this case, a 2 x 2 antenna impedance matrix $\mathbf{Z}_{A,ref}$ must be considered (one port for each reference antenna polarization). Then the received voltage at the two reference antenna ports is $\mathbf{V}_{ref} = \mathbf{Z}_{RX,ref}(\mathbf{Z}_{RX,ref} + \mathbf{Z}_{A,ref})^{-1}\mathbf{V}_{ref}^{oc}$ where $\mathbf{Z}_{RX,ref}$ is the diagonal matrix with the receiver impedances for each polarization. For Pre-AAVS1 array considered in Chapter 4, because the off diagonal terms are very low with respect to diagonal terms, i.e., $|Z_{A,ref,xy}/Z_{A,ref,xx}|^2_{dB} < -40dB$ [2] then the coupling between the x and y polarized reference antenna has been neglected.

[2] $|Z_{A,ref,xx}| = |Z_{A,ref,yy}|$ by symmetry of reference antenna geometry.

Chapter 3

Far-Field Measurements

This thesis is focused on the characterization of antennas in terms of their radiation pattern from electromagnetic field measurements performed using a UAV. In this Chapter, FF measurements of a large digital beamforming antenna array are considered.

Author contribution to this work: the author partecipated in the improvement of the software that converts UAV and RF measured data into FF data (details can be found in [41]). Elaborations of UAV and RF measured data, computation of magnitude EEPs (Section 3.3), active element gain measurement (Section 3.4), synoptic visualization of magnitude EEPs (Section 3.5), computation of phase EEPs (Section 3.6) and the position error estimation method by phase pattern discrepancies (Section 3.7) is part of the work done by the author.

Motivation of this work: As the Square Kilometre Array progresses toward the construction phase, the first prototypes of the low-frequency instrument have been deployed in Australia. SKA-low will operate from 50 MHz to 350 MHz. In June 2019, a measurement campaign took place in the Murchison Radio-astronomy Observatory (MRO) area (see Fig. 3.1) to validate the electromagnetic models of two SKA-low stations. The main purpose of the measurement campaign was to validate the acquisition system and the electromagnetic models through an experimental measurement of the amplitude EEPs. Besides these high priority objectives, further scopes included the measurement of phases of EEPs. Moreover, end-to-end system verifications were performed, such as cluster position verification, correctness of port mapping and electrical connection, stability in terms of magnitude and phase stability of the RF chains, instrumental calibration. More than 10 Gbyte of data

from 14 flights have been collected in 2 days and a half. It should be noted that experimental tests using astronomical calibration sources can also be performed [54]. However, the UAV procedure provides a completely known source and an higher signal-to-noise ratio of the received signal.
This chapter is organized as follows: the considered SKA prototype stations are described in Section 3.1 together with their acquisition system. The UAV measurement setup is introduced in Section 3.2. Array elements are characterized in their magnitude EEPs (Section 3.3) and active element gains (Section 3.4). A figure of merit for the agreement between simulated and measured patterns is adopted to obtain a direct synoptic visualization of the complete dataset (see Section 3.5). Phases of EEPs are instead shown in Section 3.6. Finally, a method that computes a possible position shift of sub-arrays from phase discrepancies in EEPs is presented in Section 3.7.

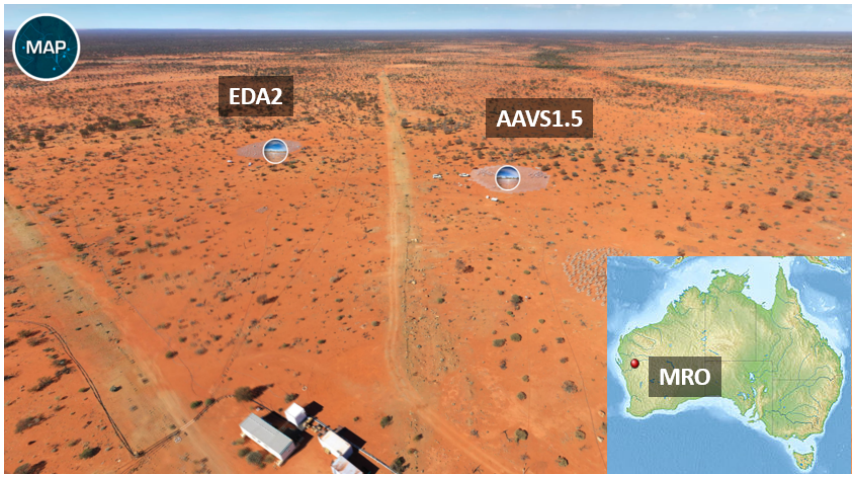

Fig. 3.1 Aerial view of the AAVS1.5 and EDA2 stations at the MRO site. Picture from https://virtualtours-external.csiro.au/MRO/.

3.1 The Antenna Under Test and Acquisition System

The two considered SKA-low stations are named Aperture Array Verification System 2.0 (AAVS2.0) and Engineering Development Array 2 (EDA2) and operate from 50 MHz to 350 MHz. Both the stations share an aperiodic (random) array layout of 256 dual-polarized antennas mounted on a ground plane with a diameter of about

40 m. When the MRO campaign was carried out, only 48 antennas of 256 were deployed in three clusters of 16 elements for AAVS2.0 (for this reason, its name was AAVS1.5), see Fig. 3.2. The EDA2 was fully deployed but only 48 antennas were connected to the receiver[1]. The AAVS1.5 is composed of dual-polarized log-periodic SKALA4.1-AL antennas [55], [15] (see Fig. 3.3), whereas EDA2 [56] is composed of dual-polarized bowtie dipoles (see Fig. 3.4). One polarization is along South-North (y-axis) direction whereas the orthogonal polarization (x-axis) is in the West-East direction. In this chapter, South-North (y-axis) polarized elements have been selected as AUT. Both AAVS1.5 and EDA2 elements are equipped with a Low Noise Amplifier (LNA) integrated on the top of the antenna and digital beamforming hardware. Groups of 16 elements (32 channels) are connected to an in-field "Smart-Box" in which the signals are converted to be transmitted via optical fiber to the control building [57]. Here, the signals are amplified, filtered, and digitized by a Tile Processing Module (TPM). Complex voltages are acquired by the TPM and stored in hdf5 files. The channel bandwidth is 0.78125 MHz that corresponds to a timestep $\Delta t_0 = 1.28 * 10^{-6}$ s between successive samples. Then by digital filtering there is an undersampling factor of 128 and an oversampling of $32/27$. The obtained timestep between two successive samples is then $\Delta t = [27 * 128/32]\Delta t_0 = 1.3824 \times 10^{-4}$ s (in the hdf5 files). This setting produces a data rate of about 27 Mbyte/min for each cluster of 16 antennas for both polarizations. As far as a UAV flight is concerned, the length of time series was about 3 min for each field cut. During the campaign more than 10 GB of data were collected in 2 days (corresponding to 14 flights). For this reason, data have been undersampled over 1024 samples (only for some computations) in order to reduce the large amount of required memory and processing time.

3.2 UAV Test Source

The UAV hereby considered is a commercial 3D Robotics X8,+ which has been customized in order to carry a frequency synthesizer, a balun and a dipole antenna (see Fig. 3.5). The UAV can perform autonomous GNSS-guided navigation according to a pre-programmed flight path. The pre-programmed flight path is specified as a set of commands contained in a text file. This text file is generated by a Matlab

[1]The disconnected elements are included in simulations of the EDA2 model.

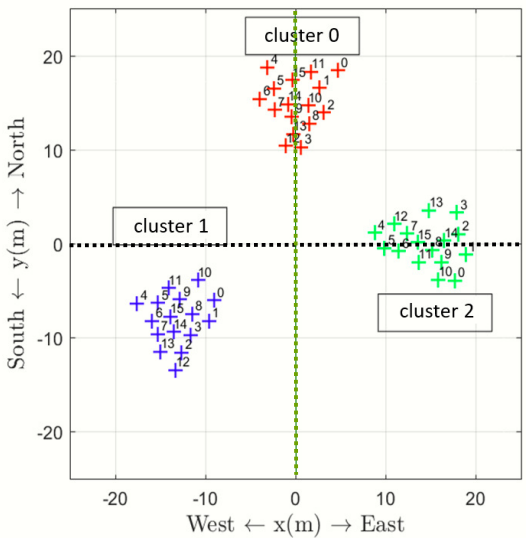

Fig. 3.2 Antenna positions of the Aperture Array Verification System 1.5 (AAVS1.5). The Engineering Development Array 2 (EDA2) share the same layout. Dashed vertical green and dashed horizontal black lines represent E-plane and H-plane (scanned by the UAV) for the South-North polarized elements, respectively.

Fig. 3.3 Log-periodic elements of the Aperture Array Verification System 1.5 (AAVS1.5).

script according to the required flight strategy. The UAV position is measured using a real-time differential GNSS system, which provides an accuracy of 2-3 centimeters. The UAV orientation is measured by the on-board Inertial Measurement Unit with an accuracy of about 2 Degrees. The UAV-mounted RF transmitter is a continuous-wave RF synthesizer with a maximum RF power of 3-7 mW and a bandwidth less than

Fig. 3.4 Bow-tie dipoles of the Engineering Development Array 2 (EDA2).

100 Hz. The synthesizer is then connected to the dipole antenna through a balun. A set of dipoles with different lengths has been manufactured. The proper dipole was used at the corresponding measurement frequency. Measurements were performed at

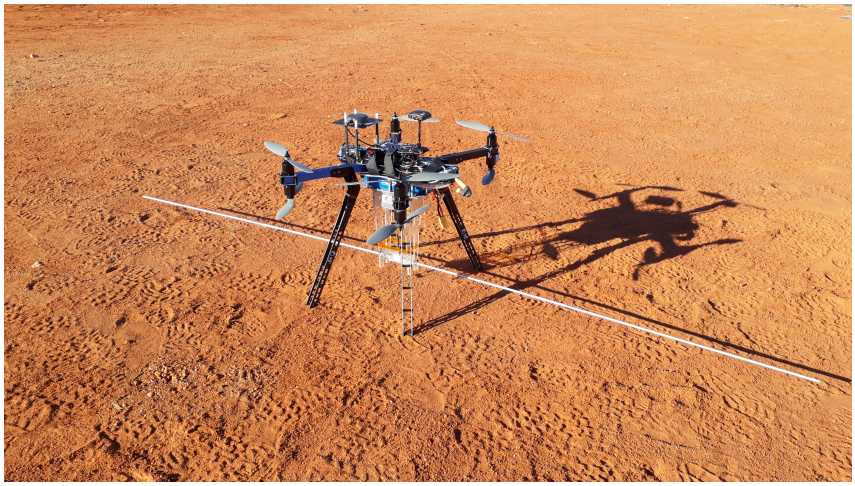

Fig. 3.5 Photo of the UAV during the measurement campaign.

50, 70, 110, 160 and 320 MHz. For each frequency, the UAV flight consisted of two orthogonal linear scans (see horizontal and vertical dashed lines in Fig. 3.2) passing

through the array center at constant height. Such a flying height was originally programmed to 160 m for all measurements. Nevertheless, some measurements were executed at 120 m due to adverse wind conditions. Through these flights, radiation patterns have been characterized within an angular coverage of ± 45 deg from zenith. The flight height regulation limit defined by CASA[2] is of 120 m. If a special authorization is available, the flight height could be extended to about 250 m. Above this value, there are some technical limits of the present UAV such as telemetry link, and overall flight duration (take-off and landing would take too much time).

Fig. 3.6 shows the FF conditions for different array sizes within the frequency range 50-320 MHz. The 10λ far-field condition is depicted with solid yellow line[3]. This condition is mainly significant at 50 MHz. The Fraunhofer distance $2D^2/\lambda$ is evaluated for one cluster of AAVS1.5 (blue) and for the full AAVS1.5 station (orange). It can be seen that the FF condition is satisfied to 160 MHz at cluster level (see Fig. 3.6). Rigorously speaking, the UAV generally flies in the NF of AAVS1.5 and EDA2 full stations. However, FF interaction between UAV and array under test has been assumed and EEPs have been extracted accordingly [58]. As it will be shown in Section 3.3, the agreement between simulated and measured EEPs is quite satisfactory. This is an indirect confirmation that the radius of influence of each array element is not very large and certainly below the sub-array diameter.

As a last remark, note that the UAV flight paths (dashed lines in Fig. 3.2)) did not lie in the E and H planes of all the clusters. Neverthless, hereinafter they are referred to as E and H planes for simplicity. Both measurements and simulations were computed on the actual measured path.

[2]The Civil Aviation Safety Authority (CASA) is the Australian authority for civil aviation regulations.

[3]The FF condition dictates that the distance between source and observation point must be much greater than λ. Here, such minimum distance is assumed to be 10λ.

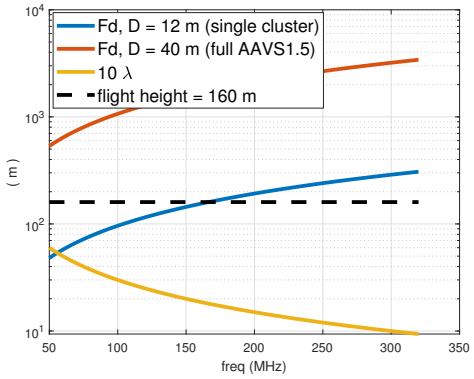

Fig. 3.6 Fraunhofer distance (Fd) $2D^2/\lambda$ for single cluster (blue line) and full AAVS1.5 station (orange line) and 10λ limit (yellow line). UAV flight height was at most 160 m (dashed black line).

3.3 Embedded Element Patterns (magnitude)

EEPs were extracted from the measured power at each array element (this was possible through the full digital beam-forming hardware described in Section 3.1) through the procedure described in [41], [58]. For the sake of completness, a brief introduction on the AUT gain computation from UAV-based FF measurements is here reported. The gain g_{AUT} of the AUT can be extracted from the transmission link equation (also known as Friis equation) between AUT and UAV-mounted source

$$\frac{P_{RX}(\mathbf{r},\boldsymbol{\gamma})}{P_{TX}} = \frac{g_{AUT}(\hat{\mathbf{r}})g_s(\hat{\mathbf{r}},\boldsymbol{\gamma})}{(\frac{4\pi r}{\lambda})^2}|\hat{\mathbf{p}}_{AUT}(\hat{\mathbf{r}})\cdot\hat{\mathbf{p}}_s(\hat{\mathbf{r}},\boldsymbol{\gamma})|^2 \tag{3.1}$$

where P_{RX} is the available (measured) power at the AUT which depends on the position vector $\mathbf{r} = r\hat{\mathbf{r}}$ from the AUT to the UAV and the UAV orientation $\boldsymbol{\gamma}$, P_{TX} and g_s are the transmitted power and gain of the UAV-mounted source antenna, $\hat{\mathbf{p}}_s$ and $\hat{\mathbf{p}}_{AUT}$ are the polarization unit vectors of source and AUT and λ is the free-space wavelength. The UAV orientation $\boldsymbol{\gamma}$ is specified through a set of three angles (yaw, pitch and roll) [41]. A possible impedance mismatch factor between AUT and receiver is understood inside P_{RX}. A free-space approximation is also assumed (reflections of the ground are not considered).

Let's consider unit vectors $\hat{\mathbf{u}},\hat{\mathbf{v}} : S^2 \longrightarrow \mathbb{R}^3$ such that $\{\hat{\mathbf{u}}(\hat{\mathbf{r}}),\hat{\mathbf{v}}(\hat{\mathbf{r}})\}$ forms a basis of the plane (passing through the origin) with unit normal vector $\hat{\mathbf{r}}$, where S^2 is the sphere of unit radius in $\mathbb{R}^3$ (e.g., $\hat{\mathbf{u}} = \hat{\theta}$, $\hat{\mathbf{v}} = \hat{\phi}$ can be the unit vectors of spherical

coordinates). Polarization unit vectors can be written as $\hat{\mathbf{p}}_s = \hat{p}_{s,v}\hat{\mathbf{v}} + \hat{p}_{s,u}\hat{\mathbf{u}}$ and $\hat{\mathbf{p}}_{AUT} = \hat{p}_{AUT,v}\hat{\mathbf{v}} + \hat{p}_{AUT,u}\hat{\mathbf{u}}$. If the source is linearly polarized along the unit vector $\hat{\mathbf{v}}$, i.e., $\hat{\mathbf{p}}_s = \hat{p}_{s,v}\hat{\mathbf{v}}$, then the partial AUT gain $g_{AUT,v} = g_{AUT}|\hat{p}_{AUT,v}|^2$ along the direction $\hat{\mathbf{v}}$ can be extracted from (3.1) by

$$g_{AUT,v}(\hat{\mathbf{r}}) = \left(\frac{4\pi r}{\lambda}\right)^2 \frac{1}{g_s(\hat{\mathbf{r}}, \boldsymbol{\gamma})} \frac{P_{RX}(\mathbf{r}, \boldsymbol{\gamma})}{P_{TX}} \tag{3.2}$$

Through knowledge on the UAV position $\mathbf{r}$, the orientation $\boldsymbol{\gamma}$ and source gain g_s, the AUT gain $g_{AUT,v}$ is finally computed from (3.2). This approach will be also adopted in Chapter 4 to obtain the AUT gain from FF measurements. From now on, the EEPs extracted from measurements using (3.2) are referred to as the measured EEPs.
E-plane and H-plane measured EEPs at 50, 70, 160, 320 MHz of elements 8, 12, 13, 15 for cluster #0, #1 and #2 are shown with blue lines in Fig. 3.7, 3.8, 3.9, 3.10, 3.11 and 3.12, respectively. Elements 8 and 15 are located in the inner part of the clusters whereas elements 12 and 13 are located near their boundaries (see Fig. 3.2). In each figure, rows refers to frequencies (50, 70, 160, 320 MHz) whereas columns to elements (8, 12, 13, 15). Each curve is normalized to its maximum. For the sake of comparison, simulated EEPs are shown with dashed black lines. Good agreement can be observed between measured and simulated EEPs. As previously mentioned, these cuts (see dashed lines in 3.2) are not E-plane and H-planes for all the clusters, e.g., the South-North cut (see green dashed line in 3.2) made by the UAV does not pass over cluster #1 and #2. However, both measurements and simulations were computed on the actual measured path.
It can be seen that some curves are not reported in a little angular region around zenith (for zenith angles near zero), e.g., see Fig. 3.8. This is because the UAV did not exactly pass above the array center, i.e., in the point $(x = 0, y = 0, z = h)$, where h is the UAV altitude. For this reason, samples near zenith were not acquired.
It can be seen that some measured EEPs suffer from some peaks, e.g., element 13 at 50 MHz in Fig. 3.7 (first row, third column). These peaks are already present in the measured power and are related to wrong time labels assigned to packets in the receiving acquisition system. This confirms the capability of the proposed end-to-end procedure to find issues in the complete system under test (i.e., antennas with acquisition system).

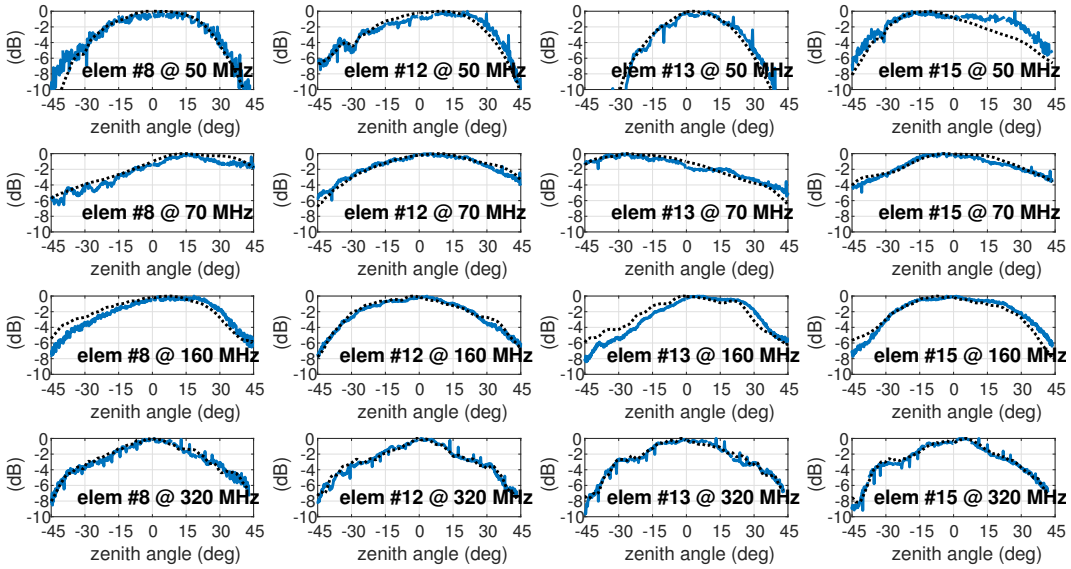

Fig. 3.7 Normalized E-plane Embedded Element Patterns (magnitude) of the four South-North polarized elements (8, 12, 13, 15) in cluster #0 of AAVS1.5 at 50, 70 MHz, 160 and 320 MHz. Columns refer to different frequencies, whereas rows to different array elements. Blue: measurements, dashed black: simulations.

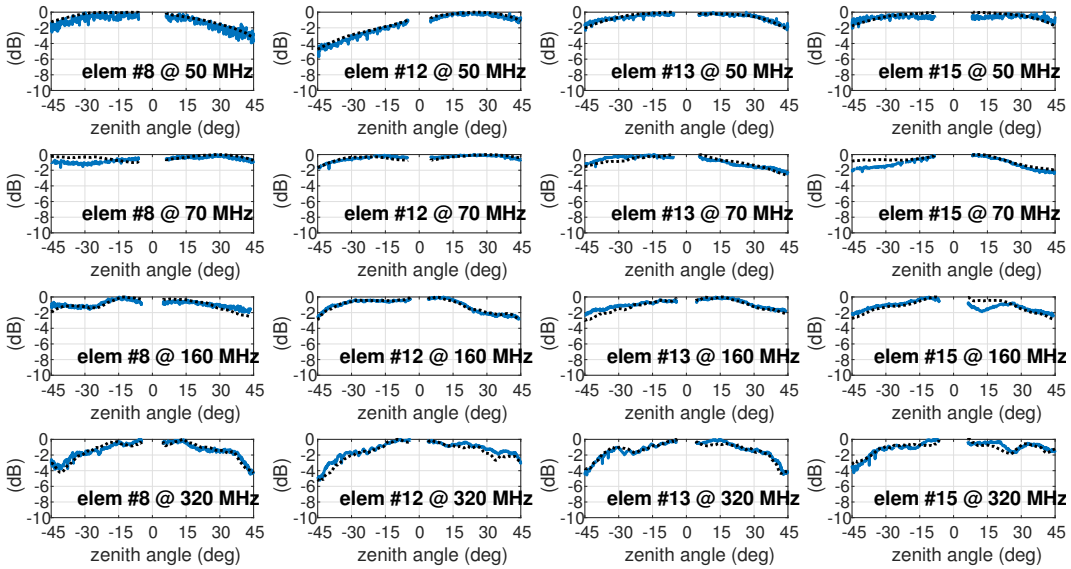

Fig. 3.8 Normalized H-plane Embedded Element Patterns (magnitude) of the four South-North polarized elements (8, 12, 13, 15) in cluster #0 of AAVS1.5 at 50, 70 MHz, 160 and 320 MHz. Columns refer to different frequencies, whereas rows to different array elements. Blue: measurements, dashed black: simulations.

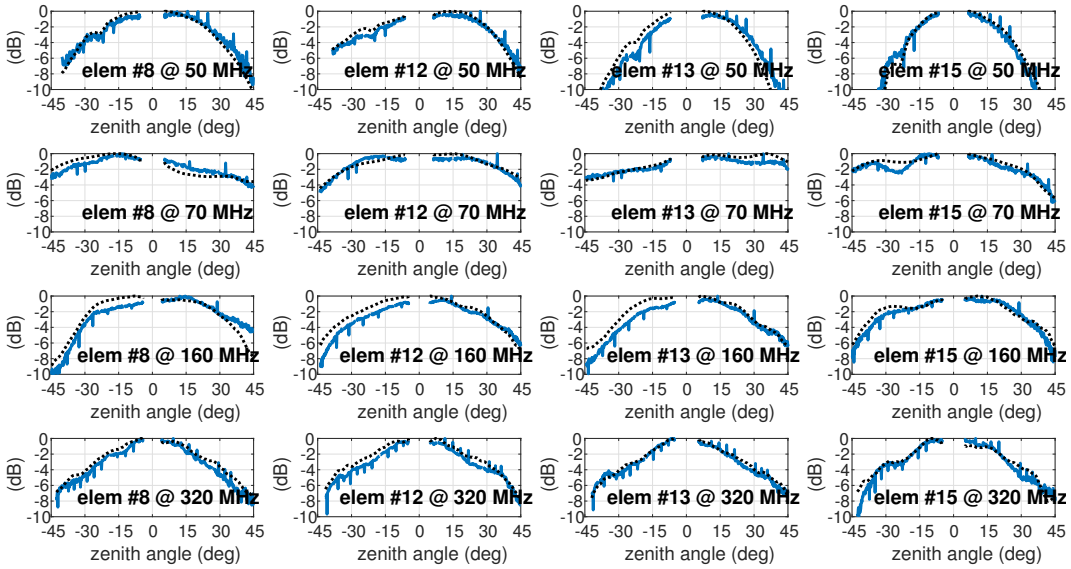

Fig. 3.9 Normalized E-plane Embedded Element Patterns (magnitude) of the four South-North polarized elements (8, 12, 13, 15) in cluster #1 of AAVS1.5 at 50, 70 MHz, 160 and 320 MHz. Columns refer to different frequencies, whereas rows to different array elements. Blue: measurements, dashed black: simulations.

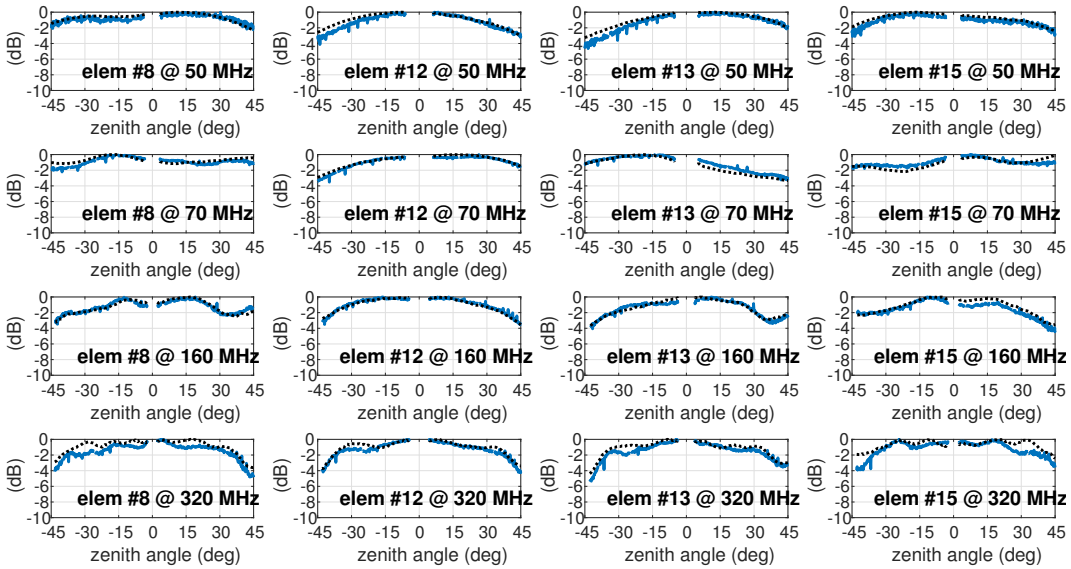

Fig. 3.10 Normalized H-plane Embedded Element Patterns (magnitude) of the four South-North polarized elements (8, 12, 13, 15) in cluster #1 of AAVS1.5 at 50, 70 MHz, 160 and 320 MHz. Columns refer to different frequencies, whereas rows to different array elements. Blue: measurements, dashed black: simulations.

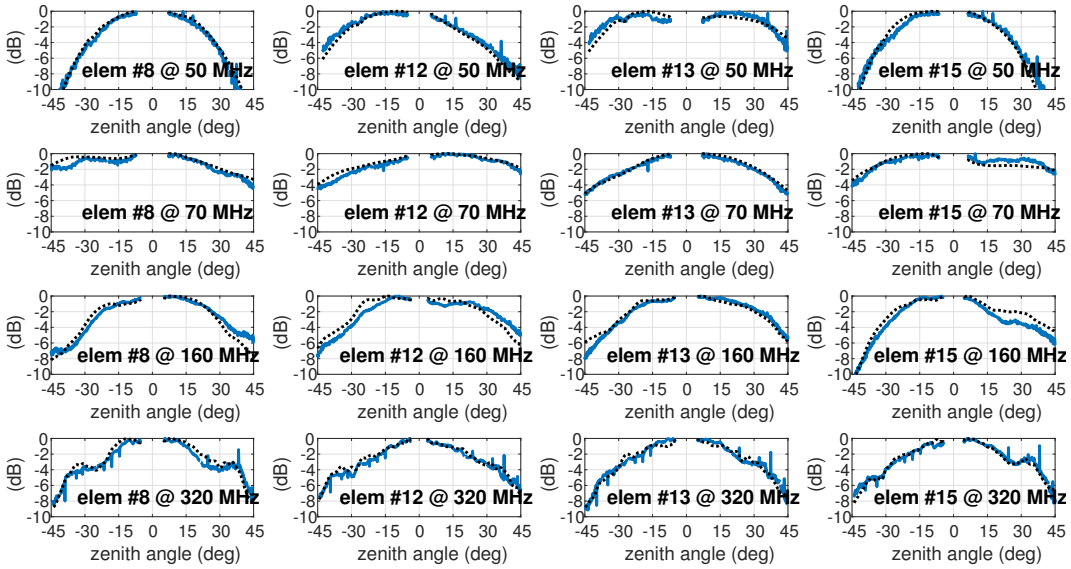

Fig. 3.11 Normalized E-plane Embedded Element Patterns (magnitude) of the four South-North polarized elements (8, 12, 13, 15) in cluster #2 of AAVS1.5 at 50, 70 MHz, 160 and 320 MHz. Columns refer to different frequencies, whereas rows to different array elements. Blue: measurements, dashed black: simulations.

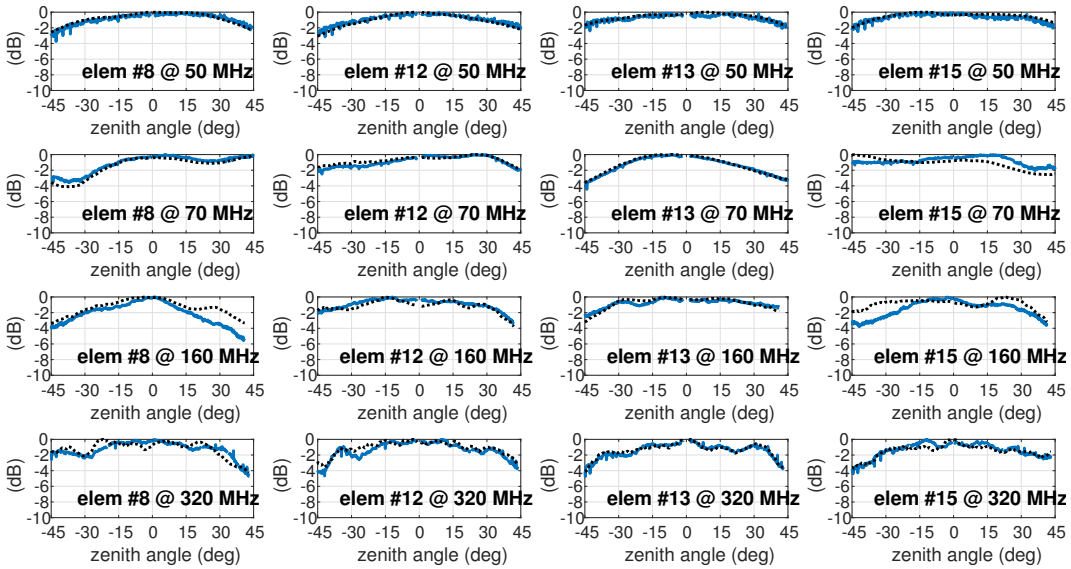

Fig. 3.12 Normalized H-plane Embedded Element Patterns (magnitude) of the four South-North polarized elements (8, 12, 13, 15) in cluster #2 of AAVS1.5 at 50, 70 MHz, 160 and 320 MHz. Columns refer to different frequencies, whereas rows to different array elements. Blue: measurements, dashed black: simulations.

3.4 Active Element Gain Measurement

Part of the work presented in this Section has been previously published in [14].
In this Section, the active element gain of one element of AAVS1.5 and EDA2 is estimated from measurements. Here, such gain is referred to the whole structure before the receiver, i.e., antenna with its LNA and cable. The active element gain has been extracted using both a UAV flight and a reference measurement. In the latter, the transmitter was directly connected to the receiver. In this way, the unknown contributions (i.e., the transmitted power P_{TX} and receiver gain g_{RX}) have been calibrated out through the reference measurement. Knowledge of the devices used during the campaign (e.g., attenuators, balun, source antenna) have been also exploited.
For simplicity, each device has been modeled as ideal. For example, each attenuator has been modeled by a scattering matrix $\mathbf{S}'$ with zero diagonal entries

$$\mathbf{S}' = \begin{pmatrix} 0 & S'_{12} \\ S'_{21} & 0 \end{pmatrix} \tag{3.3}$$

Through this assumption, the scattering parameter S_{21} of two connected devices is simply the multiplication of the scattering parameters of the single devices, i.e., $S_{21} = S'_{21}S''_{21}$, where S'_{21} and S''_{21} are the scattering parameters 21 of the first and second device, respectively. Furthermore, assuming an impedance matched load, the output (active) power P_{out} of the global device is related to the input power P_{in} through $P_{out} = |S_{21}|^2 P_{in}$. In dBm, this relation simply becomes a summation, i.e.,

$$\begin{aligned} 10\log_{10}\frac{P_{out}}{1mW} &= 20\log_{10}|S_{21}| + 10\log_{10}\frac{P_{in}}{1mW} = \\ &= 20\log_{10}|S'_{21}| + 20\log_{10}|S''_{21}| + 10\log_{10}\frac{P_{in}}{1mW} \end{aligned} \tag{3.4}$$

The same argument has been used for the in-flight RF chain in Fig. 3.13. The received (measured) power P_{RX} is related to the transmitted power P_{TX} by (dB units are understood)

$$P_{RX} = P_{TX} - A_{TX} - A_{balun} + g_s - A_{mis} - PL + g_{AUT} + g_{LNA} - A_{cable} - A_{RX} + g_{RX} \tag{3.5}$$

where A_{TX}, A_{RX} are attenuations of the attenuators used during the campaing (one located after the transmitter and one before the receiver, see Fig. 3.13). g_{AUT}, g_{LNA}

g_s, g_{RX} are gain values of the AUT, LNA, UAV-mounted source antenna and receiver, respectively[4]. Values A_{balun}, A_{mis}, PL, A_{cable} are attenuations of the balun, AUT-source mismatch, path loss and cable, respectively.
The reference measurement [59] was exploited to calibrate out the unknown contributions, i.e., the transmitted power P_{TX} and receiver gain g_{RX}. In this reference measurement, the UAV-mounted synthesizer was directly connected to the input of the receiver chain (i.e., input of the smartbox, where the cables of array elements are collected). Two attenuators (with attenuations $A_{TX,ref}$ and $A_{RX,ref}$) were exploited between transmitter and receiver. Hence, the reference power P_{Ref} measured during the reference measurement (see Fig. 3.14) is related to the transmitter power P_{TX} through

$$P_{Ref} = P_{TX} - A_{TX,ref} - A_{RX,ref} + g_{RX} \tag{3.6}$$

Performing the difference between equations (3.5) and (3.6), the active element gain $g_{AUT} + g_{LNA} - A_{cable}$ is computed from

$$\begin{aligned} g_{AUT} + g_{LNA} - A_{cable} = P_{RX} - P_{Ref} + A_{TX} + A_{balun} + A_{mis} + PL + \\ + A_{RX} - A_{TX,ref} - A_{RX,ref} - g_s \end{aligned} \tag{3.7}$$

The measured (by (3.7)) and simulated active element gain of the South-North polarized element 8 in cluster #2 of AAVS1.5 are shown in table 3.1. The same procedure has been applied to the South-North polarized element number 2 in cluster #2 of EDA2, see table 3.2. Discrepancies at 50 and 70 MHz could be due to the mismatched dipole mounted on the UAV. The error for the considered element of AAVS1.5 generally decreases at higher frequencies, whereas the EDA2 element shows a more variable discrepancy. The error may be improved with a further refinement of the considered models, with particularly for the interaction between LNA and the antenna.

[4]Rigorously speaking, because the source is linearly polarized in the considered UAV paths (see dashed lines in Fig. 3.2), i.e., $g_s \simeq g_{s,co}$, the extracted AUT gain is the co-polar gain $g_{AUT,co}$ and not the overall gain $g_{AUT} = g_{AUT,co} + g_{AUT,cx}$ as reported in (3.5). However, if $g_{AUT,cx} \simeq 0$ then $g_{AUT,co} \simeq g_{AUT}$.

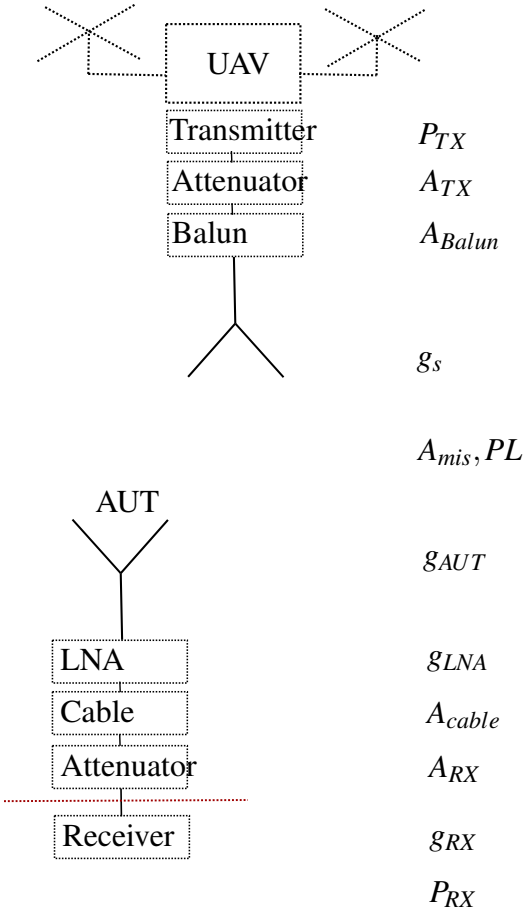

Fig. 3.13 Schematic diagram of the in-flight RF measurement chain. On the right: quantities considered for the active element gain measurement, see (3.5). Dashed red horizontal line represents the section where reference measurement was made.

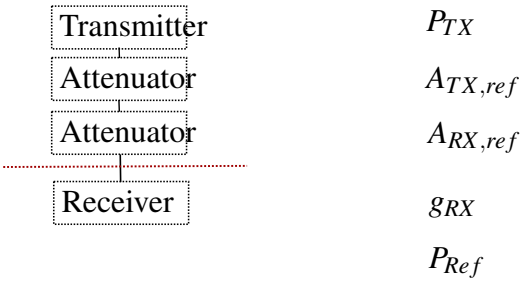

Fig. 3.14 Schematic diagram of the reference RF measurement. On the right: quantities considered for the active element gain measurement, see (3.6).

Table 3.1 Measured and simulated active element gain at zenith for element 8 (South-North polarization) in cluster #2 of AAVS1.5. Table from [14].

Frequency (MHz)	Measured gain (dBi)	Simulated gain (dBi)	Discrepancy (dB)
50	34.29	36.47	-2.18
70	46.69	48.80	-2.11
110	52.52	51.90	0.62
160	51.58	52.24	-0.66
320	50.50	49.92	0.58

Table 3.2 Measured and simulated active element gain at zenith for element 2 (South-North polarization) in cluster #2 of EDA2. Table from [14].

Frequency (MHz)	Measured gain (dBi)	Simulated gain (dBi)	Discrepancy (dB)
50	-3.81	-1.99	-1.82
70	17.04	14.48	2.57
110	19.94	18.88	1.06
160	26.23	26.30	-0.07
320	20.44	24.06	3.61

3.5 Synoptic Visualization for Magnitude EEPs

Part of the work presented in this Section has been previously published in [14].
Magnitude of E-plane EEPs have been shown in Section 3.3. In order to provide a synoptic visualization for the discrepancy between simulated and measured E-plane EEPs, the Root Mean Square (RMS) of the logarithmic difference (RMS discrepancy hereinafter) between simulated and measured EEPs was adopted as a figure of merit. To allow for a direct comparison of the agreement between measurements and simulations regardless of the level (which depends on the receiver gain and transmitted power, see Section 3.4), EEPs must be equalized somehow before the computation of the RMS discrepancy. Due to the presence of peaks in some measured EEPs (see Section 3.3), EEPs were not normalized to the their maximum. Instead, a constant gain g_{shift} is added to each measured EEP in order to minimize the RMS discrepancy. The constant gain g_{shift} for the EEPs normalization[5] has been computed

[5]the constant gain g_{shift} depends on the chosen element. Considered the element number n, it will be denoted as $g_{shift,n}$ in the next part. It should be noted that the constant g_{shift} is used only for plot purposes in order to compare simulated and measured patterns; g_{shift} does not represent the gain of an array element.

from

$$g_{shift} = \sum_{n=1}^{N} 20\log_{10}|e_{sim}(\theta_n)| - 20\log_{10}|e_{meas}(\theta_n)| \tag{3.8}$$

where e_{meas} and e_{sim} denote the measured and simulated E-plane EEP of a selected element and θ_n are the zenith angles where the EEPs are sampled (the number of samples N is approximately 400). The equalized measured pattern is hence defined as $20\log_{10}|e^{eq}_{meas}(\theta_n)| = g_{shift} + 20\log_{10}|e_{meas}(\theta_n)|$. The logarithmic difference (see (6) in [60]) between the simulated and measured pattern is then considered

$$logdiff(\theta_n) = 20\log_{10}|e_{sim}(\theta_n)| - 20\log_{10}|e^{eq}_{meas}(\theta_n)| \tag{3.9}$$

Logarithmic difference between the simulated (dashed black line) and equalized measured pattern (solid blue line) is reported with yellow line in Fig. 3.15 for element 8 in cluster 0 at 320 MHz. Finally, the RMS discrepancy is computed as the

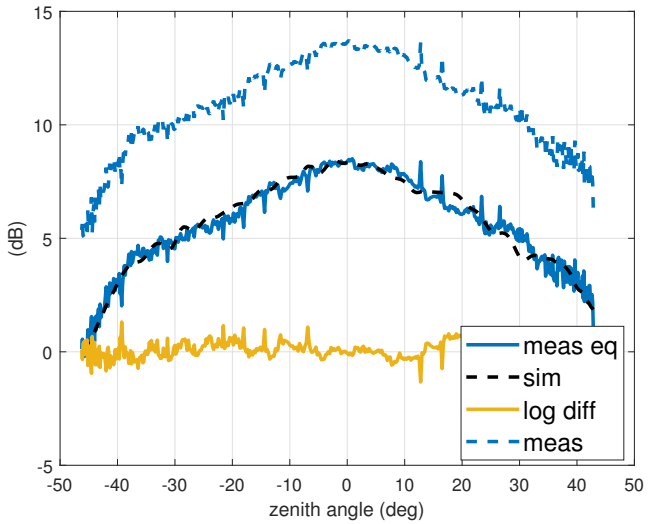

Fig. 3.15 Simulated, measured (without equalization) and equalized measured E-plane EEPs at 320 MHz of element 8 in cluster 0 are reported with dashed black, dashed blue and solid blue lines, respectively. Yellow line: logarithmic difference between simulated and equalized measured EEPs (see (3.9)).

RMS of the logarithmic difference, i.e.,

$$\sqrt{\frac{1}{N}\sum_{n=1}^{N}\Big(logdiff(\theta_n)\Big)^2} \tag{3.10}$$

The RMS discrepancies computed by (3.10) are shown with cyan or magenta dots in Fig. 3.16 and 3.17 for all elements of AAVS1.5 and EDA2, respectively. Each cluster or frequency is arranged in a different row or column. Larger values are concentrated at 50 MHz and 160 MHz for AAVS1.5 and at 320 MHz for EDA2. The magenta dots of some elements of EDA2 at 70 MHz indicate that the low-noise amplifier (LNA) at the antenna level was close to the saturation point. The clipped signal caused a distortion in the measured pattern; however, the final RMS was still comparable to the other elements.
In Fig. 3.16 and 3.17, the bars report instead the measured relative active element gain distribution. Element 8 of cluster 2 and element 2 of cluster 2 were adopted as gain reference antennas for AAVS1.5 and EDA2, respectively[6], to focus the analysis on the relative differences between the array elements. The constant gain g_{shift} computed through (3.8) of these gain reference elements is denoted with g_{ref}. For each element (say the n-th element), the quantity $(g_{ref} - g_{shift,n})$ is shown in Fig. 3.16 and 3.17 with blue bars. The low gain level of element 14 of AAVS1.5 (black bar) highlights a damage in the optical link between the LNA and the receiver that caused a high signal loss. Other elements show a considerably low gain (e.g., EDA2, 10 of cluster 0 and 15 of cluster 1), which reduces the signal-to-noise ratio, increasing the RMS discrepancy.
As a last remark, the quality of the UAV flight obviously affects the measured EEPs, e.g., an abrupt movement of the UAV that is not properly sampled could result in a poor reconstruction of the measured EEPs. In the last row of Fig. 3.16 and 3.17, a plot concering the UAV flight quality for each frequency is reported. As a figure of merit, the maximum deviation from average (orange histogram) and the Root Mean Square of the deviation from average (blue histogram) have been adopted for the three UAV angles (yaw, pitch and roll [41]). Even though the adverse wind conditions, a good overall quality of the UAV flights can be observed.

[6] the measured active element gain of these elements is shown in Section 3.4

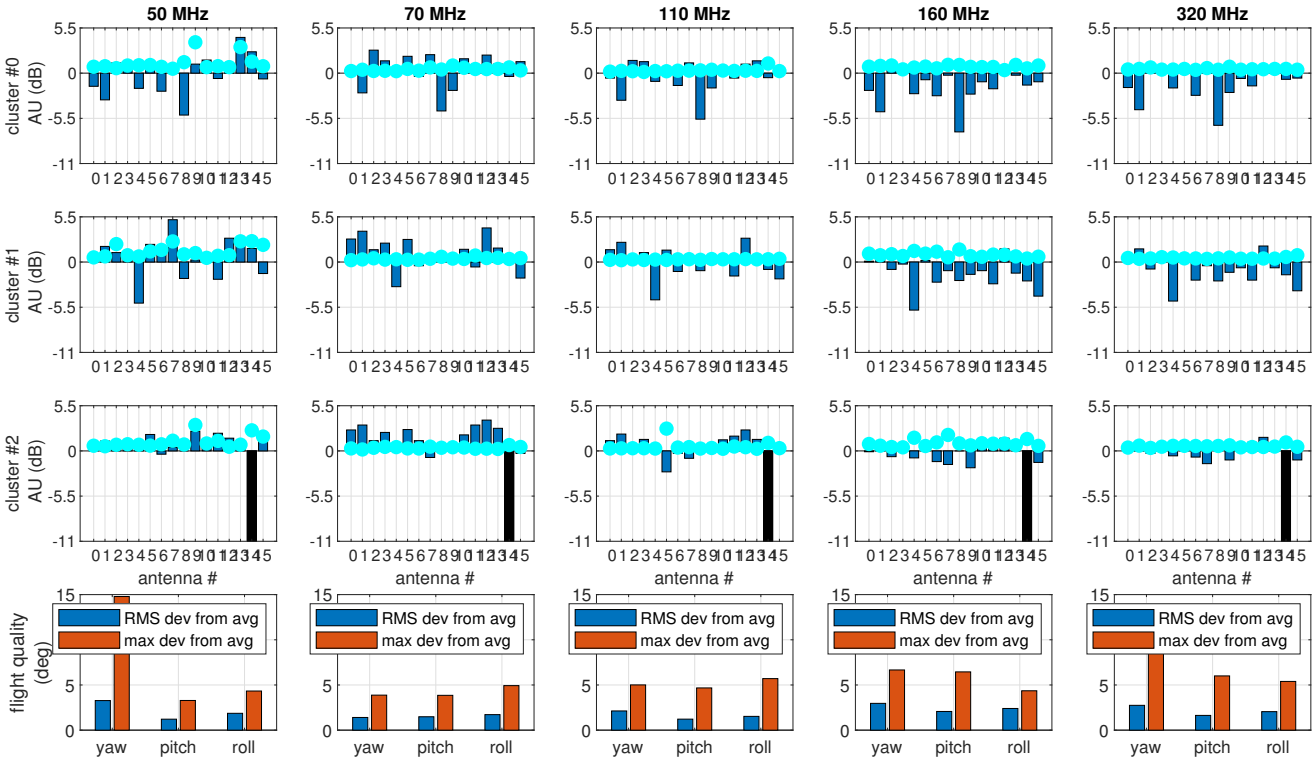

Fig. 3.16 Synoptic visualization of the AAVS1.5 results. Clusters from 0 to 2 in each row. Frequencies from 50 MHz to 320 MHz in each column. Dots: RMS discrepancy between measured and simulated EEP. Bars: measured relative active element gain. The actual value of the black bar is out of range (damaged wired link). Picture from [14].

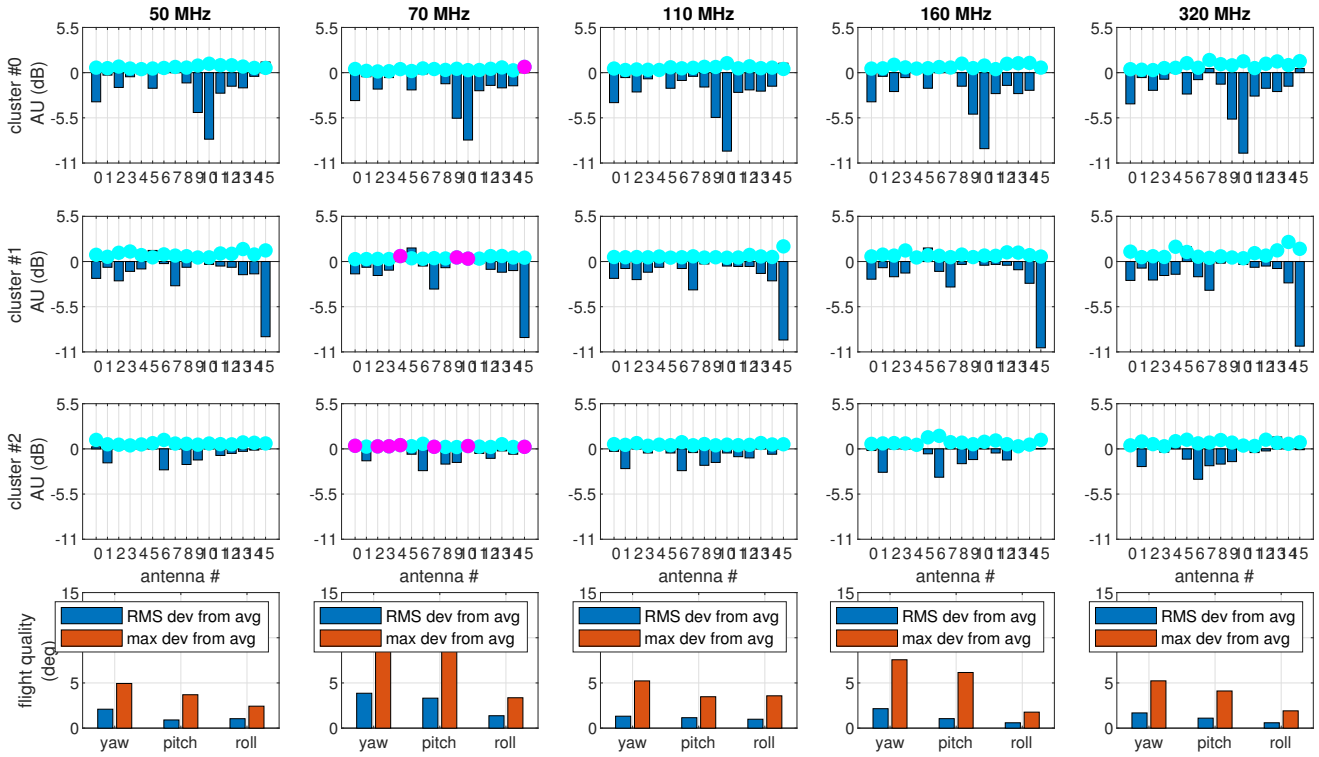

Fig. 3.17 Synoptic visualization of the EDA2 results. Clusters from 0 to 2 in each row. Frequencies from 50 MHz to 320 MHz in each column. Dots: RMS discrepancy between measured and simulated EEP. Bars: measured relative active element gain. Picture from [14].

3.6 Embedded Element Patterns (phase)

Magnitude of EEPs have been already shown in Section 3.3. In this Section, phases of EEPs are instead considered. The highest measured frequency, i.e., 320MHz, has been selected because of the larger variations in the phase patterns (at lower frequencies phase patterns are more flat). It should be noted that the transmitter on the UAV is not phase-locked to the receiver on the ground. Then, the phase of the received signal is constantly drifting with respect to the receiver reference. For this reason, phase patterns were computed through the procedure described in Chapter 2 (see (2.16)) using element 0 of cluster #2 (South-North polarization) as reference antenna. A full-wave simulation of its EEP has been used as known information in order to retrieve phases of EEPs for the other elements. In this way, mutual coupling phenomena between the reference element and array have been taken into account. Our choice of a reference antenna inside the cluster was dictated by the absence of an isolated and calibrated reference antenna outside the array (reference antenna outside the array is exploited in chapter 4).
Phases of H-plane measured EEPs (co-polar component) at 320 MHz of elements 8, 12, 13, 15 are shown with blue lines in Fig. 3.18, 3.19, 3.20 for cluster #0, #1 and #2, respectively. For the sake of comparison, simulations are reported with dashed black lines. Differences between simulations and measurements are reported with orange lines in Fig. 3.18, 3.19, 3.20. An overall good agreement between measurement and simulations for cluster #0 and #2 can be observed. On the contrary, phases of cluster # 1 (see orange curves in Fig. 3.19) present more significant discrepancies with respect to cluster #0 and #2. Such discrepancies (which resemble a function of parabolic type) are in the order of ± 40 deg. It should be mentioned that this value is significant for beamforming performance. In Section 3.7, these phase discrepancies will be explained in terms of a possible position shift of the entire cluster #1 (with respect to its nominal position).
As previously mentioned in Section 3.3, a little portion of measured data suffered from peaks (e.g., see element 13 in Fig. 3.18). This issue was due to wrong time labels assigned to packets in the receiving acquisition system.

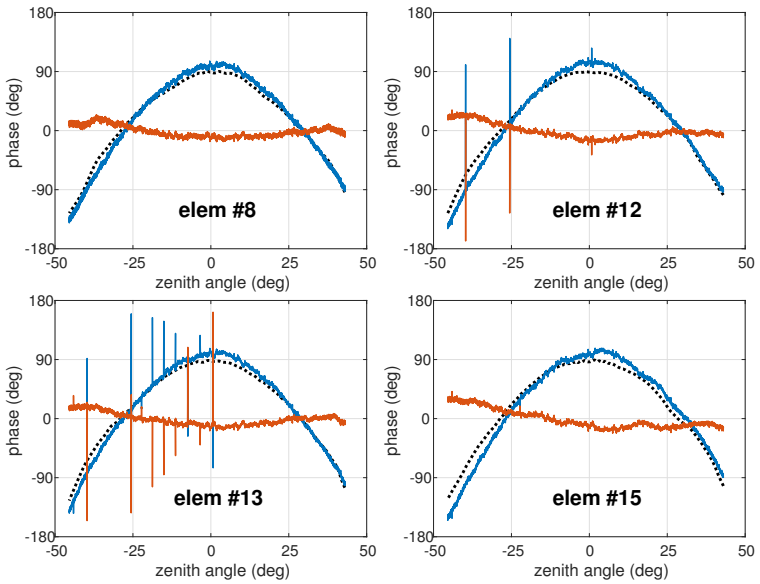

Fig. 3.18 H-plane Embedded Element Patterns (phase) of the four South-North polarized elements (8, 12, 13, 15) in cluster #0 of AAVS1.5 at 320 MHz. Blue: measurements, dashed black: simulations, yellow: their difference.

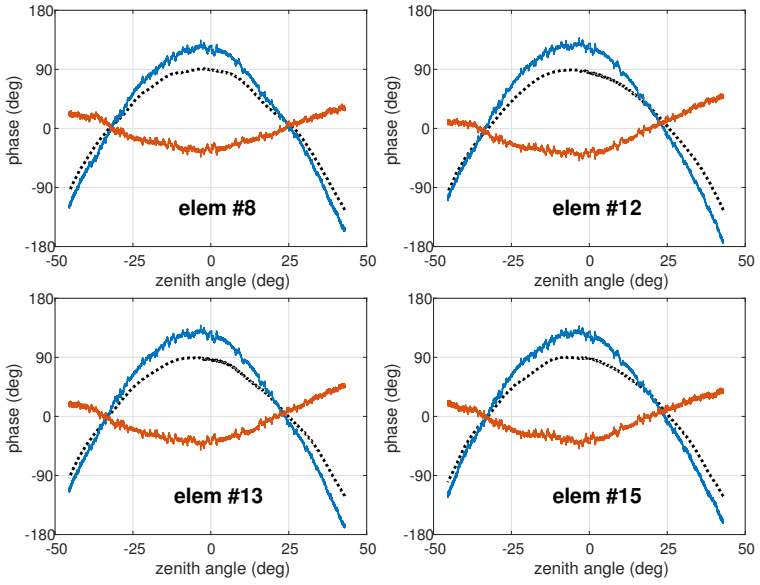

Fig. 3.19 H-plane Embedded Element Patterns (phase) of the four South-North polarized elements (8, 12, 13, 15) in cluster #1 of AAVS1.5 at 320 MHz. Blue: measurements, dashed black: simulations, yellow: their difference.

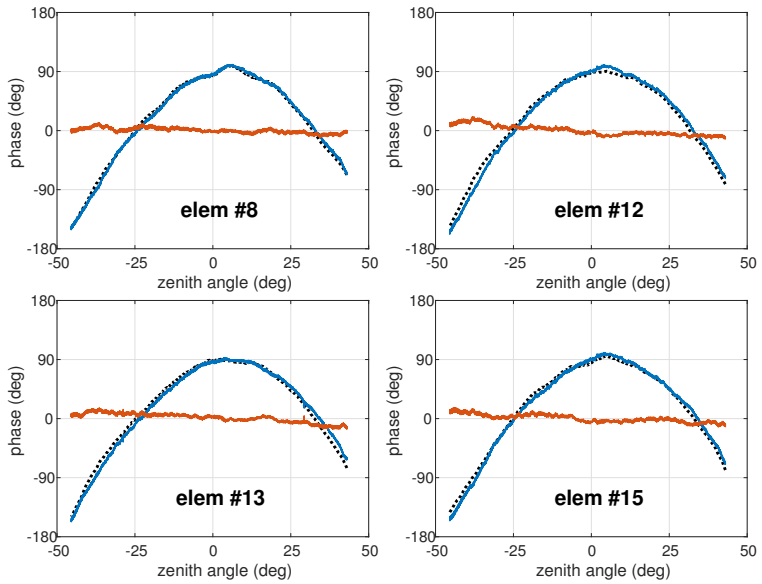

Fig. 3.20 H-plane Embedded Element Patterns (phase) of the four South-North polarized elements (8, 12, 13, 15) in cluster #2 of AAVS1.5 at 320 MHz. Blue: measurements, dashed black: simulations, orange: their difference.

3.7 Position Error Estimation of Array Clusters by Phase Discrepancies in EEPs

Part of the work presented in this Section has been already published in [61]. Phases of H-plane EEPs have been already shown in Section 3.6. In this Section, phase discrepancies between measured and simulated EEPs are attributed to a position offset (with respect to the nominal position) common to all elements belonging to the same cluster. A method that estimates this position shift is presented and applied. The resulting position shift could be due to both non-regularity (non-flatness) of the ground and installation errors.

3.7.1 Fitting Strategy

For the considered H-plane cut, the UAV-flight is close to a linear path along West-East (x-axis) direction at constant altitude (see dashed black line in Fig. 3.2). For this reason, cartesian coordinates xz (with origin centered on the reference antenna) to denote the UAV position are used. In these coordinates, the nominal position

of the AUT is denoted with $(x_{aut}, y_{aut}, 0)$ whereas $(x_{aut}, y_{aut}, 0) - (\Delta_x, \Delta_y, \Delta_z)$ is the perturbed position i.e., affected by the position error $(\Delta_x, \Delta_y, \Delta_z)$. The position of the UAV is represented by the vector $(x, 0, z)$ whereas R_{aut} and r_{aut} denote the nominal and perturbed distance between the AUT and the UAV[7]. The dependency of variables on xz is understood. Assuming a small position error $(\Delta_x, \Delta_y, \Delta_z)$, the distance r_{aut} can be approximated as

$$\begin{aligned} r_{aut} &= \sqrt{(x_{aut} - \Delta_x - x)^2 + (y_{aut} - \Delta_y)^2 + (z + \Delta_z)^2} = \\ &\sqrt{x_{aut}^2 + \Delta_x^2 + x^2 - 2x_{aut}\Delta_x - 2x_{aut}x + 2\Delta_x x + + y_{aut}^2 + \Delta_y^2 - 2y_{aut}\Delta_y + z^2 + \Delta_z^2 + 2z\Delta z} \simeq \\ &\simeq \sqrt{x_{aut}^2 + x^2 - 2x_{aut}\Delta_x - 2x_{aut}x + 2\Delta_x x + + y_{aut}^2 - 2y_{aut}\Delta_y + z^2 + 2z\Delta z} = \\ &= R_{aut}\sqrt{1 + 2\frac{(x - x_{aut})\Delta_x - y_{aut}\Delta_y + z\Delta_z}{R_{aut}^2}} \simeq R_{aut} + \frac{x - x_{aut}}{R_{aut}}\Delta_x - \frac{y_{aut}}{R_{aut}}\Delta_y + \frac{z}{R_{aut}}\Delta_z \end{aligned} \tag{3.11}$$

where terms Δ_x^2, Δ_y^2, Δ_z^2 have been neglected and a 1st order Taylor expansion[8] $\sqrt{1+x} \simeq 1 + x/2$ has been used. It should be noted that the term y_{aut}/R_{aut} is smaller and practically constant (only R_{aut} depends on the UAV position xz) with respect to the other terms $(x - x_{aut})/R_{aut}$ and z/R_{aut}. Hence, the variation Δ_y along the y-axis was not considered in this fitting strategy because its contribution (for the considered UAV-path along the x-axis) is almost constant and its variation is negligible with respect to the other errors. For this reason, (3.11) was applied with $\Delta_y = 0$.
The position of the UAV is known through a Real Time Kinematic (RTK) differential GNSS that provides centimeter-level accuracy. These data together with the nominal antenna position are used to compute R_{aut} and the distance r_{ref} between source and reference antenna.

[7] It should be noted that in the present approach a different distance R_{aut} is considered for each array element. It is clear that the simulation of the EEP phase must be performed with the considered array element in the origin (simulations for different elements do not share the same origin). Similarly, a distance R (equal for all array elements) from source to the cluster center could be adopted. In the latter case, simulations must be performed (for all array elements) with the origin coinciding with the cluster center.

[8] assuming $|(x - x_{aut})\Delta_x - y_{aut}\Delta_y + z\Delta_z|/R_{aut}^2 << 1$

Substituting (3.11) in (2.16)[9], one obtains

$$\begin{aligned}\angle\hat{p}_{aut,v} + \angle V_{ref}^{oc} - \angle V_{aut}^{oc} - \angle(\hat{\mathbf{p}}_{ref} \cdot \hat{\mathbf{p}}_s) + \angle\hat{p}_{s,v,aut} + k_0(r_{ref} - R_{aut}) = \\ = k_0 \frac{x - x_{aut}}{R_{aut}} \Delta_x + k_0 \frac{z}{R_{aut}} \Delta_z\end{aligned} \tag{3.12}$$

where r_{aut} (r_{ref}) is the distance between the considered array element (reference antenna) and the UAV, $\hat{p}_{aut,v}$ is the polarization unit vector of the considered array element, V_{aut}^{oc} and V_{ref}^{oc} are the measured voltages at the array element and reference antenna, $\hat{\mathbf{p}}_{ref}$ and $\hat{\mathbf{p}}_s$ are the polarization unit vectors of reference antenna and UAV-mounted source whereas $\hat{p}_{s,v,aut}$ is the polarization unit vector of the source (v component) toward the considered array element. For the considered array element, say the n-th element, a linear system $\mathbf{a}_n\boldsymbol{\Delta} = \mathbf{b}_n$ can be obtained by (3.12) considering all the different positions of the UAV, where $\boldsymbol{\Delta} = [\Delta_x; \Delta_z]$. Here, the symbol of semicolon ";" denotes (as in MATLAB) the operation of stacking scalars as a column vector. The term $\mathbf{b}_n$ comes from the left-hand side of (3.12). Enforcing an equal position error to a set of elements within a cluster leads to the definition of an aggregated linear system $\mathbf{A}\boldsymbol{\Delta} = \mathbf{B}$, where $\mathbf{A} = [\mathbf{a}_1; \mathbf{a}_2; \mathbf{a}_3; \dots]$ and $\mathbf{B} = [\mathbf{b}_1; \mathbf{b}_2; \mathbf{b}_3; \dots]$. This assumption models a position offset between clusters (see Fig. 3.2) due to both nonregularity (flatness) of the ground and installation errors. The linear system has to be solved in a least squares sense because $\mathbf{A}$ is rectangular.

Position Error Estimation of the UAV by Phase Discrepancies in EEPs

A similar formulation has been developed considering the UAV position offset as unknown instead of the AUT one. As in the previous Section, the considered UAV flight is a linear path along the x axis. For this reason, cartesian coordinates xz (with origin centered on the reference antenna) to denote the UAV position are used. In these coordinates, the nominal position of the UAV is denoted with $(x, 0, z)$ whereas $(x, 0, z) - (\Delta_x, \Delta_y, \Delta_z)$ is the perturbed position i.e., affected by the position error $(\Delta_x, \Delta_y, \Delta_z)$. The position of the AUT is $(x_{aut}, y_{aut}, 0)$ whereas R_{aut} and r_{aut} denote the nominal and perturbed distance between the AUT and the UAV. Similarly, R_{ref}

[9] More precisely, a little variant of (2.16) is used. The origin has been considered at the n-th array element.

and r_{ref} denote the nominal and perturbed distance between the reference antenna and the UAV. The distance r_{aut} is approximated as

$$\begin{aligned} r_{aut} = \sqrt{(x_{aut}+\Delta_x - x)^2 + (y_{aut}+\Delta_y)^2 + (z-\Delta_z)^2} = \\ \sqrt{x_{aut}^2 + \Delta_x^2 + x^2 + 2x_{aut}\Delta_x - 2x_{aut}x - 2\Delta_x x + + y_{aut}^2 + \Delta_y^2 + 2y_{aut}\Delta_y + z^2 + \Delta_z^2 - 2z\Delta z} \simeq \\ \simeq \sqrt{x_{aut}^2 + x^2 + 2x_{aut}\Delta_x - 2x_{aut}x - 2\Delta_x x + + y_{aut}^2 + 2y_{aut}\Delta_y + z^2 - 2z\Delta z} = \\ = R_{aut}\sqrt{1 + 2\frac{(x_{aut}-x)\Delta_x + y_{aut}\Delta_y - z\Delta_z}{R_{aut}^2}} \simeq R_{aut} + \frac{x_{aut}-x}{R_{aut}}\Delta_x + \frac{y_{aut}}{R_{aut}}\Delta_y - \frac{z}{R_{aut}}\Delta_z \end{aligned} \tag{3.13}$$

whereas the distance r_{ref} is approximated as

$$r_{ref} \simeq R_{ref} - \frac{x}{R_{ref}}\Delta_x - \frac{z}{R_{ref}}\Delta_z \tag{3.14}$$

Subtracting (3.14) to (3.13), one obtains

$$r_{aut} - r_{ref} \simeq R_{aut} - R_{ref} + \left(\frac{x_{aut}-x}{R_{aut}} + \frac{x}{R_{ref}}\right)\Delta_x + \frac{y_{aut}}{R_{aut}}\Delta_y + \left(-\frac{z}{R_{aut}} + \frac{z}{R_{ref}}\right)\Delta_z \tag{3.15}$$

Similarly to the previous Section, this equation can be substituted in (2.16) to obtain a linear system and compute the UAV position offset $(\Delta_x, \Delta_y, \Delta_z)$.

3.7.2 Results

The fitting method described in Section 3.7.1 has been used to explain phase discrepancies in EEPs. First, cluster #1 is considered. Results for the four considered elements 8, 12, 13, 15 of cluster #1 are shown in Fig. 3.21. The fitted phase errors (dashed black curves in Fig. 3.21) approximate well the phase discrepancies (orange curves) between measurements and simulations. The fitted position shift for cluster #1 is $\Delta_x \simeq 0.02$ m and $\Delta_z \simeq -0.62$ m. The shift along the x-axis is negligible because it is within the position measurement accuracy. On the contrary, the method predicts a significant Δ_z that could be explained by a little slope in the area of the AAVS1.5 array (the soil could be not perfectly flat).
Similar results have been obtained by using other elements of cluster 2 as reference

antenna.

The previous analysis is repeated on cluster # 2. In this case, the reference antenna (element 0 in cluster #2) is located in the same cluster of the analyzed elements (element 8, 12, 13, 15). The phase discrepancy fitting is shown in Fig. 3.22. The fitted phase error approximates well the discrepancy between measurements and simulations. In this case, the resulting position shift $\Delta_x \simeq 0.03$ m and $\Delta_z \simeq 0$ m of cluster 2 is much smaller than in cluster # 1. This is consistent with the flat ground within the subarray. Similar results, not shown here, have been achieved for cluster 0.

The fitting formulation using the UAV position offset as variable has been also applied to the data. However, the achieved offsets were not consistent with the expected differential GNSS-accuracy of few centimeters. Hence, the AUT position offset can represent a good candidate to explain the phase discrepancies. However, position measurement of reference points (e.g., array centers, UAV GNSS base-station) has been found to be affected by inaccuracies[10]. For this reason, the observed phase discrepancies in EEPs could be due to a combination of the two errors that cannot be disentangled (AUT and UAV position offset). For future works, position measurement of the reference points must be carefully performed and verified.

[10]It should be noted that the position of the UAV is computed using such reference points.

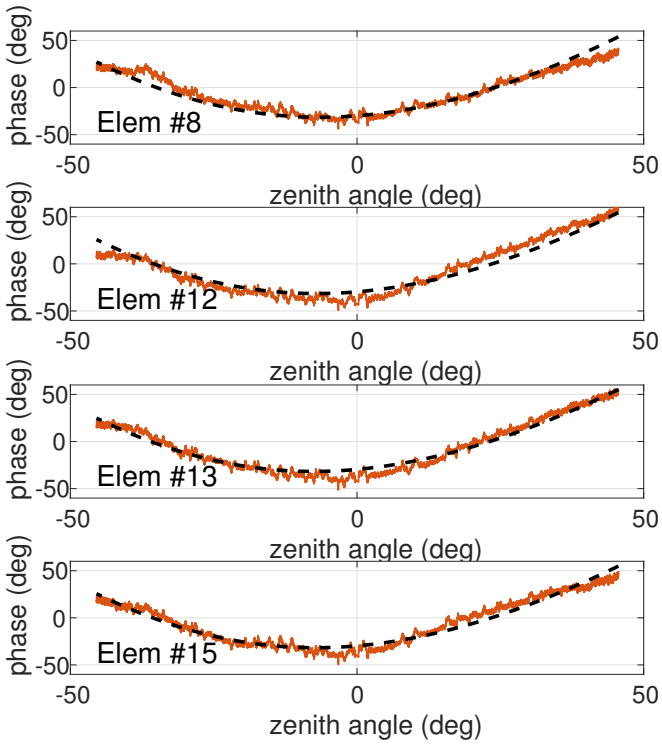

Fig. 3.21 Phase error fitting of four elements (8, 12, 13, 15) of cluster 1. Orange and dashed black curves represent the measured and reconstructed error, respectively. The estimated position shift of cluster 1 is $\Delta_x \simeq 0.02$ m and $\Delta_z \simeq$ - 0.62 m. Picture from [61].

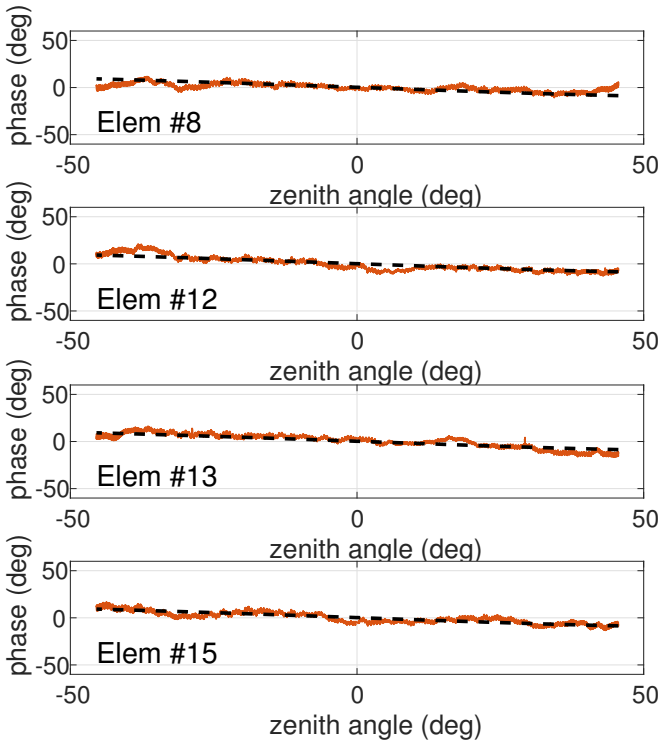

Fig. 3.22 Phase error fitting of four elements (8, 12, 13, 15) of cluster 2. Orange and dashed black curves represent the measured and reconstructed error, respectively. The estimated position shift of cluster 2 is $\Delta_x \simeq 0.03$ m and $\Delta_z \simeq 0$ m. Picture from [61].

Chapter 4

Near-Field Measurements

This thesis is focused on the characterization of antennas in terms of their radiation pattern from electromagnetic field measurements performed using a UAV. In this Chapter, FF and NF measurements of a large digital beamforming antenna array are considered.
Part of the work described in this chapter has been previously published in [34], [1].
Author contribution to this work: elaborations of UAV and RF measured data, elaboration of the inverse source NF-FF transformation data, definition and tuning of the NF-FF transformation parameters is part of the work done by the author.
Motivation of this work: the large size of this radio telescope prototype oriented the development of the large NF scanner presented in this work. Moreover, the presence of active antennas constrained the UAV to operate in TX mode. A previous prototype has been already characterized using a FF flights [62] with good results. The NF approach presented in this work has been investigated as a valuable alternative for the test of even larger arrays, e.g., SKA-low full stations. For such arrays, the FF condition cannot be reached within the flight altitude regulation limits, generally of 120 meters.
This chapter is organized as follows: the array under test and its acquisition system are described in Section 4.1 whereas the UAV-based scanner is described in Section 4.2. The NF data acquired through the UAV are presented in Section 4.3. Results of the inverse source NF-FF transformation applied on such measured NF data are discussed in Section 4.4. Finally, FF and NF flights are compared (in terms of time needed to perform the flight) in Section 4.5.

Fig. 4.1 The UAV flies over the array under test i.e., the Pre - Aperture Array Verification System. On the right (white circle): reference antenna used for phase reconstruction. Picture from [34].

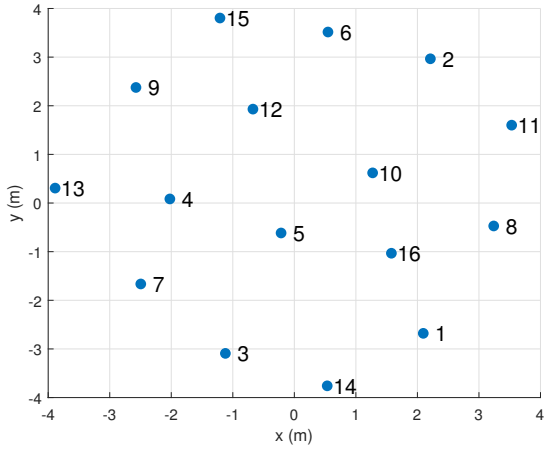

Fig. 4.2 Positions of elements in Pre-AAVS1 array.

4.1 The Antenna Under Test and Acquisition System

The Pre - Aperture Array Verification System (Pre -AAVS1) (see Fig. 4.1) is an antenna array located in Mullard Observatory in Cambridge (UK). It is composed of 16 active dual-polarized log-periodic elements arranged in a pseudorandom (aperiodic) configuration (see Fig. 4.2). Each element, called SKALA-2 [63], is equipped with a Low Noise Amplifier (LNA) integrated on the top of the antenna. The array has a size of 9.2 m and is placed over a ground plane of 16-m diameter. One polarization is along South-North (y-axis) direction whereas the orthogonal polarization (x-axis)

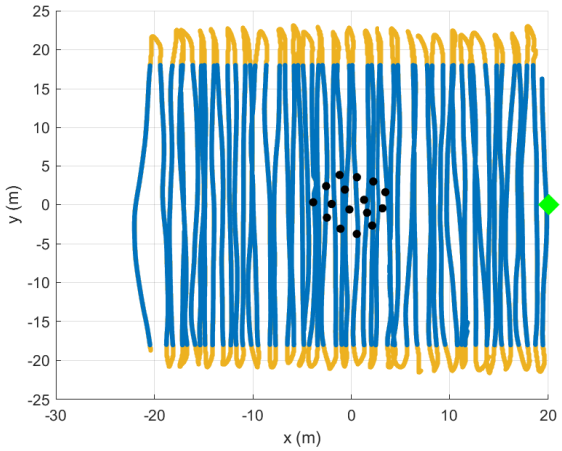

Fig. 4.3 Yellow and blue line represent the UAV path for the y-oriented raster #1 (view from above). Black and green dots represent the array and reference antenna, respectively.

is in the West-East direction. In order to test the presented procedure, the y-polarized elements of Pre-AAVS1 have been selected as AUT. In this receiving system, the two polarizations of each antenna are connected to the analog inputs of a Tile Processing Module 1.2 (TPM) [42], [64], [65], the precursor to the TPM that is used for Phase One of the SKA. The TPM houses 32 Analog to Digital Converters (ADCs), with a programmable amplifier connected to each, and two Field Programmable Gate Arrays (FPGAs). The voltage signals are sampled with an observable band of 400 MHz. The digitized and amplified signals pass through a polyphase filter bank which splits the band into 512 frequency channels resulting in a channel bandwidth of 400 MHz / 512 = 781.25 kHz. The time-step between two successive samples is hence $\Delta t_0 = 1/(781.25\text{ kHz}) = 1.28 \times 10^{-6} s$. Then, by digital filtering, an oversampling factor of 32/27 is applied. In order to reduce the large amount of data, data have been averaged over 1024 samples. The final time-step Δt between two successive samples is then $\Delta t = \Delta t_0 \times 1024 \times 27/32 = 0.0011 s$. In this receving system a digital beamformer is present. However, all the digitized signals have been exploited in this work to achieve more flexibility.

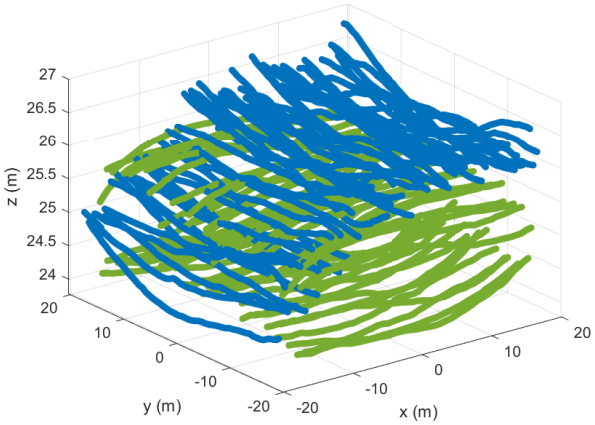

Fig. 4.4 The extracted path for the two UAV flights: y-oriented raster #2 (blue line) and x-oriented raster (green line). Picture from [34].

4.2 Near-Field Planar Scanner

Planar NF scanning is a well-established technique for antenna characterization [66]. The probe usually scans a rectangular grid with constant spacing (usually half wavelength) on a plane. Other planar acquisitions are also possible, e.g., spiral [67] or planar with non constant spacing [68]. The measurement is usually combined with a NF-FF transformation in order to obtain the AUT pattern.
In standard planar NF scanner, several requirements have to be fulfilled in order to apply the NF-FF transformation properly:

- the probe pattern must have no nulls in the AUT direction.
- the probe has to be distant enough from the AUT, so that the mutual coupling between them is negligible.
- the probe has to cover a sufficiently large area in order to have a negligible AUT field outside of that area.
- contrary to spherical scans, probe correction is generally significant and has to be applied.

First two points are trivially fulfilled by the measurement configuration. Last two points are addressed in Section 4.4.2.

The core of the proposed strategy is an Unmanned Aerial Vehicle (UAV) (Fig. 4.1) equipped with a continuous-wave RF source. Through a preprogrammed flight path, the UAV is capable to perform autonomous navigation. Quasi-planar flights (Fig. 4.3-4.4) were performed by the UAV acting as a NF scanner. More precisely, the micro hexacopter was equipped with a continuous-wave synthesizer, a balun and a dipole antenna. The UAV position was acquired by a differential GNSS system with a few centimeters of accuracy. Such position accuracy can be considered acceptable at the considered frequency of 175 MHz (wavelength 1.7 m). The UAV orientation was measured by the onboard Inertial Measurement Unit with an accuracy of about 2 degrees. Overall, three planar flights were performed, labeled by: x-oriented raster, y-oriented raster #1 and y-oriented raster #2. For the sake of redundancy, two flights were performed as a cartesian raster along the y-axis (y-oriented raster #1-2) (these two flights are almost equivalent for the present analysis). The UAV path of the y-oriented raster #1 is shown in Fig. 4.3 as a 2D view whereas x-oriented raster and y-oriented raster #2 are shown together in Fig. 4.4 in a 3D fashion. In each one of these two quasi-planar scans a square area of approximately 40 m x 40 m was covered. From each flight, a scan of 36 m x 36 m has been extracted as input for the NF-FF transformation. This is because measurement points where the UAV curved (yellow points in Fig. 4.3) are source of uncertainty due to the rapidly changing UAV angles (UAV angles are not properly sampled in these regions). For this reason, these points were discarded and rectilinear paths only (e.g., blue points in Fig. 4.3) were considered as input of the NF-FF transformation. During each flight, complex voltages were acquired at each array element by a complete digital back-end (already described in section 4.1). With a maximum speed of 3 m/s, the UAV flight time was about 15 minutes (without landing and takeoff) for each flight. The mean altitude of the UAV flight was approximately 24 meters. Hence, the NF region of the array under test was scanned. Flights were programmed as constant altitude rasters with a constant spacing of half wavelength (0.9 meters) between the parallel linear cuts. However, because the irregularity of the scan the half wavelength sampling criterion was not fulfilled in all the scanning regions (orthogonally to the UAV path direction, e.g., along x-axis for y-oriented raster #1, see Fig. 4.3). On the other hand, the field is heavily oversampled along the UAV path thanks to the very fast receiving acquisition system on the ground. In order to assess the validity of the acquired set of measurement points, a NF-FF transformation has been applied with simulated data on y-oriented raster #1 measurement points (blue path in Fig. 4.3) obtaining good

results. This demonstrates that the non-compliance of the half wavelength criterion in few regions of the NF scan could be neglected in a first approximation. During each flight, the dipole over the UAV was almost tangential to the UAV path e.g., in the x-oriented raster the dipole was almost aligned with the x-axis whereas in the y-oriented raster with the y-axis (see Fig. 4.5). In standard planar NF scans, the two tangential components of the electric field are acquired. Note that these two components are usually measured over the same spatial points. On the contrary, in the present measurement setup, the two components were acquired over two different sets of points (see Fig. 4.4). It is evident that such points follow surfaces that are not planar and not regular either. For this reason, standard NF-FF transformations are hardly applicable. Here, an inverse source technique (see Section 4.4) capable to efficiently deal with a set of measurement points with arbitrary locations has been adopted.

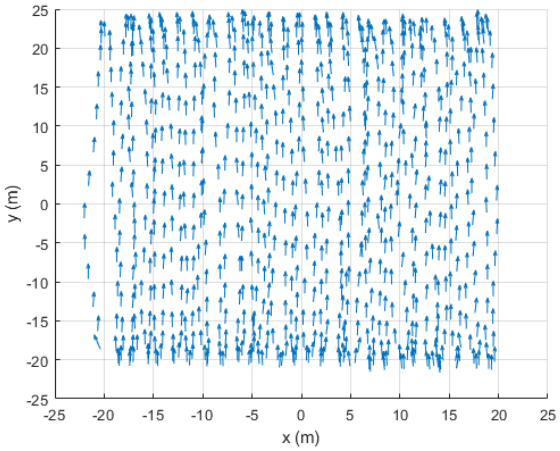

Fig. 4.5 Direction of the UAV-mounted dipole for the y-oriented raster #1.

4.3 Measured Near-Field Data

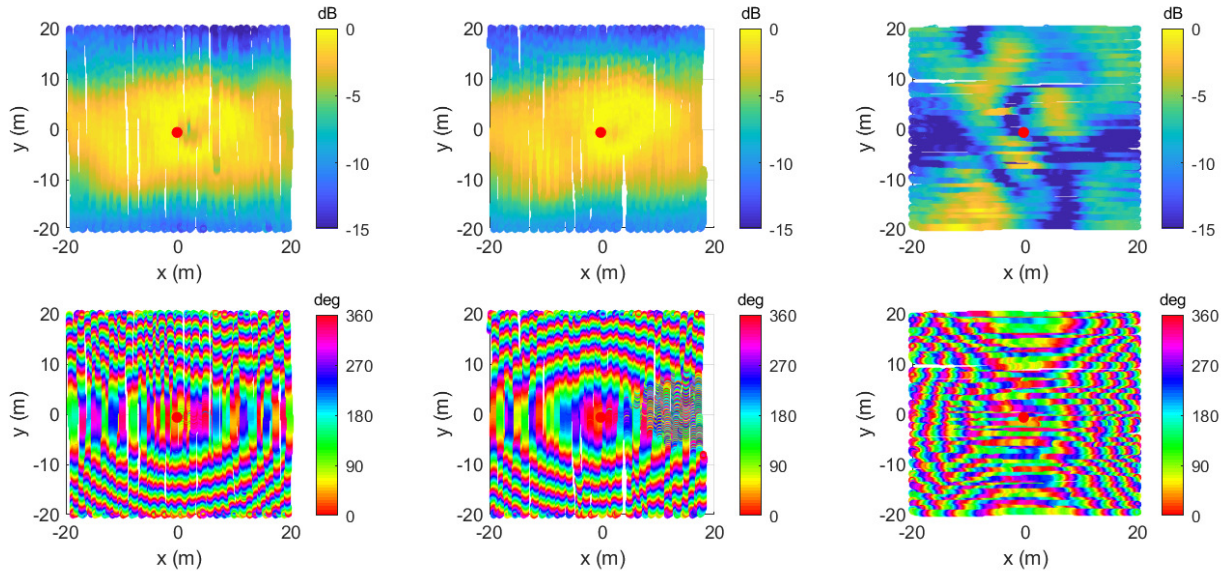

Fig. 4.6 Element 5. On columns (from left to right): y-oriented raster #1 - #2, x-oriented raster. On rows: magnitude and reconstructed phase of the received signal.

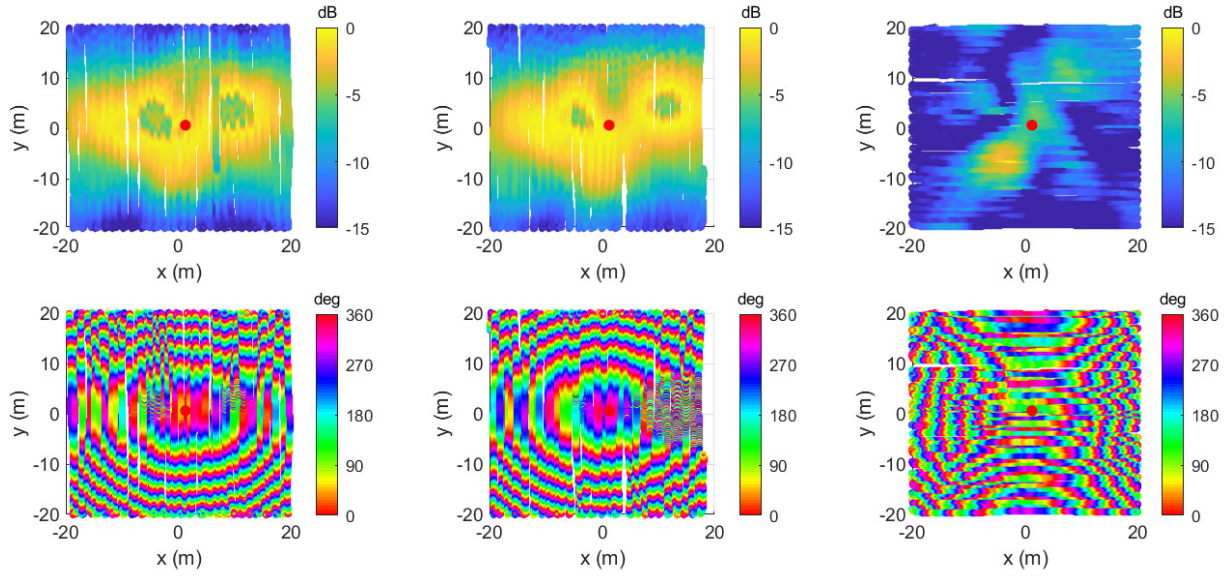

Fig. 4.7 Element 10. On columns (from left to right): y-oriented raster #1 - #2, x-oriented raster. On rows: magnitude and reconstructed phase of the received signal.

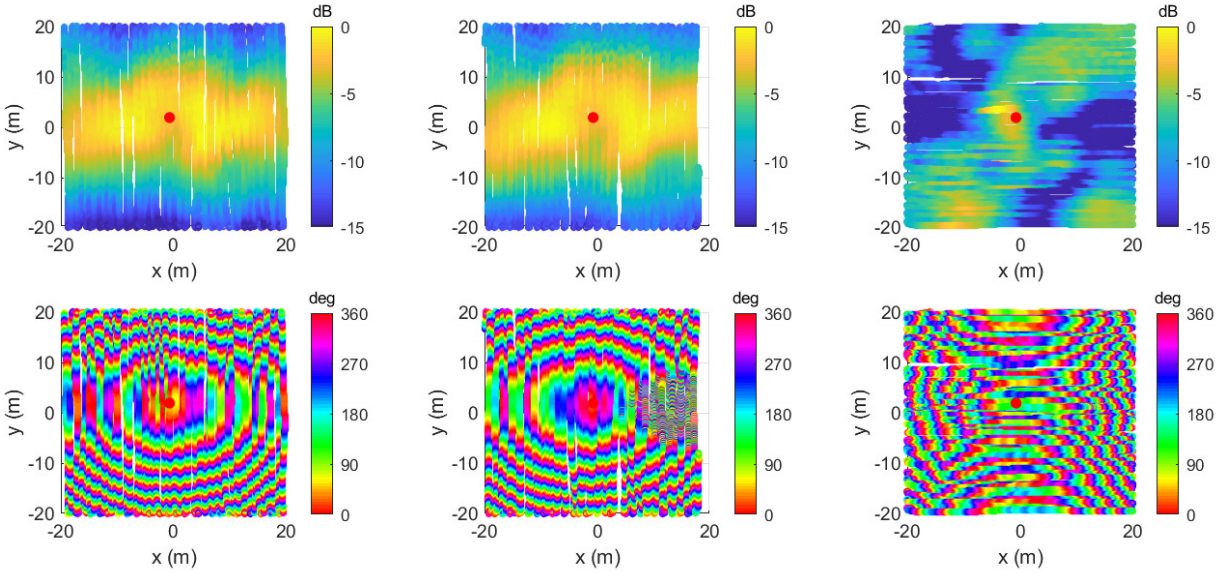

Fig. 4.8 Element 12. On columns (from left to right): y-oriented raster #1 - #2, x-oriented raster. On rows: magnitude and reconstructed phase of the received signal.

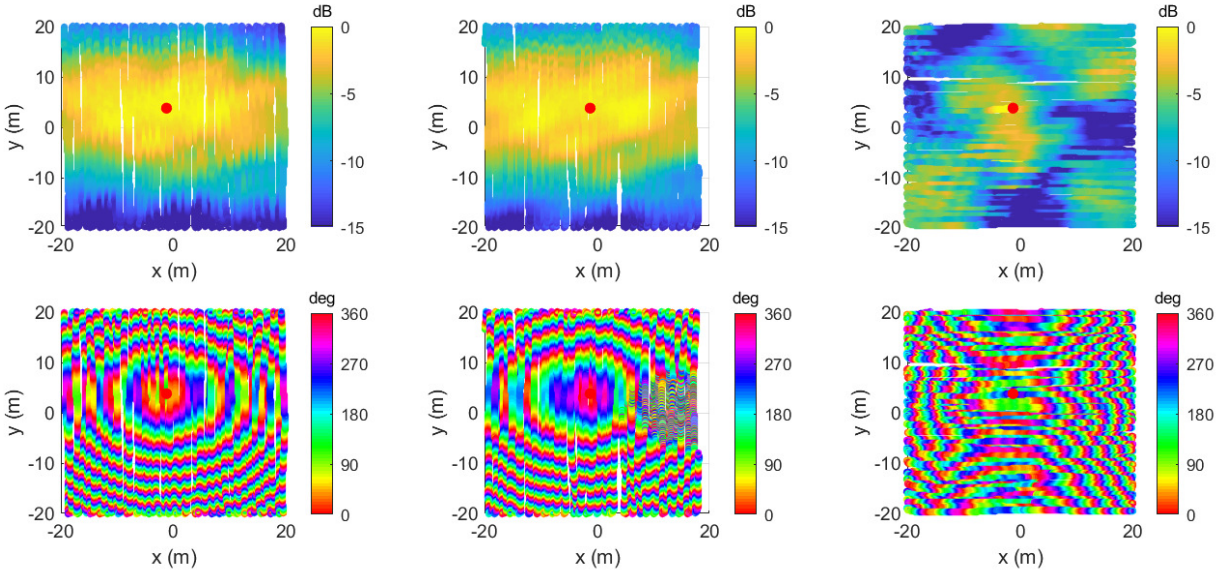

Fig. 4.9 Element 15. On columns (from left to right): y-oriented raster #1 - #2, x-oriented raster. On rows: magnitude and reconstructed phase of the received signal.

In this section, measured NF data of four array elements are presented. These elements (numbered with 5, 10, 12, 15) are located from the origin to the array

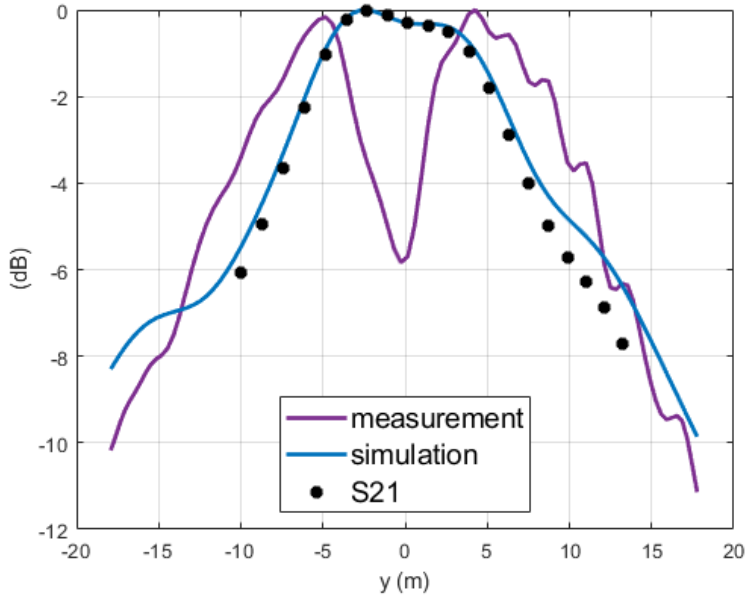

Fig. 4.10 Measured (purple) and simulated (blue) power at element 5 in dB for y-oriented raster # 1, cut at $x = 2.1$ m. Black dots represent the scattering parameter $|S_{21}|^2$ (dB) between UAV and AUT. Each curve is normalized at its maximum.

boundary (see Fig. 4.2).

All measured data suffered from non-linearity at RF level and truncation phenomena at digital level. In fact, a better quality can be appreciated in signals which exhibits a lower power level. Furthermore, these artifacts are usually present where the AUT (simulated) field is particularly strong (as it will be shown in Table 4.1)[1]. As it will be shown in this Section, such issues are appreciable for element 5 and reference antenna and particularly relevant for element 10. On the contrary, signals of elements 12 and 15 appear to be more reliable. Further optimization of the acquisition system setup will probably lead to smaller overall discrepancies.

Figures 4.6, 4.7, 4.8, 4.9 (first row) show the measured NF power at 175 MHz along the UAV path (in a 2D view) received by the four selected elements, respectively. For the y-oriented rasters (first two columns), each measured NF pattern resembles a low-directivity radiating element whose position is highlighted with the red dot. As previously mentioned, signals of elements 5 and 10 are corrupted in some regions of the UAV scan (as it will be shown in this Section, the same regions of distorsion

[1] A complete debug and understanding of such issues at the receiver level is out of focus of this thesis.

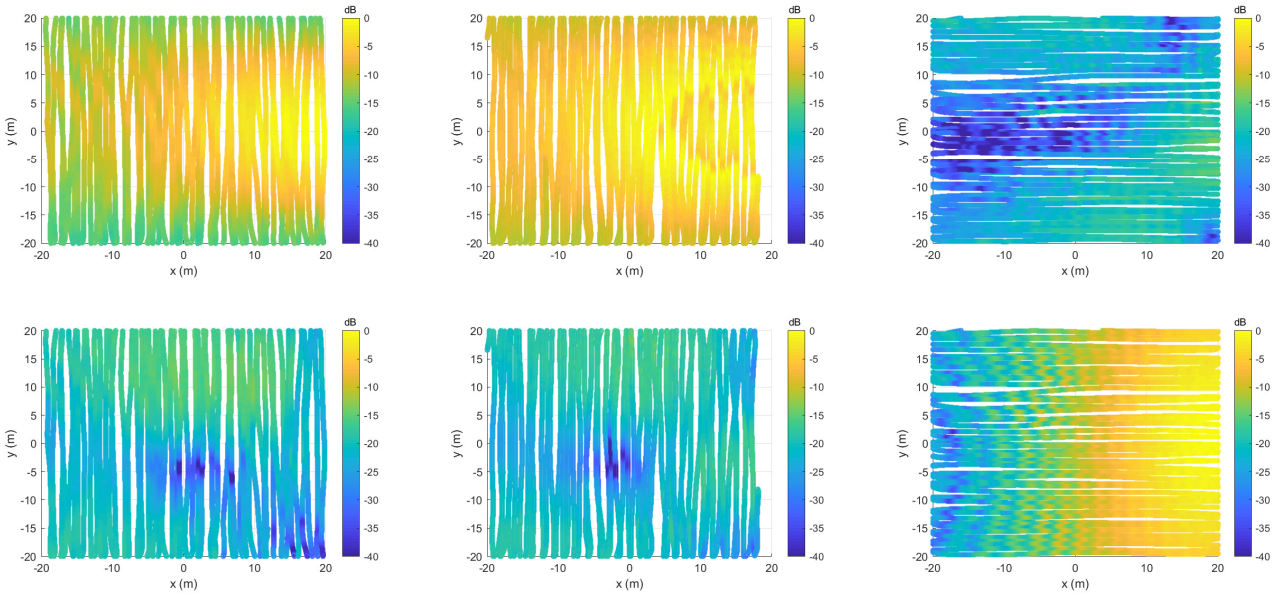

Fig. 4.11 Magnitude of the signal received at the reference antenna. On columns (from left to right): y-oriented raster #1, y-oriented raster #2, x-oriented raster. On rows: y-polarized and x-polarized reference antenna, respectively. Each flight (i.e., column) is equalized at the global maximum of the two polarizations.

appear in the phase plots). In a first attempt, this distortion was attributed to an interaction between UAV and array. This hypothesis has been rejected after a simulation of the scattering parameter S_{21} between element 5 and UAV (including array and grounplane) (see Fig. 4.10) along a cut where the measured signal is corrupted.

It should be noted that, in some regions near the boundary of the scanned area, the measured power is only 5 dB lower than the maximum. As it will be stated in section 4.4.2, this is not enough considering that a level of -30 dB from the maximum is generally required along the boundary of the scan plane [69]. Such limited NF scan size was dictated by the UAV flight duration.

Received power at reference antenna is shown for all flights in Fig. 4.11. For the y-oriented raster #2 (second column, first row), the signal is a little distorted in the region near the reference antenna position. As it will be shown in Section 4.4.1, this affects negatively the phase reconstruction (of all array elements) for y-oriented raster #2, in the region near the reference antenna position. It should be noted that

the y-oriented raster for the y-polarized reference antenna is not symmetric with respect to the x-oriented raster of the x-polarized reference antenna. This is because the dipole-like reference antenna pattern is more directive in its E-plane with respect to its H-plane.

The phase information has been retrieved according to the procedure described in Chapter 2 through the dual-polarized reference antenna (see (2.23) and (2.24)). The phase equalization constant $\angle C_{ref,y} - \angle C_{ref,x}$ between the two orthogonal reference antenna polarizations computed through (2.22) is approximately 70°. Reconstructed phases of the four selected elements are shown in Fig. 4.6, 4.7, 4.8, 4.9 (second row). For y-oriented rasters (first two columns) the element phase diagrams are consistent with the characteristic phase pattern of a spherical wave centered at the element position.

For the sake of comparison, measured powers and reconstructed phases of the four considered elements are reported with their simulated counterparts in tables 4.1 and 4.2. For all simulated quantities, the electric field component along the UAV-mounted dipole direction has been computed from a complete NF simulation in FEKO. It should be noted that, for elements 5 and 10, regions of distortion for the measured signals (left column) correspond approximately to regions where the simulated field is strong (right column). This may confirm the previously mentioned issues in the acquisition system (e.g., packet loss phenomena).

As a further verification, the reconstructed phase is compared to the simulated one along a quasi-rectilinear cut at x = 1.5 m for the y-oriented raster. Very good agreement can be observed between the blue markers (simulation) and purple solid line (reconstructed) in Fig. 4.12.

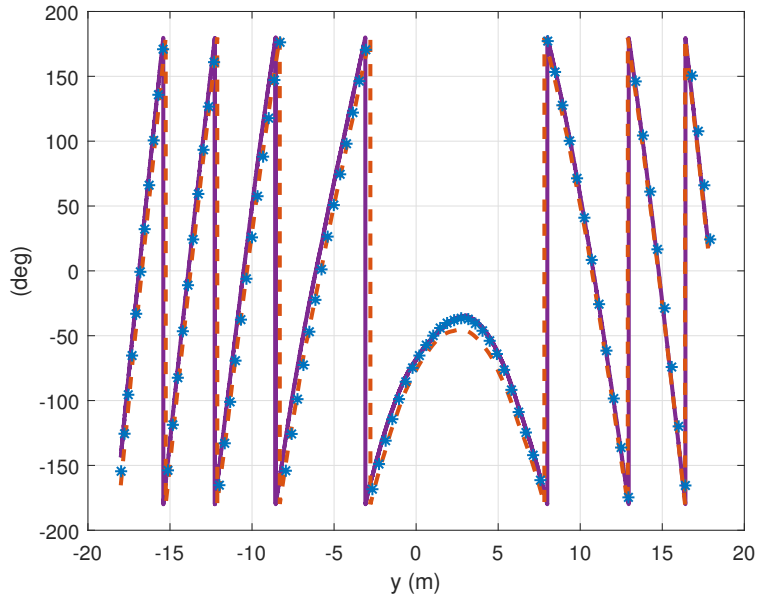

Fig. 4.12 Reconstructed phase (deg) (purple solid line), FEKO simulation (dotted blue markers) and phase of the NF field radiated by inverse source currents (dashed orange) along a quasi-linear cut at x=1.5 m (y-oriented raster) for element 12. Picture from [34].

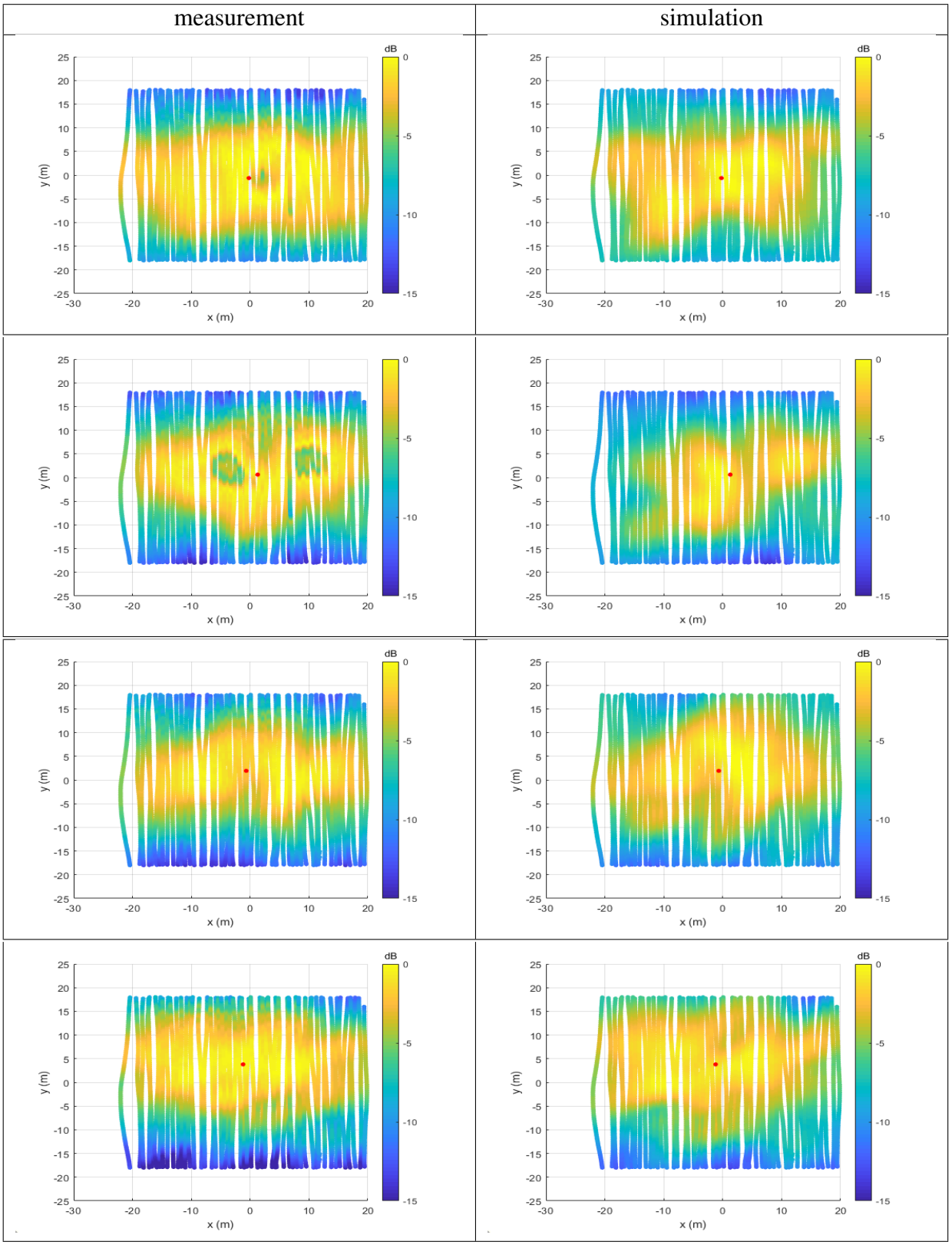

Table 4.1 Measured (left column) and simulated (right column) magnitude of the received signal at elements 5, 10, 12, 15 for y-oriented raster #1.

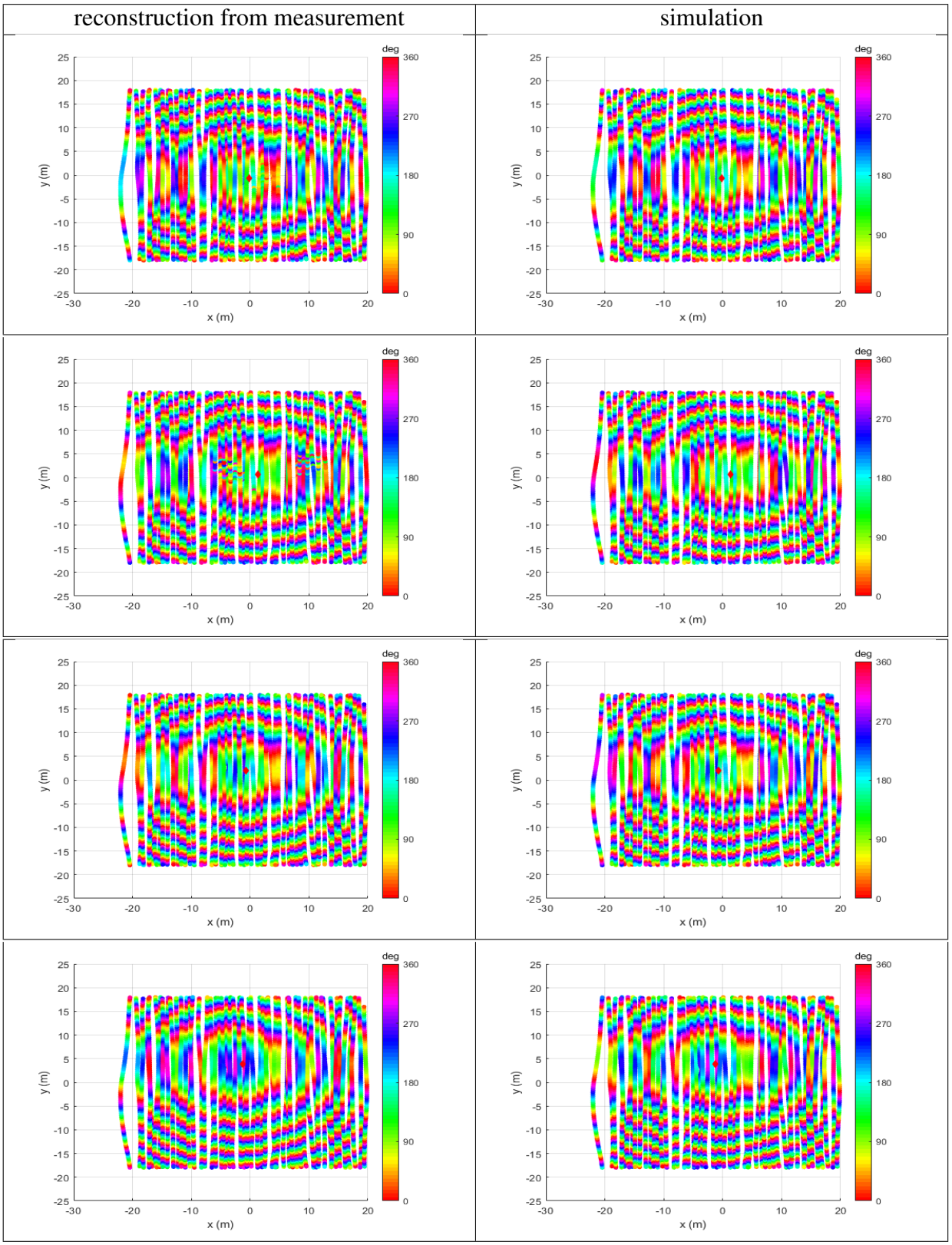

Table 4.2 Reconstructed (left column) and simulated (right column) phase of the received signal at elements 5, 10, 12, 15 for y-oriented raster #1.

4.4 Results

In this Section, data on the NF-FF transformation are presented. The presented results have been achieved using two UAV flights, i.e., the x-oriented raster and y-oriented raster #2 as input for the NF-FF transformation. Similar results have been obtained using the x-oriented raster and y-oriented raster #1.

4.4.1 Inverse Source and Near-Field Results

The UAV path (see Fig. 4.3, 4.4) is not regular (neither planar nor uniformly spaced) and thus standard NF-FF transformations cannot be applied. For this reason, an inverse source[2] approach [75] has been adopted as NF-FF transformation method This approach is based on equivalent electric and magnetic currents placed over a virtual (non-physical) surface surrounding the AUT. These unknown currents are computed enforcing a null radiated field inside the virtual surface and a field equal to the measured one on the UAV measurement points (e.g., for element 15 second and third column of Fig. 4.9). Through this choice, Love's currents (null field inside the virtual surface) are exploited. In this way, the computed currents are directly related to the actual electromagnetic field radiated by the AUT. The complexity of the operator that has to be inverted is increased by the addition of the null field condition. However, this choice drastically improves the condition number of the operator, resulting also in a more stable solution. Different configurations of the inverse source can be also considered [76], [77]. It should be noted that reciprocity is exploited (see Appendix B) since the AUT is actually in receive mode. It should be noted that differently from other applications of inverse source [75] the measurement points belong to two different rasters, one for each polarization (see Fig. 4.4). A vertical cylinder of 5 m radius and 3.5 m height has been used as virtual surface (the array presented in Section 4.1 has 4.6-m radius). The presence of the ground-plane has been taken into account into the inverse-source process. The surface of the cylinder has been discretized with approximately 36.000 RWGs [78] for a total number of 72.000 unknowns for the electric and magnetic currents. The total number of measurement points was 900.000, considering both x and y-oriented rasters. The

[2]Other NF-FF transformation approaches based on plane-wave expansions [70], [71] or single-cut NF-FF transformations [72], [73] or non-redundant representations [74] have been also proposed in literature.

linear system arising from the discretization has been solved in a least squares sense using an iterative method coupled with a memory saving matrix factorization and a fast matrix-vector multiplication [79], [80]. In this way, for each array element, the computation of the currents took approximately 16 GB of the Random Access Memory (RAM) and 32 minutes (27 for the matrix factorization and 5 minutes for the linear system solution) on a workstation with a processor Intel Xeon E5-2697 v2. Electric equivalent currents are shown in Fig. 4.13, 4.14 for element 12 and 15,

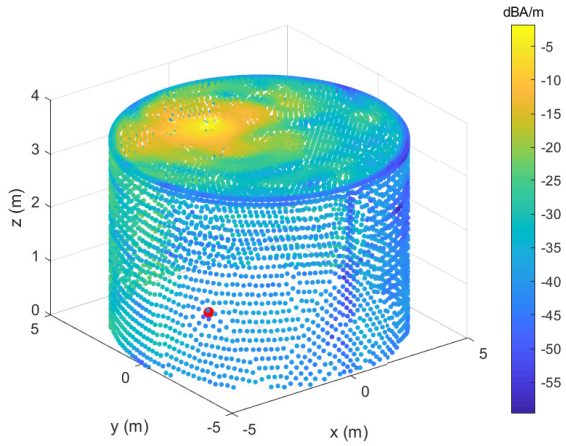

Fig. 4.13 Magnitude of the electric equivalent current for element 12. Picture from [34].

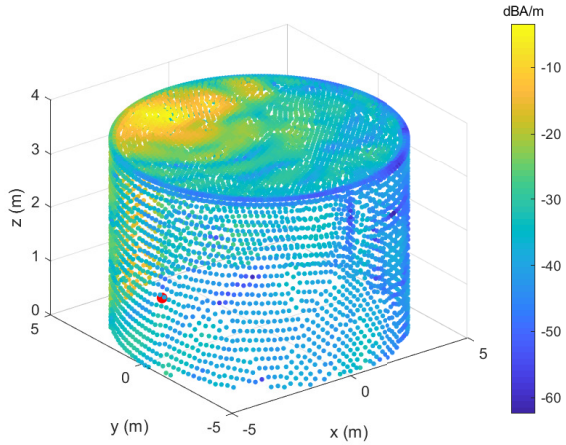

Fig. 4.14 Magnitude of the electric equivalent current for element 15. Picture from [34].

respectively. The red dot marks the position of the considered antenna on the ground.

Although currents are mainly concentrated on the upper part of the cylinder, they are non-vanishing also on its lateral part because of the finite dimension of the cylinder. Magnetic equivalent currents are not shown due to their similarity to electric ones. As a verification example, the phase of the NF radiated from the computed equivalent currents (along a cut at x = 1.5 m for the y-oriented raster) is also reported in Fig. 4.12 with the orange dashed line. A good agreement can be observed between these curves, with a maximum discrepancy of approximately 10 degrees. For a comparison over the whole UAV path, magnitude and phase of the field radiated by the inverse source currents are reported on the right column in Fig. 4.15 and 4.16, respectively. On the left column, the input quantities used for the NF-FF transformation (i.e., the measured magnitude and the reconstructed phase) are reported. It can be observed that the field strength of inverse source currents is very low where the reconstructed phase is corrupted (see first row, first column of Fig. 4.16, right part of the UAV scan). As it will be shown in Section 4.4.2 and 4.4.3, a similar phenomenon can be appreciated in the H-plane of the NF-FF transformed EEPs.
For the x-oriented raster (Fig. 4.15, second row), a good agreement between measured and radiated by inverse source currents field can be observed.

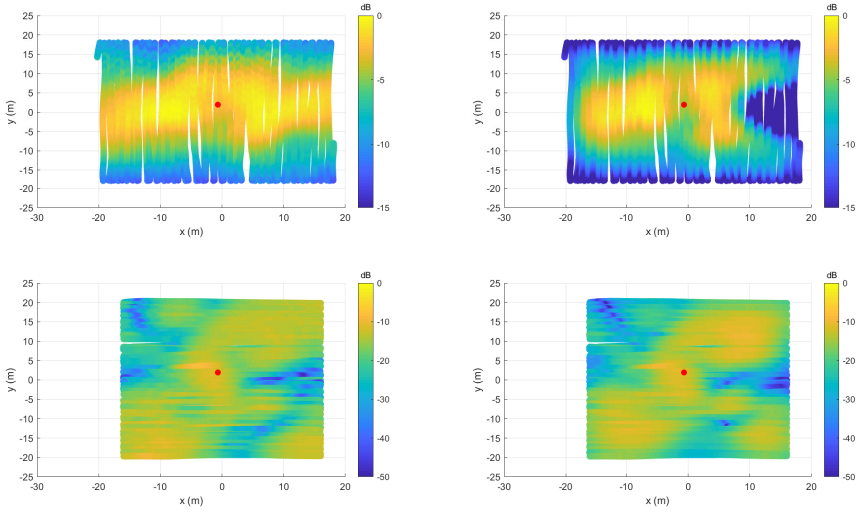

Fig. 4.15 Left column: measured magnitude of the signal at element 12 (used as input for the inverse source NF-FF transformation). Right column: magnitude of the field radiated by inverse source currents. First row: y-oriented raster #2, second row: x-oriented raster.

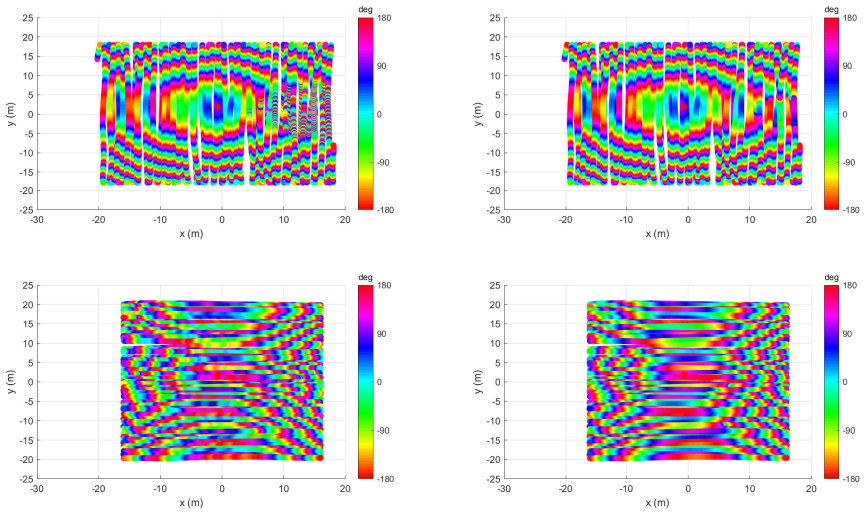

Fig. 4.16 Left column: reconstructed phase of the signal at element 12 (used as input for the inverse source NF-FF transformation). Right column: phase of the field radiated by inverse source currents. First row: y-oriented raster #2, second row: x-oriented raster.

4.4.2 Embedded Element Patterns (EEPs)

The radiated FF patterns at 175 MHz are computed from the equivalent currents over the cylindrical surface. NF-FF transformations exploiting larger cylinders (with radius r = 8 m and r = 10 m) were also performed. Tables 4.3 and 4.4 show the transformed FF EEPs (magnitude and phase of the co-polar component) on their E-plane and H-plane, respectively. All curves are equalized at zenith. The three NF-FF transformations considering cylinders of radius r = 5, 8 and 10 m as virtual surface are reported with solid, dotted and dashed orange lines for elements 5, 10, 12, 15.

For the sake of comparison, a FF flight was performed due to the feasible Fraunhofer distance. Magnitude and phase of the FF EEPs have been extracted from this measurement as in [33], [58] (i.e., the phase has been extracted from (2.16) whereas the magnitude from (3.1)). Hereinafter, they are referred to as the "measured FF EEPs" and are reported with purple lines in tables 4.3 and 4.4. In particular, the reference antenna has been used also in this FF case for the computation of each EEP measured phase.

As further verification, a FF simulation has been performed in FEKO and is also

reported in tables 4.3 and 4.4 with a blue line.
It is well known that NF planar scans suffer from some limitations. First, the transformed FF pattern of the AUT is valid only over a limited angular range. The angular bound for the validity of such transformed EEPs depends on the aperture of the AUT and both the scan size and height. Considering the array size of 9.2 m, the angular validity for the transformed FF can be estimated in the order of ± 29° [81]. On the other hand, considering the dimension of the array with its ground plane, i.e., 16 m, the maximum angle of validity reduces to ± 22°. In tables 4.3 and 4.4, solid and dashed vertical black lines represent the validity range of the reconstruction corresponding to 22° and 29°, respectively.
Second, as a standard requirement for NF measurement [69], the signal level at the edges of the planar scan must be 30 (or even 40) dB below the maximum. In this work, the measured power is however only 5 dB from the maximum (see Section 4.3) in some regions along the boundary. This happens because the scan size (36 - 40 m) is not large enough for the considered scan height (about 20 m). These two parameters have been selected considering flight duration and safety (to avoid collision between UAV and top of the AUT). For this reason, an even smaller angular validity (with respect to criteria discussed above) is expected in the EEPs[3].
It should be also mentioned that the (UAV-mounted) source dipole-like pattern has been found almost constant within the angular validity range discussed above. Therefore, probe correction issue has not been addressed in this work. Nevertheless, results are still quite satisfactory.
As a general remark, in table 4.3 the three NF-FF transformed E-plane EEPs (orange curves) show good consistency within the ± 22° angular region, for both elements 12 and 15. In particular, in table 4.3 the agreement between NF-FF transformed and FF measurement magnitude patterns of element 12 is reasonably good[4] (less than 1 dB discrepancy) within the ± 22° angular region. The discrepancy is a little bit higher for element 15 [5]. This is related to the more significant truncation effect (see Fig. 4.9) i.e., the element is closer to the boundary of the scan area. On the contrary, the

[3] In this work, the radiation pattern has been retrieved using the inverse source technique. However, in a classical planar NF-FF transformation, the radiation pattern is computed from the aperture field through a Fourier transform. Truncation of the spatial domain is equivalent to multiply the aperture field to a rectangular function which is equal to one on the measurement domain and zero outside. The desired pattern is hence distorted by a convolution with a sinc function. As a result, oscillations can appear in the reconstruction. This truncation effect is also known as Gibbs phenomenon.

[4] element 12 is located near the array center, see Fig. 4.2

[5] element 15 is located near the array boundary, see Fig. 4.2

corrupted signals of elements 5 and 10 result in a worse agreement between the three NF-FF transformed EEPs. Furthermore, for element 5 and 10 a worse agreement between NF-FF transformed EEPs and FF measurement can be observed.
Results are similar for H-plane EEPs in table 4.4. As mentioned in Section 4.3, all elements suffer from a corrupted phase reconstruction [6] in the UAV scanning region near the reference antenna position. This affects negatively the NF-FF transformed EEPs, in particular in their H-plane.
As far as the phase of E-plane EEPs is concerned, good agreement can be observed in table 4.3 between NF-FF transformations and FF measurement. Although the phase of the FF measurement suffered from some noise in the positive zenith angle region of H-plane EEPs (see 4.4), a good agreement can be observed between NF-FF transformations and FF measurement.
As a figure-of-merit for the E-plane, the root mean square of the logarithmic difference [60] is shown in Fig. 4.17 for all array elements. Such error measures for simulated and NF-FF transformed EEPs are reported with blue and orange dots, respectively. The measured FF EEPs are considered as reference. The considered angular range is ± 22°. Fig. 4.17 suggests that the quality of the E-plane NF-FF transformed EEPs is comparable to the simulation one. Data for element 8 are not available because that receiver channel was connected to the reference antenna. On the contrary, the error value for the NF-FF transformed EEP of element 11 is not reported because the corresponding NF measured signal exhibited lower quality.

[6] because the signal of the reference antenna is corrupted in the region near the reference antenna position, see Fig. 4.11

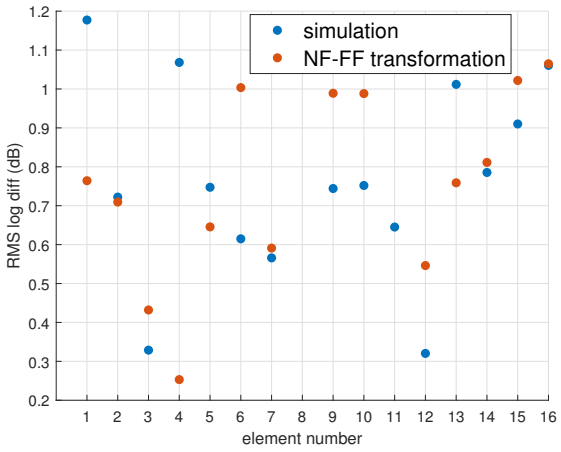

Fig. 4.17 Orange (blue) dots represent the Root Mean Square of the log-difference between FF measurement and NF-FF transformed (simulated) EEPs in the angular range 22° degrees. Picture from [34].

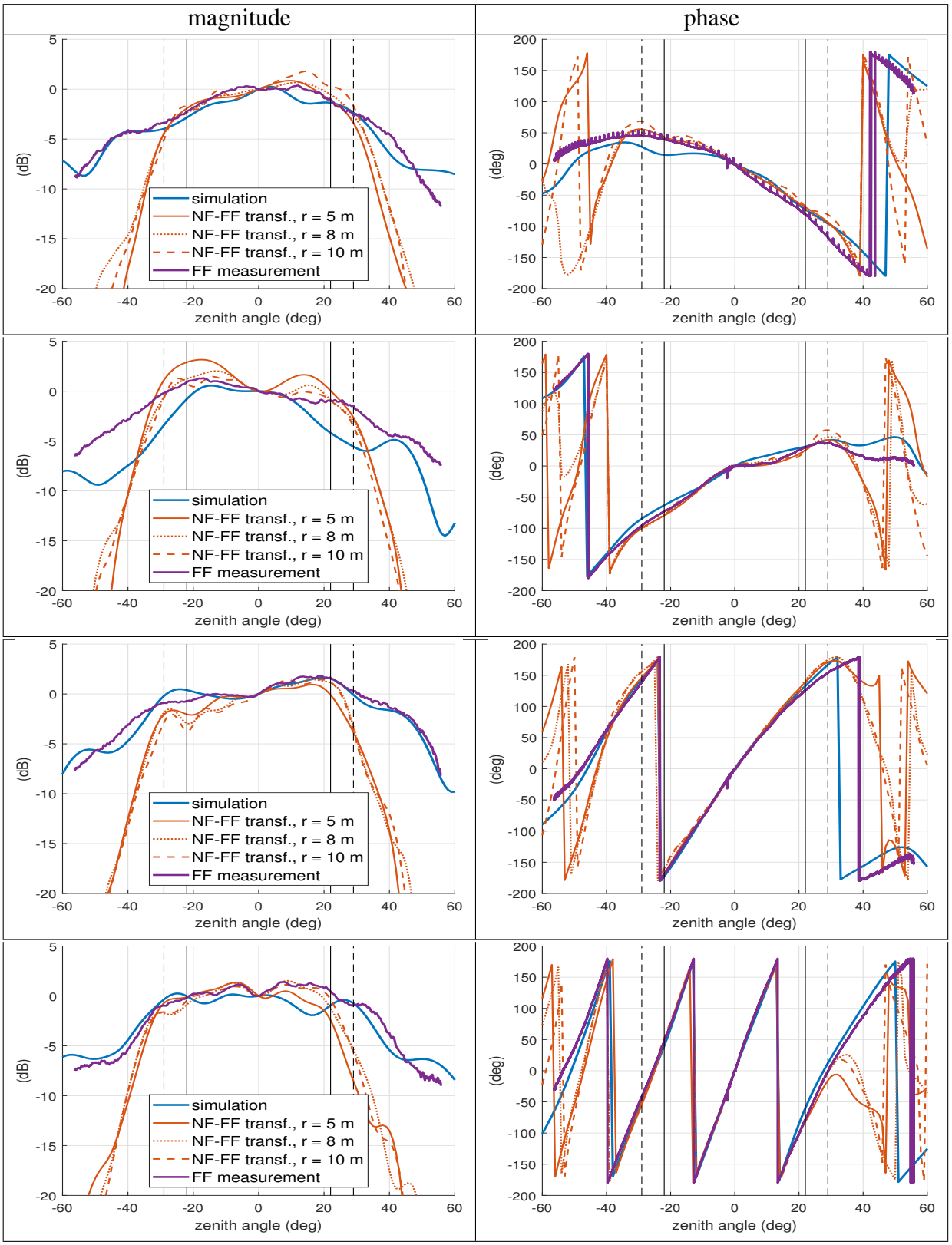

Table 4.3 Magnitude (left column) and phase (right column) of E-plane Embedded Element Patterns (EEPs) of elements 5, 10, 12, 15 for three different NF-FF transformations (r is the radius of the cylinder used as equivalent surface).

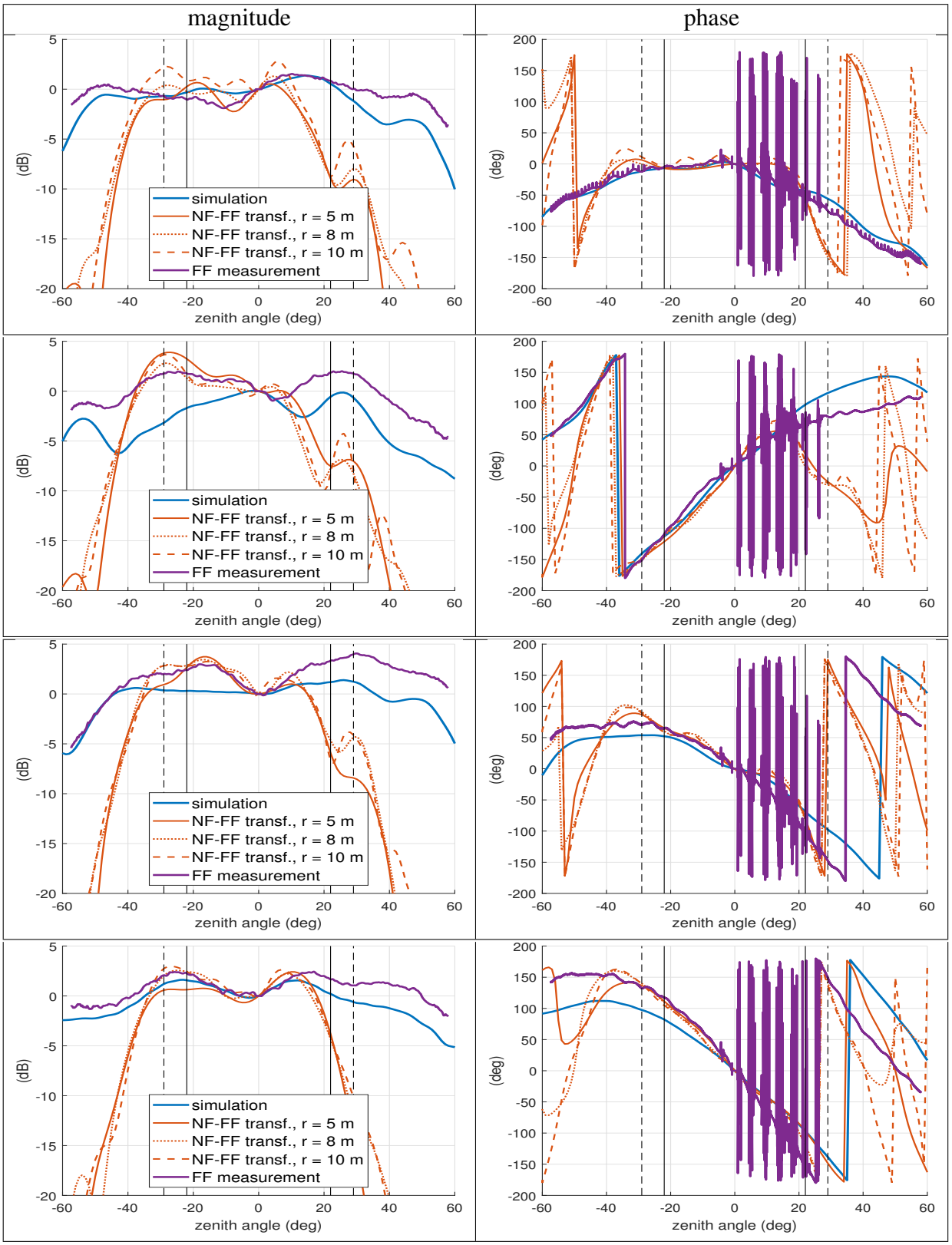

Table 4.4 Magnitude (left column) and phase (right column) of H-plane Embedded Element Patterns (EEPs) of elements 5, 10, 12, 15 for three different NF-FF transformations (r is the radius of the cylinder used as equivalent surface).

4.4.3 Array pattern

Array calibration is a fundamental task for phased array with digital beam-forming. Calibration coefficients need to be accurately determined to focus/steer the array beam in a particular direction. Such coefficients depend on both the antennas and acquisition system. The presented method represents a viable solution to determine calibration coefficients from NF measurements.
As reported in section 4.4.2, all the EEPs have been obtained by NF-FF transformation from NF measurements. The calibration coefficients can be obtained by equalizing all such EEPs (in magnitude and phase) for a particular observation direction. In this way, both antenna and receiver contributions are accounted for.
The sum of all the equalized EEPs produce the full array beam. Fig. 4.18 shows the co-polar component of the E-plane beam pattern for the array under test pointed at zenith. Simulated and measured FF EEPs are reported with blue and purple lines, respectively. The NF-FF transformation describes the main lobe and first nulls quite well. Fig. 4.19 shows the co-polar component of the H-plane. The NF-FF transformed pattern has a null in the positive zenith angle region. This can be explained by the corrupted phase signal of the reference antenna (described in Section 4.3). In fact, the direction where the NF signal is distorted corresponds in FF to positive zenith angle values of the H-plane.
The E-plane cross-polar component is shown in Fig. 4.20. The result represented with orange solid line has been obtained with both x and y-oriented rasters in Fig. 4.4 whereas the orange dashed line only uses the y-oriented raster. The lack of the x-component information in the latter is clearly visible in Fig. 4.20. The simulated cross-polar pattern is reported with blue line (measured cross-polar FF data are not available). Even if sampling both NF components doubles the UAV flight time, this is necessary to achieve an acceptable accuracy for the cross-polar component. The good agreement between simulation (blue line) and NF-FF transformation (solid orange line) confirms the validity of the sampling approach based on two different rasters (see Fig. 4.4), one for each polarization. For a complete comparison over the full azimuthal angle, Fig. 4.21, 4.22 show the magnitude (i.e., $|e_\theta|^2 + |e_\phi|^2$) of the NF-FF transformed and simulated 2D FF array patterns pointing at zenith. Quantities θ and ϕ correspond to the zenith and azimuth angles of the spherical coordinate system, respectively. Solid and dashed black circles correspond to 22° and 29°, respectively. As reported in Section 4.4.2, these angle values denote the

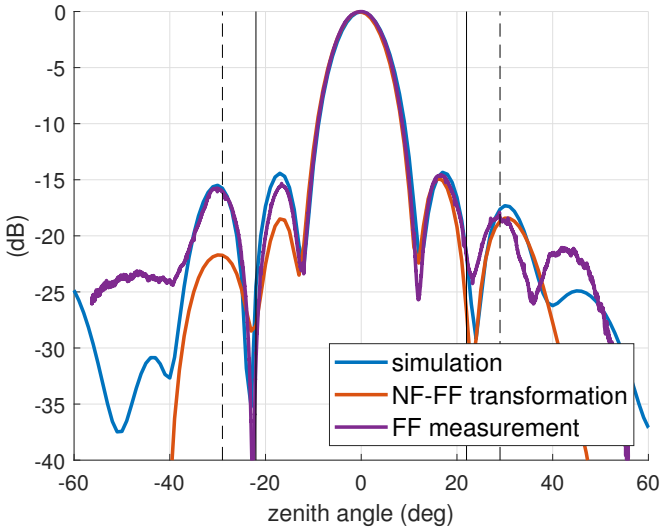

Fig. 4.18 Array beam magnitude, E-plane cut, co-polar component. Blue, orange and purple curves represent the far-field from simulation, NF-FF transformation and FF measurement, respectively. Picture from [34].

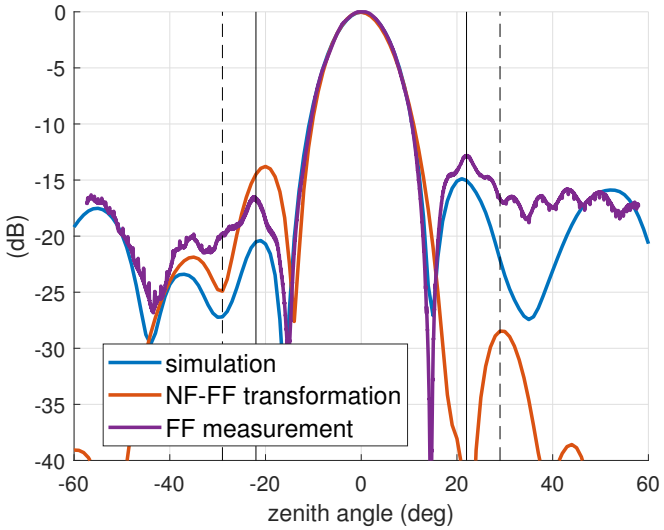

Fig. 4.19 Array beam magnitude, H-plane cut, co-polar component. Blue, orange and purple curves represent the far-field from simulation, NF-FF transformation and FF measurement, respectively.

validity of the NF-FF transformation across the zenith angular range. The agreement between the 2D patterns is quite satisfactory, i.e., main lobe size and first sidelobe

locations and levels are in agreement. The 2D FF measured pattern is not available due to its prohibitive time duration (only a few FF cuts can be scanned by the UAV in a single flight [33]).

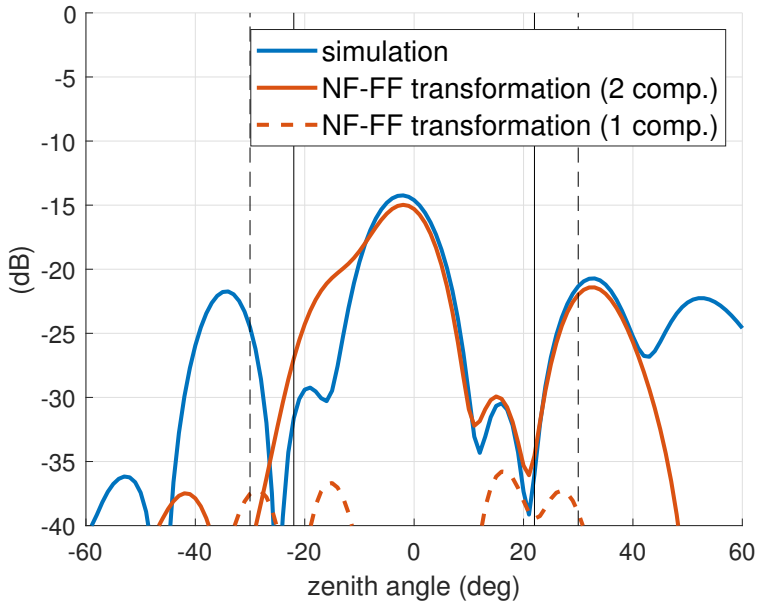

Fig. 4.20 Array beam magnitude, E-plane cut, cx component. Blue, solid orange and dashed orange curves represent the far field from simulation and NF-FF transformation (two electric field components as input) and NF-FF transformation (only one electric field component as input), respectively. Picture from [34].

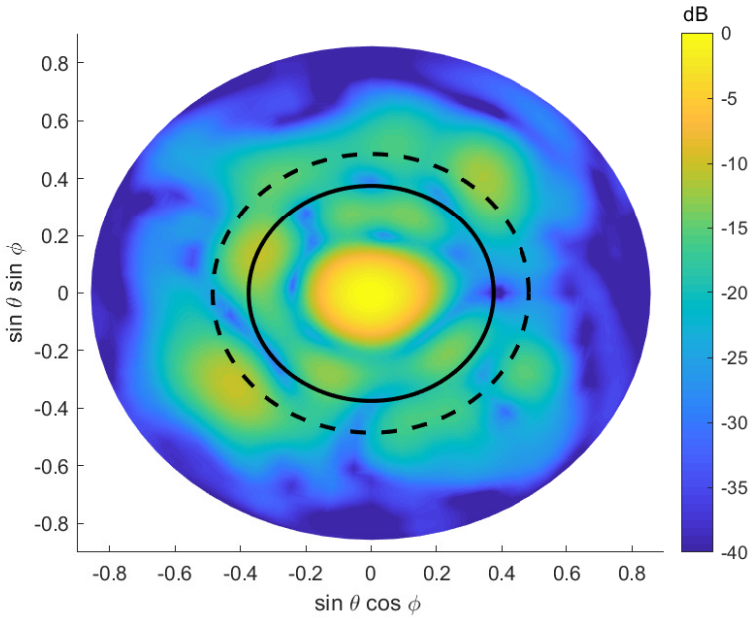

Fig. 4.21 NF-FF transformed array beam magnitude (2D view). The black circles show the angular validity range of the NF-FF transformation (see Section 4.4.2). Picture from [34].

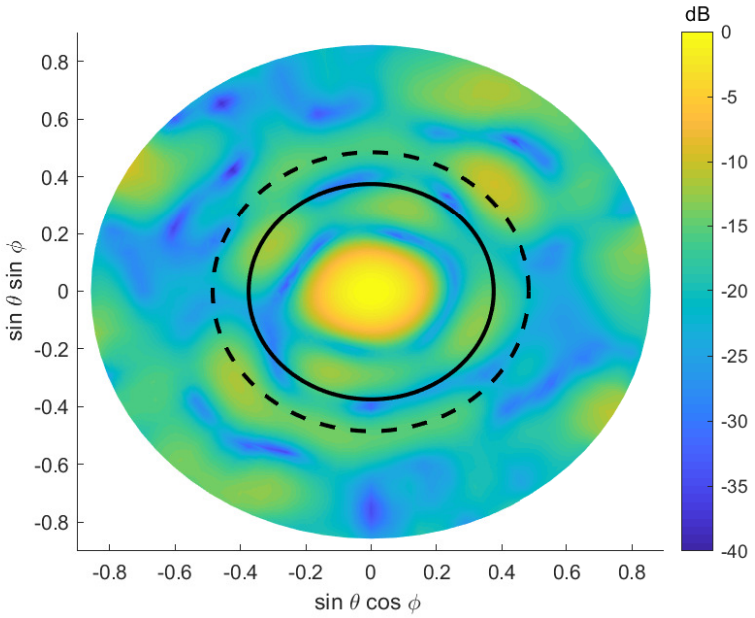

Fig. 4.22 Simulated array beam magnitude (2D view). The black circles show the angular validity range of the NF-FF transformation (see Section 4.4.2). Picture from [34].

4.5 FF vs NF flights

In this Section, FF and NF flights are compared in terms of time duration. This comparison is motivated by future characterizations of fully deployed (40-m size) SKA stations. As far as FF flights are concerned, azimuthal rasters are considered. These flights consist of several circular concentric paths with constant azimuthal angular step $\Delta\theta$ and constant distance from the AUT (see Fig. 3 in [82]), where $\Delta\theta$ is the azimuthal angle between two successive concentric paths. If N circular paths are performed, this flight allows to obtain the FF pattern within the $\theta_{FF} = N\Delta\theta$ angular range with a $\Delta\theta$ resolution. As far as NF flights are concerned, a cartesian raster (e.g., a y-oriented cartesian raster, see Fig. 4.3) with constant step $\Delta y = \lambda/2$ is considered. The size of the cartesian raster is chosen in order to obtain an angular validity θ_{FF} [81] in the NF-FF transformed pattern, i.e., the same θ_{FF} is fixed for both FF and NF flights.

In Fig. 4.23, path lengths of the FF and NF flights are compared considering different values of array sizes. A frequency of 350 MHz and a validity angle of $\theta_{FF} = 60$ degrees are chosen. For the FF flights, two different values of $\Delta\theta = 5$, 10 degrees are considered (see blue and orange line, respectively). The altitude of the FF flights is chosen as the minimum FF distance, i.e., $\max\{10\lambda, 2D^2/\lambda\}$. For the NF flight, an altitude of 20 meters is fixed.

Assuming a constant UAV speed of 3 m / s, the time needed for the FF and NF flights is shown in Fig. 4.24. As Fig. 4.23 and 4.24 show, FF flights becomes dramatically time-consuming for big apertures. On the contrary, NF flights are faster to perform. Moreover, NF flights are much more feasible, i.e., the UAV can fly at low altitude. It should be also mentioned that the resolution $\Delta\theta$ of the NF-FF transformed pattern can be arbitrary small, i.e., radiation integrals of the inverse source currents can be evaluated over arbitrary sets of angles (e.g., $\Delta\theta = 0.1$ degrees can be chosen).

In conclusion, UAV-based NF measurements can represent a valuable alternative with respect to FF measurements to test fully deployed (40-m size) SKA stations.

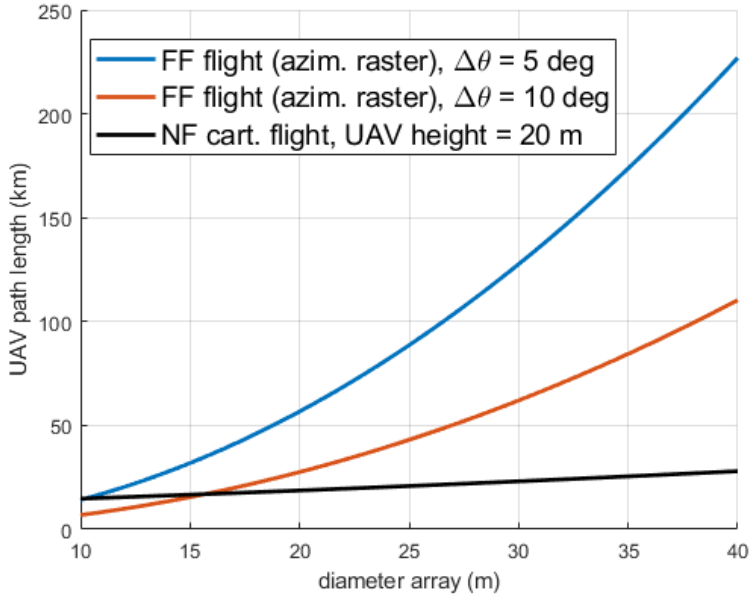

Fig. 4.23 Path length (kilometres) of UAV flights in case of FF (blue and orange lines) and NF (black line) measurements. Different array sizes are considered on the x - axis.

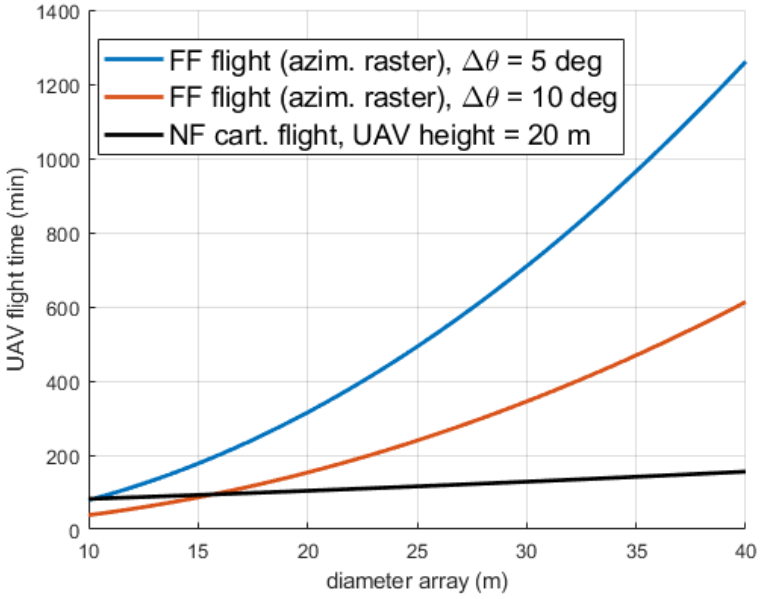

Fig. 4.24 Time duration (minutes) of UAV flights in case of FF (blue and orange lines) and NF (black line) measurements. Different array sizes are considered on the x - axis.

Chapter 5

Conclusion

The characterization of large antenna arrays is a very challenging task. In recent years, Unmanned Aerial Vehicle (UAV) technology has been widely experimented as antenna testing solution for FF pattern measurements. As far as power measurements are concerned, the main source of error is usually represented by the uncertainty on the UAV orientation and modeling (the UAV position error can usually be neglected in a first approximation because it causes an error that decays with respect to the distance from the AUT). For example, at lower frequencies (e.g., 50MHz) the UAV-mounted source usually shows a low-directivity dipole-like pattern. In this case, the UAV orientation error affects mainly the expected source polarization whereas the gain remains approximately constant. For this reason, UAV-based measurements of the AUT cross-polarization still remains a challenging task. Furthermore, as far as the UAV modeling is concerned, the UAV usually mounts a mismatched load at lower frequencies. Therefore, a precise evaluation of the reflection coefficient at source level (and hence the power delivered to the transmitting antenna) can be not trivial. On the other hand, at higher frequencies, the UAV usually mounts a more directive antenna with the UAV structure acting as a ground plane. In this case, the UAV orientation error significantly affects the expected source gain as well as polarization.

However, when the AUT is very large, the FF distance (greater than hundreds of meters) is no longer compliant with flight altitude regulations. In this case, NF approaches become necessary and a NF-FF transformation can be used to determine the FF quantities of interest from NF data. Hence, UAV-based NF measurements represent a valuable alternative to FF ones. This is because a complete FF measurement

over a portion of the sphere (not single FF cuts) is dramatically time-consuming for big apertures. Furthermore, NF flights are much more feasible, i.e., the UAV can fly at low altitude. However, in the latter setup, the UAV position accuracy becomes crucial. In this thesis, such accuracy was in the order of 10 cm in altitude and 3 cm in the transverse plane. This means that the maximum measurable frequency is 300 MHz if a maximum position error of $\lambda/10$ is allowed.

In this thesis, both the FF and NF approaches are analyzed and tested on measurements of SKA prototypes. The presented UAV-based measurement setup faces the problem of the missing information of the transmitter phase, i.e., the measured phase is continuously drifting during the flight. A phase reconstruction method using a reference antenna has been presented for both the FF and NF case (see Chapter 2). This method has been applied to UAV-based FF and NF measurements of SKA prototypes to retrieve the correct phase information (see Chapters 3 and 4). The accuracy of this method relies on the knowledge of position and orientation of the UAV and reference antenna, and their radiation patterns.

An inverse source technique has been used as NF-FF transformation (see Chapter 4). This method allows to deal with arbitrary located measurement points. On the other hand, it is not easy to implement, probe correction can be difficult to include and point-matching weights must be carefully chosen[1]. Such NF-FF transformation has been applied to a large horizontal scan made by the UAV. Such a planar acquisition is particularly stable due to the simple rectilinear path the UAV has to follow. As a drawback, the NF-FF transformed data are valid only in a limited angular range. A satisfactory agreement between the NF-FF transformed results and a set of FF measurements has been reached for both EEPs (magnitude and phase) and array pattern. Both are consistent with simulated data.

The presented results demonstrate the feasibility of the NF approach as an effective and fast way to characterize large antenna arrays in their operating environment. This method is capable to characterize digital beamforming arrays by means of two planar NF flights at low altitude. It can be also applied to aperture antennas and analog beamformed arrays by exploiting a receiver with three phase-coherent channels (one for the AUT and two for the dual-polarized reference antenna).

Future studies will be devoted to application of planar NF flights over a fully deployed SKA station (40-m size). Considering the low-directivity elements under test, the UAV altitude must be carefully chosen. In fact, once fixed the desired

[1] see Appendix B, Section "Inverse Source NF-FF Transformation: numerical implementation".

angular validity range of the NF-FF transformation, a smaller altitude would result in a smaller measurement area and hence a faster flight. On the other hand, shortening the UAV altitude increases the multiple reflections between the UAV structure and the AUT. Furthermore, reflections from the ground and from the AUT to the reference antenna could corrupt the reference antenna signal affecting negatively the phase reconstruction. For these reasons, the position of the reference antenna must be carefully chosen (with the possibility to consider more than one reference antenna). Another interesting application is the use of the UAV indoor, e.g., in anechoic chambers. In this case, the UAV position can be acquired through an optical device (e.g., laser tracker system). The measurement accuracy of such instruments is much improved with respect to the GNSS one considered in this thesis. In this way, higher frequencies could be also measured.

References

[1] L. Ciorba, G. Virone, F. Paonessa, S. Matteoli, P. Bolli, E. de Lera Acedo, N. Razavi Ghods, J. Abraham, E. Colin Beltrán, K. Zarb Adami, A. Magro, O. A. Peverini, G. Addamo, G. Giordanengo, M. Righero, and G. Vecchi. Near-field phase reconstruction for uav-based antenna measurements. In *2019 13th European Conference on Antennas and Propagation (EuCAP)*, pages 1–4, 2019.

[2] Jan Svedin, Anders Bernland, Andreas Gustafsson, Eric Claar, and John Luong. Small uav-based sar system using low-cost radar, position, and attitude sensors with onboard imaging capability. *International Journal of Microwave and Wireless Technologies*, 13(6):602–613, 2021.

[3] Wout Joseph, Sam Aerts, Matthias Vandenbossche, Arno Thielens, and Luc Martens. Drone based measurement system for radiofrequency exposure assessment. *Bioelectromagnetics*, 37(3):195–199, 2016.

[4] Ziwei Wang, Ji Zhou, Shaomin Liu, Mingsong Li, Xiaodong Zhang, Zhiming Huang, Weichen Dong, Jin Ma, and Lijiao Ai. A land surface temperature retrieval method for uav broadband thermal imager data. *IEEE Geoscience and Remote Sensing Letters*, 19:1–5, 2022.

[5] Andrey V. Savkin and Hailong Huang. Deployment of unmanned aerial vehicle base stations for optimal quality of coverage. *IEEE Wireless Communications Letters*, 8(1):321–324, 2019.

[6] Yikui Zhai, Qirui Ke, Ying Xu, Wenbo Deng, Junying Gan, Junying Zeng, Wenlve Zhou, Fabio Scotti, Ruggero Donida Labati, and Vincenzo Piuri. Mobile communication base station antenna measurement using unmanned aerial vehicle. *IEEE Access*, 7:119892–119903, 2019.

[7] Alan Salari and Danilo Erricolo. Unmanned aerial vehicles for high-frequency measurements: An accurate, fast, and cost-effective technology. *IEEE Antennas and Propagation Magazine*, 64(1):39–49, 2022.

[8] Ieee recommended practice for antenna measurements. *IEEE Std 149-2021 (Revision of IEEE Std 149-1977)*, pages 1–207, 2022.

[9] Giuseppe Virone, Andrea M. Lingua, Marco Piras, Alberto Cina, Federico Perini, Jader Monari, Fabio Paonessa, Oscar A. Peverini, Giuseppe Addamo, and Riccardo Tascone. Antenna pattern verification system based on a micro unmanned aerial vehicle (uav). *IEEE Antennas and Wireless Propagation Letters*, 13:169–172, 2014.

[10] Fatih Üstüner, Emre Aydemir, Erhan Güleç, Mustafa İlarslan, Mansur Çelebi, and Ekrem Demirel. Antenna radiation pattern measurement using an unmanned aerial vehicle (uav). In *2014 XXXIth URSI General Assembly and Scientific Symposium (URSI GASS)*, pages 1–4, 2014.

[11] I. Farhat, D. Cutajar, K. Zarb Adami, and C. Sammut. Field trials for ultrawideband antenna. In *2018 2nd URSI Atlantic Radio Science Meeting (AT-RASC)*, pages 1–3, 2018.

[12] A. Nelles et al. Calibrating the absolute amplitude scale for air showers measured at LOFAR. *Journal of Instrumentation*, 10(11):P11005–P11005, nov 2015.

[13] Giuseppe Virone, Pietro Bolli, Fabio Paonessa, Giuseppe Pupillo, Stefan J. Wijnholds, Stefania Matteoli, Andrea Maria Lingua, Jader Monari, Giuseppe Addamo, and Oscar A. Peverini. Strong mutual coupling effects on lofar: Modeling and in situ validation. *IEEE Transactions on Antennas and Propagation*, 66(5):2581–2588, 2018.

[14] Fabio Paonessa, Lorenzo Ciorba, Giuseppe Virone, Pietro Bolli, Alessio Magro, Andrew McPhail, Dave Minchin, and Raunaq Bhushan. SKA-Low Prototypes Deployed in Australia: Synoptic of the UAV-Based Experimental Results. *URSI Radio Science Letters*, 2:21, August 2020.

[15] Pietro Bolli, Lorenzo Mezzadrelli, Jader Monari, Federico Perini, Alberto Tibaldi, Giuseppe Virone, Mirko Bercigli, Lorenzo Ciorba, Paola Di Ninni, Maria Grazia Labate, Vittorio Giuseppe Loi, Andrea Mattana, Fabio Paonessa, Simone Rusticelli, and Marco Schiaffino. Test-driven design of an active dual-polarized log-periodic antenna for the square kilometre array. *IEEE Open Journal of Antennas and Propagation*, 1:253–263, 2020.

[16] G. Pupillo, G. Naldi, G. Bianchi, A. Mattana, J. Monari, F. Perini, M. Poloni, M. Schiaffino, P. Bolli, A. Lingua, I. Aicardi, H. Bendea, P. Maschio, M. Piras, G. Virone, F. Paonessa, Z. Farooqui, A. Tibaldi, G. Addamo, O. A. Peverini, R. Tascone, and S. J. Wijnholds. Medicina array demonstrator: calibration and radiation pattern characterization using a UAV-mounted radio-frequency source. *Experimental Astronomy*, 39(2):405–421, June 2015.

[17] P. Bolli, G. Pupillo, G. Virone, M. Z. Farooqui, A. Lingua, A. Mattana, J. Monari, M. Murgia, G. Naldi, F. Paonessa, F. Perini, S. Pluchino, S. Rusticelli, M. Schiaffino, F. Schillirò, G. Tartarini, and A. Tibaldi. From mad to sad: The italian experience for the low-frequency aperture array of ska1-low. *Radio Science*, 51(3):160–175, 2016.

[18] Daniel et al. Jacobs. First demonstration of echo: an external calibrator for hydrogen observatories. 129(973):035002, 2017.

[19] Martínez Picar et al. Antenna pattern calibration of radio telescopes using an uav-based device. In *2015 International Conference on Electromagnetics in Advanced Applications (ICEAA)*, pages 981–984, 2015.

[20] Iman Farhat, Denis Cutajar, Kristian Zarb Adami, Charles Sammut, and John Abela. Characterization of 36 meter square mid-frequency radio astronomy prototype antenna array. In *2018 IEEE Conference on Antenna Measurements Applications (CAMA)*, pages 1–3, 2018.

[21] Fabio Paonessa, Giuseppe Virone, Lorenzo Ciorba, Giuseppe Addamo, Mauro Lumia, Gianluca Dassano, Mario Zannoni, Cristian Franceschet, and Oscar A. Peverini. Design and verification of a <italic>q</italic>-band test source for uav-based radiation pattern measurements. *IEEE Transactions on Instrumentation and Measurement*, 69(12):9366–9370, 2020.

[22] Libe Washburn, Eduardo Romero, Cyril Johnson, Chris Gotschalk, and Brian Emery. Antenna calibration for oceanographic radars using aerial drones. In *2016 IEEE Conference on Antenna Measurements Applications (CAMA)*, pages 1–4, 2016.

[23] Yingwei Tian, Biyang Wen, Ziyan Li, Yukun Yin, and Weimin Huang. Analysis and validation of an improved method for measuring hf surface wave radar antenna pattern. *IEEE Antennas and Wireless Propagation Letters*, 18(4):659–663, 2019.

[24] Simon Duthoit, Jorge L. Salazar, William Doyle, Antonio Segales, Brent Wolf, Caleb Fulton, and Phillip Chilson. A new approach for in-situ antenna characterization, radome inspection and radar calibration, using an unmanned aircraft system (uas). In *2017 IEEE Radar Conference (RadarConf)*, pages 0669–0674, 2017.

[25] Yasser Hussein, Joshua Miller, Vachik Garkanian, and Emmanuel Decrossas. Far-field pattern measurement and simulation of vhf antenna at 60 mhz for europa clipper mission. In *2018 IEEE Symposium on Electromagnetic Compatibility, Signal Integrity and Power Integrity (EMC, SI, PI)*, pages 94–98, 2018.

[26] Jason Schreiber. Antenna pattem reconstitution using unmanned aerial vehicles (uavs). In *2016 IEEE Conference on Antenna Measurements Applications (CAMA)*, pages 1–3, 2016.

[27] Marjo Heikkilä, Marjut Koskela, Tero Kippola, Mahmut Kocak, Juha Erkkilä, and Jouni Tervonen. Using unmanned aircraft systems for mobile network verifications. In *2018 IEEE 29th Annual International Symposium on Personal, Indoor and Mobile Radio Communications (PIMRC)*, pages 805–811, 2018.

[28] Andrés Navarro Cadavid, Jaime Aristizabal, and Marcos Duván Pineda Alhucema. Antenna pattern verification for digital tv broadcast systems in andean countries based on uav's. In *2018 IEEE-APS Topical Conference on Antennas and Propagation in Wireless Communications (APWC)*, pages 858–861, 2018.

[29] María García-Fernández, Yuri Álvarez López, Ana Arboleya, Borja González-Valdés, Yolanda Rodríguez-Vaqueiro, María Elena De Cos Gómez, and Fernando Las-Heras Andrés. Antenna diagnostics and characterization using unmanned aerial vehicles. *IEEE Access*, 5:23563–23575, 2017.

[30] Maria Garcia-Fernandez, Yuri Alvarez Lopez, and Fernando Las-Heras Andres. Unmanned aerial system for antenna measurement and diagnosis: evaluation and testing. *IET Microwaves, Antennas & Propagation*, 13(13):2224–2231, 2019.

[31] Pietro Bolli, Giuseppe Pupillo, Fabio Paonessa, Giuseppe Virone, Stefan J. Wijnholds, and Andrea Maria Lingua. Near-field experimental verification of the em models for the lofar radio telescope. *IEEE Antennas and Wireless Propagation Letters*, 17(4):613–616, 2018.

[32] Raimund A. M. Mauermayer, Jonas Kornprobst, and Torsten Fritzel. A low-cost multicopter based near-field antenna measurement system employing software defined radio and 6-d laser metrology. In *2019 Antenna Measurement Techniques Association Symposium (AMTA)*, pages 1–5, 2019.

[33] Giuseppe Virone, Fabio Paonessa, Lorenzo Ciorba, Stefania Matteoli, Pietro Bolli, Stefan J. Wijnholds, and Giuseppe Addamo. Measurement of the LOFAR-HBA beam patterns using an unmanned aerial vehicle in the near field. *Journal of Astronomical Telescopes, Instruments, and Systems*, 8(1):1 – 14, 2021.

[34] Lorenzo Ciorba, Giuseppe Virone, Fabio Paonessa, Marco Righero, Eloy De Lera Acedo, Stefania Matteoli, Edgar Colin Beltran, Pietro Bolli, Giorgio Giordanengo, Giuseppe Vecchi, Alessio Magro, Riccardo Chiello, Oscar A. Peverini, and Giuseppe Addamo. Large horizontal near-field scanner based on a non-tethered unmanned aerial vehicle. *IEEE Open Journal of Antennas and Propagation*, 3:568–582, 2022.

[35] I. Farhat, D. Cutajar, M. Bezzina, and K. Zarb Adami. Drone characterization approach for radio telescopes. In *2019 PhotonIcs Electromagnetics Research Symposium - Spring (PIERS-Spring)*, pages 3016–3018, 2019.

[36] Chihway Chang, Christian Monstein, Alexandre Refregier, Adam Amara, Adrian Glauser, and Sarah Casura. Beam calibration of radio telescopes with drones. *Publications of the Astronomical Society of the Pacific*, 127(957):1131–1143, nov 2015.

[37] Torsten Fritzel, Rüdiger Strauß, Hans-Jürgen Steiner, Christoph Eisner, and Thomas Eibert. Introduction into an uav-based near-field system for in-situ and large-scale antenna measurements (invited paper). In *2016 IEEE Conference on Antenna Measurements Applications (CAMA)*, pages 1–3, 2016.

[38] Fabian T. Faul, Daniel Korthauer, and Thomas F. Eibert. Impact of rotor blade rotation of uavs on electromagnetic field measurements. *IEEE Transactions on Instrumentation and Measurement*, 70:1–9, 2021.

[39] G. Virone, F. Paonessa, L. Ciorba, M. Lumia, G. Addamo, O. A. Peverini, and P. Bolli. Effect of conductive propellers on vhf uav-based antenna measurements: Simulated results. In *2021 15th European Conference on Antennas and Propagation (EuCAP)*, pages 1–4, 2021.

[40] Giuseppe Virone, Fabio Paonessa, Lorenzo Ciorba, Mauro Lumia, Giuseppe Addamo, Oscar Antonio Peverini, and Pietro Bolli. Effect of conductive propellers on vhf uav-based antenna measurements: Experimental results. In *2021 IEEE Conference on Antenna Measurements Applications (CAMA)*, pages 46–47, 2021.

[41] F. Paonessa. *VHF/UHF Antenna Array Measurements with a UAV-based Test Source*. PhD thesis, Politecnico di Torino, Electronics Engineering, 2017.

[42] Giovanni Naldi, Andrea Mattana, Sandro Pastore, Monica Alderighi, Kristian Zarb Adami, Francesco Schillirò, Amin Aminaei, Jeremy Baker, Carolina Belli, Gianni Comoretto, Simone Chiarucci, Riccardo Chiello, Sergio D'Angelo, Gabriele Dalle Mura, Andrea De Marco, Rob Halsall, Alessio Magro, Jader Monari, Matt Roberts, Federico Perini, Marco Poloni, Giuseppe Pupillo, Simone Rusticelli, Marco Schiaffino, and Emanuele Zaccaro. The digital signal processing platform for the low frequency aperture array: Preliminary results on the data acquisition unit. *Journal of Astronomical Instrumentation*, 06(01):1641014, 2017.

[43] Wei Fan, Fengchun Zhang, and Zhengpeng Wang. Over-the-air testing of 5g communication systems: Validation of the test environment in simple-sectored multiprobe anechoic chamber setups. *IEEE Antennas and Propagation Magazine*, 63(1):40–50, 2021.

[44] Ieee standard test procedures for antennas. *ANSI/IEEE Std 149-1979*, pages 1–144, 1979.

[45] Rohan Chandra, Tom Goldstein, and Christoph Studer. Phasepack: A phase retrieval library. In *2019 13th International conference on Sampling Theory and Applications (SampTA)*, pages 1–5, 2019.

[46] Jonas Kornprobst, Alexander Paulus, Josef Knapp, and Thomas F. Eibert. Phase retrieval for partially coherent observations. *IEEE Transactions on Signal Processing*, 69:1394–1406, 2021.

[47] Alexander Paulus, Josef Knapp, Jonas Kornprobst, and Thomas F. Eibert. Reliable linearized phase retrieval for near-field antenna measurements with truncated measurement surfaces. *IEEE Transactions on Antennas and Propagation*, pages 1–1, 2022.

[48] G. Serra, P. Bolli, G. Busonera, T. Pisanu, S. Poppi, F. Gaudiomonte, G. Zacchiroli, J. Roda, M. Morsiani, and J. A. López-Pérez. The microwave holography system for the Sardinia Radio Telescope. In Larry M. Stepp, Roberto Gilmozzi, and Helen J. Hall, editors, *Ground-based and Airborne Telescopes IV*, volume 8444, pages 1877 – 1891. International Society for Optics and Photonics, SPIE, 2012.

[49] Sandra Costanzo and Giuseppe Di Massa. An integrated probe for phaseless near-field measurements. *Measurement*, 31(2):123–129, 2002.

[50] Alexander Paulus, Josef Knapp, and Thomas F. Eibert. Phaseless near-field far-field transformation utilizing combinations of probe signals. *IEEE Transactions on Antennas and Propagation*, 65(10):5492–5502, 2017.

[51] S. Costanzo and G. Di Massa. Spatial domain indirect holographic technique for antenna near-field phaseless measurements. *Radio Science*, 52(4):432–438, 2017.

[52] Jaime Laviada Martínez, Ana Arboleya-Arboleya, Yuri Álvarez López, Cebrián García-González, and Fernando Las-Heras. Phaseless antenna diagnostics based on off-axis holography with synthetic reference wave. *IEEE Antennas and Wireless Propagation Letters*, 13:43–46, 2014.

[53] T. D. Carozzi and G. Woan. A fundamental figure of merit for radio polarimeters. *IEEE Transactions on Antennas and Propagation*, 59(6):2058–2065, 2011.

[54] Stefan J. Wijnholds and Wim A. van Cappellen. In situ antenna performance evaluation of the lofar phased array radio telescope. *IEEE Transactions on Antennas and Propagation*, 59(6):1981–1989, 2011.

[55] Paola Di Ninni, Mirko Bercigli, Pietro Bolli, Giuseppe Virone, and Stefan J. Wijnholds. Mutual coupling analysis for a ska1-low station. In *2019 13th European Conference on Antennas and Propagation (EuCAP)*, pages 1–5, 2019.

[56] Randall Wayth, Marcin Sokolowski, Tom Booler, Brian Crosse, David Emrich, Robert Grootjans, Peter J. Hall, Luke Horsley, Budi Juswardy, David Kenney, and et al. The engineering development array: A low frequency radio telescope utilising ska precursor technology. *Publications of the Astronomical Society of Australia*, 34:e034, 2017.

[57] U. Kiefner, R. B. Wayth, D. B. Davidson, and M. Sokolowski. Holographic calibration of phased array telescopes. *Radio Science*, 56(5):e2020RS007171, 2021. e2020RS007171 2020RS007171.

[58] G. Virone, F. Paonessa, O. A. Peverini, G. Addamo, R. Orta, R. Tascone, and P. Bolli. Antenna pattern measurements with a flying far-field source (hexacopter). In *2014 IEEE Conference on Antenna Measurements Applications (CAMA)*, pages 1–2, 2014.

[59] Fabio Paonessa, Lorenzo Ciorba, Giuseppe Virone, Pietro Bolli, Jader Monari, Federico Perini, Randall Wayth, Adrian Sutinjo, and David Davidson. Characterization of the murchison widefield array dipole with a uav-mounted test source. In *2019 13th European Conference on Antennas and Propagation (EuCAP)*, pages 1–4, 2019.

[60] Sergey Pivnenko, Janus E. Pallesen, Olav Breinbjerg, Manuel Sierra Castaner, Pablo Caballero Almena, Cristian MartÍnez Portas, JosÉ Luis Besada Sanmartin, Jordi Romeu, Sebastian Blanch, JosÉ M. Gonzalez-Arbesu, Christian Sabatier, Alain Calderone, GÉrard Portier, HÅkan Eriksson, and Jan Zackrisson. Comparison of antenna measurement facilities with the dtu-esa 12 ghz validation standard antenna within the eu antenna centre of excellence. *IEEE Transactions on Antennas and Propagation*, 57(7):1863–1878, 2009.

[61] Lorenzo Ciorba et. al. Understanding phase pattern discrepancies in uav based measurements of a ska-low prototype. In *2022 16th European Conference on Antennas and Propagation (EuCAP)*, 2022.

[62] Bolli P. Paonessa F. et al. de Lera Acedo, E. Ska aperture array verification system: electromagnetic modeling and beam pattern measurements using a micro uav. *Experimental Astronomy*, 45:1–20, 2018.

[63] B. Wakley E. de Lera Acedo, N. Drought and A. Faulkner. Evolution of skala (skala-2), the log-periodic array antenna for the ska-low instrument. In *2015 International Conference on Electromagnetics in Advanced Applications (ICEAA)*, pages 839–843, 2015.

[64] Alessio Magro, Riccardo Chiello, Cristian Albanese, Jeremy Baker, Gianni Comoretto, Andrea DeMarco, Alessio Gravina, Rob Halsall, Matthew Roberts, and Kristian Zarb Adami. A software infrastructure for firmware-software interaction: The case of tpms. In *2017 International Conference on Signals and Systems (ICSigSys)*, pages 190–196, 2017.

[65] Alessio Magro, Keith Bugeja, Riccardo Chiello, and Andrea DeMarco. A high-performance, flexible data acquisition library for radio instruments. In *2019 IEEE-APS Topical Conference on Antennas and Propagation in Wireless Communications (APWC)*, pages 069–074, 2019.

[66] D. M. Kerns. Plane-wave scattering-matrix theory of antennas and antenna-antenna interactions: Formulation and applications. In *Journal of Research of the National Bureau of Standards*, volume 80B, page 5–51, 1976.

[67] Francesco D'Agostino, Flaminio Ferrara, Claudio Gennarelli, Rocco Guerriero, Scott McBride, and Massimo Migliozzi. Fast and accurate antenna pattern evaluation from near-field data acquired via planar spiral scanning. *IEEE Transactions on Antennas and Propagation*, 64(8):3450–3458, 2016.

[68] F. D'Agostino, F. Ferrara, C. Gennarelli, R. Guerriero, and M. Migliozzi. An svd-based approach to reconstruct the planar wide-mesh scanning nf data

from inaccurately probe-positioned samples. *IEEE Antennas and Wireless Propagation Letters*, 17(4):641–644, 2018.

[69] Ieee recommended practice for near-field antenna measurements. *IEEE Std 1720-2012*, pages 1–102, 2012.

[70] Ole Neitz, Raimund A. M. Mauermayer, Yvonne Weitsch, and Thomas F. Eibert. A propagating plane-wave-based near-field transmission equation for antenna gain determination from irregular measurement samples. *IEEE Transactions on Antennas and Propagation*, 65(8):4230–4238, 2017.

[71] Quentin Gueuning, Jean Cavillot, Stuart Gregson, Christophe Craeye, Eloy de Lera Acedo, Anthony K Brown, and Clive Parini. Plane-wave spectrum methods for the near-field characterization of very large structures using uavs: The ska radio telescope case. In *2021 15th European Conference on Antennas and Propagation (EuCAP)*, pages 1–5, 2021.

[72] R. Cornelius, T. Salmerón-Ruiz, F. Saccardi, L. Foged, D. Heberling, and M. Sierra-Castañer. A comparison of different methods for fast single-cut near-to-far-field transformation [euraap corner]. *IEEE Antennas and Propagation Magazine*, 56(2):252–261, 2014.

[73] M. Sierra-Castañer, F. Saccardi, and L. J. Foged. Gain antenna measurement using single cut near field measurements. In *AMTA 2016 Proceedings*, pages 1–4, 2016.

[74] M. Ayyaz Qureshi, Carsten H. Schmidt, and Thomas F. Eibert. Efficient near-field far-field transformation for nonredundant sampling representation on arbitrary surfaces in near-field antenna measurements. *IEEE Transactions on Antennas and Propagation*, 61(4):2025–2033, 2013.

[75] Giuseppe Vecchi Javier Leonardo Araque Quijano. Field and source equivalence in source reconstruction on 3d surfaces. *Progress In Electromagnetics Research*, 103:67–100, 2010.

[76] Jonas Kornprobst, Josef Knapp, Raimund A. M. Mauermayer, Ole Neitz, Alexander Paulus, and Thomas F. Eibert. Accuracy and conditioning of surface-source based near-field to far-field transformations. *IEEE Transactions on Antennas and Propagation*, 69(8):4894–4908, 2021.

[77] Thomas F. Eibert, Dario Vojvodić, and Thorkild B. Hansen. Fast inverse equivalent source solutions with directive sources. *IEEE Transactions on Antennas and Propagation*, 64(11):4713–4724, 2016.

[78] S. Rao, D. Wilton, and A. Glisson. Electromagnetic scattering by surfaces of arbitrary shape. *IEEE Transactions on Antennas and Propagation*, 30(3):409–418, 1982.

[79] L. Scialacqua, F. Mioc, L. J. Foged, G. Giordanengo, M. Righero, and G. Vecchi. Diagnostics on electrically large structures by a nested skeletonization scheme enhancement of the equivalent current technique. In *2020 14th European Conference on Antennas and Propagation (EuCAP)*, pages 1–4, 2020.

[80] L. Scialaequa, F. Scattone, A. Giacomini, L.J. Foged, and F. Mioc. Advanced diagnostics on a large array by the equivalent current technique. In *2021 Antenna Measurement Techniques Association Symposium (AMTA)*, pages 1–5, 2021.

[81] A.C. Newell. Error analysis techniques for planar near-field measurements. *IEEE Transactions on Antennas and Propagation*, 36(6):754–768, 1988.

[82] Fabio Paonessa, Giuseppe Virone, Pietro Bolli, and Andrea M. Lingua. Uav-based antenna measurements: Scan strategies. In *2017 11th European Conference on Antennas and Propagation (EUCAP)*, pages 1303–1305, 2017.

[83] A. J. Devaney and E. Wolf. Radiating and nonradiating classical current distributions and the fields they generate. *Phys. Rev. D*, 8:1044–1047, Aug 1973.

[84] A. Devaney and G. Sherman. Nonuniqueness in inverse source and scattering problems. *IEEE Transactions on Antennas and Propagation*, 30(5):1034–1037, 1982.

[85] R. Albanese and Peter Monk. The inverse source problem for maxwell's equations. *Inverse Problems*, 22:1023–1035, 06 2006.

[86] E.A. Marengo and A.J. Devaney. The inverse source problem of electromagnetics: linear inversion formulation and minimum energy solution. *IEEE Transactions on Antennas and Propagation*, 47(2):410–412, 1999.

[87] R. P. Porter and A. J. Devaney. Holography and the inverse source problem. *J. Opt. Soc. Am.*, 72(3):327–330, Mar 1982.

[88] E.A. Marengo, A.J. Devaney, and F.K. Gruber. Inverse source problem with reactive power constraint. *IEEE Transactions on Antennas and Propagation*, 52(6):1586–1595, 2004.

[89] Roger F. Harrington. *Some Theorems and Concepts*, pages 95–142. 2001.

[90] Andreas Kirsch and Frank Hettlich. *The Mathematical Theory of Time-Harmonic Maxwell's Equations: Expansion-, Integral-, and Variational Methods. Boundary Integral Equation Methods for Lipschitz Domains*, pages 227–311. Springer International Publishing, Cham, 2015.

[91] Lars Garding. *Some Points of Analysis and Their History, Dirichlet's problem and Garding's inequality (chapter 10)*, volume 11, page 66. 1997.

[92] Steven G. Krantz and Harold R. Parks. *A primer of real analytic functions, 2nd edition*, page 14. 2002.

[93] Martin Stumpf. *Time-Domain Electromagnetic Reciprocity in Antenna Modeling, Introduction*. 2019.

[94] R. A. M. Mauermayer O. Neitz T. F. Eibert, E. Kilic¸ and G. Schnattinger. Electromagnetic field transformations for measurements and simulations (invited paper). *Progress In Electromagnetics Research*, 151:127–150, 2015.

[95] Carsten H. Schmidt, Martin M. Leibfritz, and Thomas F. Eibert. Fully probe-corrected near-field far-field transformation employing plane wave expansion and diagonal translation operators. *IEEE Transactions on Antennas and Propagation*, 56(3):737–746, 2008.

[96] Javier Leonardo Araque Quijano and Giuseppe Vecchi. Improved-accuracy source reconstruction on arbitrary 3-d surfaces. *IEEE Antennas and Wireless Propagation Letters*, 8:1046–1049, 2009.

Appendix A

Uniqueness of the Inverse Source Problem

In this Appendix, uniqueness of the inverse source problem for time-harmonic Maxwell's equations is addressed. Aim of the chapter is to prove mathematically the uniqueness of such problem (see lemma A.2.1). For this reason, the chapter has a rigorous mathematical approach.

A.1 Motivations

Inverse source is a well known method that has been successfully exploited in the electromagnetic community in order to obtain information on a radio-frequency source. In particular, this technique has been widely used for NF-FF transformations and antenna diagnostics. For this reason, it is fundamental to understand if the problem is well.posed. In particular, in this work uniqueness of the inverse source problem is considered.

The inverse source problem is substantially a back-propagation problem. Known the tangential electric field over a virtual surface Γ (where the field is usually measured), the tangential electromagnetic field over a surface Σ must be determined. The virtual (non-physical) surface Σ is located in the region enclosed by the measurement surface Γ.

It is well know that the inverse source problem for volume currents is ill-posed (the solution is not unique) [83], [84], [85]. This is due to the fact that there exist volume

currents that radiate a null field. Other researches has shown that through the inverse source problem is possible to compute the minimum energy solution [85], [86], [87], [88] whereas it is not possible to obtain the non-radiating part. In [85] the inverse source problem for an electric surface current only (no magnetic current, no null field condition inside the virtual surface) is addressed.
Here, the inverse source problem for time-harmonic Maxwell's equations for equivalent surface electric and magnetic currents with Love's condition (null field inside virtual surface) is instead considered.

A.1.1 Equivalence Theorem

In this Section, the equivalence theorem [89] (and its connection to the inverse source problem) is briefly presented and analyzed.
A surface Σ that encloses the source and possible scatterers is considered. In this way, the region outside Σ consists of free space. The equivalence theorem states that there exist electric $\mathbf{J}$ and magnetic $\mathbf{M}$ currents defined over Σ that radiate the same field of the source in the region exterior to Σ.
More precisely, an arbitrary electromagnetic field $\mathbf{E}^-, \mathbf{H}^- \in C^1(B, \mathbb{C}^3) \cap C(\overline{B}, \mathbb{C}^3)$ in B and $\mathbf{E}^+, \mathbf{H}^+ \in C^1(\mathbb{R}^3 \setminus \overline{B}, \mathbb{C}^3) \cap C(\mathbb{R}^3 \setminus B, \mathbb{C}^3)$ in $\mathbb{R}^3 \setminus \overline{B}$, i.e. solutions of Maxwell's equations (for $\mathbb{R}^3 \setminus \overline{B}$, the Silver Muller radiation condition must be included) can be considered[1]. Equivalence theorem states that surface currents $\mathbf{M} := (\mathbf{E}^+ - \mathbf{E}^-) \times \mathbf{n}$ and $\mathbf{J} := \mathbf{n} \times (\mathbf{H}^+ - \mathbf{H}^-)$ radiate fields $\mathbf{E}^-, \mathbf{H}^-$ in B and $\mathbf{E}^+, \mathbf{H}^+$ in $\mathbb{R}^3 \setminus \overline{B}$, where $\mathbf{n}$ is the unit normal outward vector over Σ. In this Chapter, Love's currents (null field inside B, i.e., $\mathbf{E}^- = \mathbf{H}^- = 0$ in B) are considered, i.e., $\mathbf{J} := \mathbf{n} \times \mathbf{H}^+$ and $\mathbf{M} := \mathbf{E}^+ \times \mathbf{n}$.
Using the equivalence theorem, the problem of determining the field $\mathbf{E}^+$ is transformed to the determination of the unknown currents $\mathbf{J}$ and $\mathbf{M}$. The usual way to find these currents is to enforce that such currents radiate a field equal to the measured one, over the finite set of points in Γ where measurements are made. Of course, a discretization of the radiation operator which maps currents over Σ to the field over measurement points in Γ is needed. In this way, once obtained (an approximation of) currents $\mathbf{J}$ and $\mathbf{M}$, fields in $\mathbb{R}^3 \setminus \overline{B}$ can be computed. In particular, the far-field of the considered source is obtained.
It should be noted that the equivalence theorem gives a proof on the existence of the considered currents $\mathbf{J}$ and $\mathbf{M}$ that radiates the measured tangential electric field on Γ.

[1] Definition of the function spaces $C^1(B, \mathbb{C}^3)$ and $C(\overline{B}, \mathbb{C}^3)$ can be found in Appendix B.

However, (to the best of the author's knowledge) the equivalence theorem does not answer to the uniqueness problem considered in this Chapter.

A.2 Uniqueness of Inverse Source Currents

Aim: prove that $\mathbf{E}\times\mathbf{n}$ over the measurement surface Γ uniquely determines the tangential fields $\mathbf{E}\times\mathbf{n}$ and $\mathbf{n}\times\mathbf{H}$ over Σ. Magnetic $\mathbf{M}$ and electric $\mathbf{J}$ currents are defined as $\mathbf{M}:=\mathbf{E}\times\mathbf{n}$ and $\mathbf{J}:=\mathbf{n}\times\mathbf{H}$ over Σ. Currents $\mathbf{J}$ and $\mathbf{M}$ are also called equivalent currents. Aim of this chapter is to prove that $\mathbf{E}\times\mathbf{n}$ over Γ uniquely determines currents $\mathbf{J}$ and $\mathbf{M}$ over Σ. The proof can be found in lemma A.2.1.
A schematic of the inverse source problem is shown in Fig. A.1. Domains $\Omega\subset\mathbb{R}^3$ and $B\subset\mathbb{R}^3$ with $B\subset\Omega$ are open bounded (connected with connected complement) smooth domains. It is recalled that the electromagnetic field $\mathbf{E},\mathbf{H}$ satisfy

$$\begin{cases}\nabla\times\mathbf{E}=-j\omega\mu\mathbf{H} & \text{in } \mathbb{R}^3\setminus\overline{B}\\ \nabla\times\mathbf{H}=j\omega\varepsilon\mathbf{E} & \text{in } \mathbb{R}^3\setminus\overline{B}\\ \text{Silver Muller radiation condition}\end{cases}\tag{A.1}$$

where the Silver Muller radiation condition is

$$\mathbf{E}(\mathbf{x})-Z_0\mathbf{H}(\mathbf{x})\times\frac{\mathbf{x}}{|\mathbf{x}|}=O(\frac{1}{|\mathbf{x}|^2})\qquad |\mathbf{x}|\longrightarrow+\infty\tag{A.2}$$

uniformly with respect to $\mathbf{x}/|\mathbf{x}|\in S^2$.

Guidelines for the reader: The proof is divided in the following points:

- from the tangential electric field $\mathbf{E}\times\mathbf{n}$ over the measurement surface Γ it is possible to uniquely determine the electric field $\mathbf{E}$ in the region exterior to Γ, i.e., $\mathbb{R}^3\setminus\overline{\Omega}$.
- the electric field $\mathbf{E}$ satisfies Helmholtz equation in $\mathbb{R}^3\setminus\overline{B}$. Solutions of Helmholtz equation are analytic.
- roughly speaking, if two analytic functions are equal over a small set, then they are equal over the bigger set where they are analytic (see lemma A.3.1).

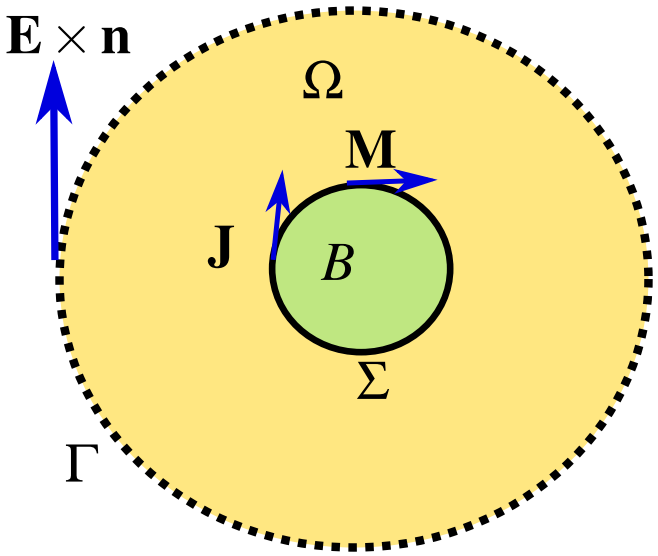

Fig. A.1 Schematic of the inverse source problem. The surface Γ (dashed black line) represents the surface where the tangential electric field $\mathbf{E} \times \mathbf{n}$ is measured. Currents $\mathbf{J}$ and $\mathbf{M}$ over the virtual surface Σ (solid black line) are determined from the tangential electric field $\mathbf{E} \times \mathbf{n}$ over Γ. The domain B (green) is the inner domain with boundary $\partial B = \Sigma$. Similarly, the domain Ω (yellow) is the inner domain with boundary $\partial \Omega = \Gamma$

In this way, $\mathbf{E}$ must be equal to any other possible field which exists in $\mathbb{R}^3 \setminus \overline{B}$ (with the same $\mathbf{E} \times \mathbf{n}$ over Γ).

- finally, currents $\mathbf{E} \times \mathbf{n}$ and $\mathbf{n} \times \mathbf{H}$ over Σ are uniquely determined.

Notation:

- $\Gamma = \partial \Omega$ is the surface where the tangential electric field is known (e.g., measured).
- Ω is the volume enclosed by the measurement surface Γ.
- $\Sigma = \partial B$ is the surface where equivalent currents are placed.
- B is the volume enclosed by Σ.
- $\mathbf{n} =$ is the unit outward normal vector.
- $Z_0 = \sqrt{\mu/\varepsilon}$ is the free space impedance.

It should be recalled that $H(\text{Curl}, \Omega)$ is the space of functions $\mathbf{e} : \Omega \longrightarrow \mathbb{C}^3$ such that $\mathbf{e} \in L^2(\Omega, \mathbb{C}^3)$ and $\nabla \times \mathbf{e} \in L^2(\Omega, \mathbb{C}^3)$, where $L^2(\Omega, \mathbb{C}^3)$ is the space of vector fields with each component in $L^2(\Omega)$.
In this work, spaces $H^{-1/2}(\text{Div}, \Sigma)$ and $H^{-1/2}(\text{Curl}, \Sigma)$ are not introduced, for their definitions see [90].
The space $H_{loc}(\text{curl}, \mathbb{R}^3 \setminus \overline{B})$ is defined as

$$H_{loc}(\text{curl}, \mathbb{R}^3 \setminus \overline{B}) = \{\mathbf{e} : \mathbb{R}^3 \setminus \overline{B} \longrightarrow \mathbb{C}^3 \text{ s.t.} \\ \mathbf{e}|_{B_R \setminus \overline{B}} \in H(\text{curl}, B_R \setminus \overline{B}) \text{ for any } R \geq R_0\}$$

where B_R is the open ball centered at origin of radius R and R_0 is the radius of the ball which contains B.

Lemma A.2.1 (uniqueness of inverse source)**.** *Given*
$\mathbf{E}$, $\mathbf{H} \in H_{loc}(curl, \mathbb{R}^3 \setminus \overline{B})$ *such that*

$$\begin{cases} \nabla \times \mathbf{E} = -j\omega\mu\mathbf{H} & in\ \mathbb{R}^3 \setminus \overline{B} \\ \nabla \times \mathbf{H} = j\omega\varepsilon\mathbf{E} & in\ \mathbb{R}^3 \setminus \overline{B} \\ \mathbf{E}(\mathbf{x}) - Z_0\mathbf{H}(\mathbf{x}) \times \frac{\mathbf{x}}{|\mathbf{x}|} = O(\frac{1}{|\mathbf{x}|^2}) & |\mathbf{x}| \longrightarrow +\infty \end{cases} \tag{A.3}$$

then currents $\mathbf{J}$, $\mathbf{M} \in H^{-1/2}(Div, \Sigma)$ *such that* $\mathbf{J} = \mathbf{n} \times \mathbf{H}$ *and* $\mathbf{M} = \mathbf{E} \times \mathbf{n}$ *on* Σ *are uniquely determined by* $\mathbf{E} \times \mathbf{n}$ *over the measurement surface* Γ.

Proof. Let's assume that there exist an electromagnetic field
$(\mathbf{e}, \mathbf{h}) \in H_{loc}(\text{curl}, \mathbb{R}^3 \setminus \overline{B}) \times H_{loc}(\text{curl}, \mathbb{R}^3 \setminus \overline{B})$ such that $\mathbf{e} \times \mathbf{n} = \mathbf{E} \times \mathbf{n}$ on Γ. The proof consists in demonstrating that this implies $\mathbf{e} = \mathbf{E}$ and $\mathbf{h} = \mathbf{H}$ in $\mathbb{R}^3 \setminus \overline{B}$ and hence $\mathbf{e} \times \mathbf{n} = \mathbf{E} \times \mathbf{n}$ and $\mathbf{n} \times \mathbf{h} = \mathbf{n} \times \mathbf{H}$ on Σ.
The electromagnetic field $\mathbf{e}$, $\mathbf{h}$ must satisfy

$$\begin{cases} \nabla \times \mathbf{e} = -j\omega\mu\mathbf{h} & \text{in } \mathbb{R}^3 \setminus \overline{B} \\ \nabla \times \mathbf{h} = j\omega\varepsilon\mathbf{e} & \text{in } \mathbb{R}^3 \setminus \overline{B} \\ \mathbf{e}(\mathbf{x}) - Z_0\mathbf{h}(\mathbf{x}) \times \frac{\mathbf{x}}{|\mathbf{x}|} = O(\frac{1}{|\mathbf{x}|^2}) & |\mathbf{x}| \longrightarrow +\infty \end{cases} \tag{A.4}$$

Because $(\mathbf{e}, \mathbf{h}) \in H_{loc}(\text{curl}, \mathbb{R}^3 \setminus \overline{B}) \times H_{loc}(\text{curl}, \mathbb{R}^3 \setminus \overline{B})$ then $(\mathbf{e}, \mathbf{h}) \in H_{loc}(\text{curl}, \mathbb{R}^3 \setminus \overline{\Omega}) \times H_{loc}(\text{curl}, \mathbb{R}^3 \setminus \overline{\Omega})$.
From the uniqueness of the exterior boundary value problem (see pages 303- 309, theorem 5.64 in [90]), given an arbitrary $\boldsymbol{\lambda} \in H^{-1/2}(\text{Div}, \Gamma)$, there exists a unique solution $(\mathbf{e}, \mathbf{h}) \in H_{loc}(\text{curl}, \mathbb{R}^3 \setminus \overline{\Omega}) \times H_{loc}(\text{curl}, \mathbb{R}^3 \setminus \overline{\Omega})$ of:

$$\begin{cases} \nabla \times \mathbf{e} = -j\omega\mu\mathbf{h} & \text{in } \mathbb{R}^3 \setminus \overline{\Omega} \\ \nabla \times \mathbf{h} = j\omega\varepsilon\mathbf{e} & \text{in } \mathbb{R}^3 \setminus \overline{\Omega} \\ \mathbf{e} \times \mathbf{n} = \boldsymbol{\lambda} & \text{on } \Gamma \\ \mathbf{e}(\mathbf{x}) - Z_0\mathbf{h}(\mathbf{x}) \times \frac{\mathbf{x}}{|\mathbf{x}|} = O(\frac{1}{|\mathbf{x}|^2}) & |\mathbf{x}| \longrightarrow +\infty \end{cases} \tag{A.5}$$

Considering $\boldsymbol{\lambda} = \mathbf{E} \times \mathbf{n}$ on Γ then $\mathbf{e} = \mathbf{E}$ in $\mathbb{R}^3 \setminus \overline{\Omega}$ from the uniqueness of the exterior boundary value problem.
Each cartesian component of $\mathbf{E}$ (or equivalently $\mathbf{e}$) is analytic over the open connected

set $\mathbb{R}^3 \setminus \overline{B}$ (see the proof below). Because $\mathbf{e}|_{\mathbb{R}^3\setminus\overline{\Omega}} = \mathbf{E}|_{\mathbb{R}^3\setminus\overline{\Omega}}$, then $\mathbf{e} = \mathbf{E}$ on $\mathbb{R}^3 \setminus \overline{B}$ by lemma A.3.2. This implies $\mathbf{h} = \mathbf{H}$ on $\mathbb{R}^3 \setminus \overline{B}$. The proof of lemma A.2.1 is concluded. In next part, it is proved that each cartesian component of the electric field $\mathbf{E}$ (or equivalently $\mathbf{e}$) is analytic over $\mathbb{R}^3 \setminus \overline{B}$. Because $\mathbf{E}$ satisfies

$$\nabla \times \nabla \times \mathbf{E} - k^2\mathbf{E} = 0 \quad \text{over } \mathbb{R}^3 \setminus \overline{B} \tag{A.6}$$

(where $k = \omega\sqrt{\varepsilon\mu}$) then each cartesian component E of $\mathbf{E}$ satisfies Helmholtz equation, i.e.,

$$\Delta E + k^2 E = 0 \quad \text{in } \mathbb{R}^3 \setminus \overline{B} \tag{A.7}$$

Given $A = (-1,1) \subset \mathbb{R}$, we define $v : A \times \mathbb{R}^3 \setminus \overline{B} \longrightarrow \mathbb{C}$ as $v(u,\mathbf{x}) = e^{ku}E(\mathbf{x})$, $\forall u \in A$ and $\forall \mathbf{x} \in \mathbb{R}^3 \setminus \overline{B}$. We note that E is locally square integrable over $\mathbb{R}^3 \setminus \overline{B}$ and then v is locally square integrable over $A \times \mathbb{R}^3 \setminus \overline{B}$.
Note that v satisfies $\Delta_{u,\mathbf{x}} v = 0$ in $A \times \mathbb{R}^3 \setminus \overline{B}$, where $\Delta_{u,\mathbf{x}} = \partial^2/\partial u^2 + \Delta_{\mathbf{x}}$.
Then v satisfies also the weak form of Laplace equation:

$$\int_{A\times\mathbb{R}^3\setminus\overline{B}} v\Delta\psi \, dxdy = 0 \quad \forall \psi \in C_0^\infty(A \times \mathbb{R}^3 \setminus \overline{B}) \tag{A.8}$$

From lemma A.3.1 (Weyl's lemma), v is analytic. Then also E is analytic on $\mathbb{R}^3 \setminus \overline{B}$ because

$$E(\mathbf{x}) = v(0,\mathbf{x}) \quad \forall \mathbf{x} \in \mathbb{R}^3 \setminus \overline{B} \tag{A.9}$$

Because E is an arbitrary cartesian component of $\mathbf{E}$ (or equivalently $\mathbf{e}$), each cartesian component of $\mathbf{E}$ (or equivalently $\mathbf{e}$) is analytic.

□

A.3 Useful Lemmas

It should be recalled that an analytic function is a function which can be locally expanded as a power series. Moreover, the set $C^\infty(\Omega)$ is defined as the set of infinitely differentiable functions with compact support in Ω.
Some useful lemmas that have been used in Section A.2 are now listed.

Lemma A.3.1 (Weyl's lemma: regularity of Laplace equation solutions)**.** *[91] Given a region $\Omega \subset \mathbb{R}^n$, if $v : \Omega \longrightarrow \mathbb{C}$ is locally square integrable over Ω and v satisfies*

$$\int_\Omega v \Delta \psi \, dx = 0 \quad \forall \psi \in C_0^\infty(\Omega) \tag{A.10}$$

then v is almost everywhere equal to a harmonic analytic function.

Lemma A.3.2 (Unique continuation of real-analytic functions)**.** *Let $V \subseteq \mathbb{R}^3$ a connected open set, $U \subseteq V$ an open (not empty) set and $f_1, f_2 : V \longrightarrow \mathbb{C}$ analytic functions such that $f_1|_U = f_2|_U$.*
Then $f_1 = f_2$ over V.

Proof. This is a well know result. A proof for the single-variable case can be found in corollary 1.2.6 of [92]. For the sake of completeness, a proof is here reported.
The function $g : V \longrightarrow \mathbb{C}$ as $g = f_1 - f_2$ over V is defined. The aim is to prove that $g = 0$ over V.
It should be noted that g is analytic on V.
The set Z is defined as the set where g and all its derivatives vanish, i.e.,

$$Z = \{\mathbf{x} \in V \text{ s.t. } D_{\mathbf{n}} g(\mathbf{x}) = 0 \text{ for all } \mathbf{n} \in \mathbb{N}^3\} = \bigcap_{\mathbf{n} \in \mathbb{N}^3} \{\mathbf{x} \in V \text{ s.t. } D_{\mathbf{n}} g(\mathbf{x}) = 0\} \tag{A.11}$$

where $|\mathbf{n}| = n_1 + n_2 + n_3$ and

$$D_{\mathbf{n}} = \frac{\partial^{|\mathbf{n}|}}{\partial x^{n_1} \partial y^{n_2} \partial z^{n_3}} \tag{A.12}$$

Aim of this part is to prove that Z is both open and closed.
The set Z is closed because Z is intersection of each closed set
$\{\mathbf{x} \in V \text{ s.t. } D_{\mathbf{n}} g(\mathbf{x}) = 0\}$. In fact, the latter set is closed because it is the inverse image of zero, i.e., it is $(D_{\mathbf{n}} g)^{-1}(\{0\})$ and $\{0\} \subset \mathbb{C}$ is closed and $D_{\mathbf{n}} g$ is continuous $\forall \mathbf{n} \in \mathbb{N}^3$.

The set Z is also open. Given an arbitrary point $\mathbf{x} \in Z$, there exist an open neighborhood $W_{\mathbf{x}} \subset Z$. In fact, given $\mathbf{x} \in Z$, g can be expanded as a Taylor series in $\mathbf{x}$. All coefficients of the series must be zero, then g and all its derivatives are zero on $W_{\mathbf{x}}$, i.e., $W_{\mathbf{x}} \subset Z$.
Finally, Z is a non-empty open and closed set, then $Z = V$. Hence, $g = 0$ and $f_1 = f_2$ over V. □

Appendix B

AUT Characterization through Equivalent Sources and Reciprocity

In Chapter 4 an inverse source NF-FF transformation has been applied to measured data using a UAV. The UAV operated in transmitting mode whereas the receiving voltage was acquired at the AUT. For this reason, reciprocity must be applied in order to characterize the AUT. In this Chapter, the application of the reciprocity theorem in its integral form (also known as Lorentz's lemma) is applied to the considered UAV-based measurement setup.

B.1 Reciprocity

In this Section, Lorentz's reciprocity lemma is briefly recalled. The case of an anisotropic medium is considered. The medium can be inhomogeneous and temporally dispersive (spatially dispersive media are not considered here). In this case, constitutive relations[1], i.e., equations linking the electric $\mathbf{D}$ and magnetic $\mathbf{B}$ inductions to the electric $\mathbf{E}$ and magnetic $\mathbf{H}$ fields, are $\mathbf{D} = \underline{\underline{\boldsymbol{\varepsilon}}} \cdot \mathbf{E}$ and $\mathbf{B} = \underline{\underline{\boldsymbol{\mu}}} \cdot \mathbf{H}$, , where $\underline{\underline{\boldsymbol{\varepsilon}}}$ and $\underline{\underline{\boldsymbol{\mu}}}$ are the electric permittivity and magnetic permeability tensors, respectively. If the medium is a conductor, the conduction current $\mathbf{J}_c = \underline{\underline{\boldsymbol{\sigma}}} \cdot \mathbf{E}$ must be taken into account, where $\underline{\underline{\boldsymbol{\sigma}}}$ is the conductivity tensor. In the free-space case, the electric permittivity, magnetic permeability and conductivity tensors become $\underline{\underline{\boldsymbol{\varepsilon}}} = \varepsilon \underline{\underline{\boldsymbol{I}}}$, $\underline{\underline{\boldsymbol{\mu}}} = \mu \underline{\underline{\boldsymbol{I}}}$ and $\underline{\underline{\boldsymbol{\sigma}}} = 0$, where ε and μ are the free-space electric permittivity and magnetic

[1] In this work, constitutive relations are considered in frequency domain.

permeability, respectively.
Reciprocity in its integral form is known as Lorentz's lemma which is based on the Gauss Theorem (Divergence theorem). For this reason, Gauss Theorem is here reported for completeness. The set $C^n(D,\mathbb{C}^3)$ is defined as the set of vector fields $\mathbf{E}: D \longrightarrow \mathbb{C}^3$ which are n-times continuously differentiable on D whereas $C^n(\overline{D},\mathbb{C}^3)$ is the set of vector fields $\mathbf{E} \in C^n(D,\mathbb{C}^3)$ which have continuous extensions (together with its derivatives of order n) to the closure $\overline{D}$ of D. For $n=0$, the notation $C(\overline{D},\mathbb{C}^3) = C^0(\overline{D},\mathbb{C}^3)$ is used. Similar definitions for $C^n(D)$ and $C^n(\overline{D})$ are understood for scalar functions $E: D \longrightarrow \mathbb{C}$.

Theorem B.1.1. *[90][Theorem of Gauss, Divergence Theorem] Consider a smooth bounded domain $D \subset \mathbb{R}^3$ with boundary ∂D with normal (outward pointing) unit vector* $\mathbf{n}$*, Consider a vector field $\mathbf{E} \in C(\overline{D},\mathbb{C}^3)$ with $\nabla \cdot \mathbf{E} \in C(D)$. Then*

$$\int_D \nabla \cdot \mathbf{E}\, dx = \int_{\partial D} \mathbf{E} \cdot \mathbf{n}\, ds \tag{B.1}$$

Proof. See Theorem A.11 in [90]. □

Lemma B.1.2 (Lorentz's lemma)**.** *(from (1.10) in [93]) Consider a smooth bounded domain $D \subseteq \mathbb{R}^3$ with boundary ∂D with normal (outward pointing) unit vector* $\mathbf{n}$*. The domain D can be constituted by a union of M disjoint subdomains D_m, i.e., open sets $D_m \subset D$ for $m = 1,...,M$ such that $\overline{D} = \cup_{m=1}^{M} \overline{D}_m$.*
Consider an electromagnetic field $(\mathbf{E}_n, \mathbf{H}_n)$ with sources $(\mathbf{J}_n, \mathbf{M}_n)$ solution of Maxwell's equations on $\cup_{m=1}^{M} D_m$, i.e.,

$$\begin{cases} \nabla \times \mathbf{E}_n = -j\omega \underline{\underline{\boldsymbol{\mu}}}_n \cdot \mathbf{H}_n - \mathbf{M}_n \\ \nabla \times \mathbf{H}_n = j\omega \underline{\underline{\tilde{\boldsymbol{\varepsilon}}}}_n \cdot \mathbf{E}_n + \mathbf{J}_n \\ \text{on } D_m \quad \forall m = 1,...,M \end{cases} \tag{B.2}$$

where $\underline{\underline{\tilde{\boldsymbol{\varepsilon}}}}_n(\mathbf{r}) = \underline{\underline{\boldsymbol{\varepsilon}}}_n(\mathbf{r}) - \frac{j}{\omega}\underline{\underline{\boldsymbol{\sigma}}}_n(\mathbf{r})$, for $n = 1,2$.
Sources $\mathbf{J}_n, \mathbf{M}_n$ and tensors $\underline{\underline{\tilde{\boldsymbol{\varepsilon}}}}_n, \underline{\underline{\boldsymbol{\mu}}}_n$ are assumed to be sufficiently smooth such that fields $\mathbf{E}_n, \mathbf{H}_n$ solutions of (B.2) satisfy hypotheses of theorem B.1.1 on each subdomain $\overline{D}_m$ for all $m = 1,...,M$ and $n = 1,2$. Furthermore, assume that the tangential fields $\mathbf{n} \times \mathbf{E}$ and $\mathbf{n} \times \mathbf{H}$ are continuous across the subdomains D_m for both fields

$n = 1$ and $n = 2$. Then

$$\int_D (\mathbf{J}_1 \cdot \mathbf{E}_2 - \mathbf{M}_1 \cdot \mathbf{H}_2) dx - \int_D (\mathbf{J}_2 \cdot \mathbf{E}_1 - \mathbf{M}_2 \cdot \mathbf{H}_1) dx +$$
$$+ j\omega \int_D \mathbf{H}_1 \cdot \left(\underline{\underline{\boldsymbol{\mu}}}_2 - \underline{\underline{\boldsymbol{\mu}}}_1^T \right) \cdot \mathbf{H}_2 \, dx - j\omega \int_D \mathbf{E}_1 \cdot \left(\underline{\underline{\tilde{\boldsymbol{\varepsilon}}}}_2 - \underline{\underline{\tilde{\boldsymbol{\varepsilon}}}}_1^T \right) \cdot \mathbf{E}_2 \, dx =$$
$$= \int_{\partial D} (\mathbf{E}_1 \times \mathbf{H}_2 - \mathbf{E}_2 \times \mathbf{H}_1) \cdot \mathbf{n} \quad ds$$

Proof. The proof can be found in [93] and it is based on the Gauss divergence theorem (see theorem (B.1.1)) applied on each subdomain D_m and manipulations of (B.2). □

It should be noted that in lemma (B.1.2) the tangential fields $\mathbf{n} \times \mathbf{E}$ and $\mathbf{n} \times \mathbf{H}$ are continuous across the subdomains D_m if no surface currents are present between the subdomains (where $\mathbf{n}$ is the unit normal vector on the surface across two neighbour subdomains).
In the next part, well-known corollaries useful for the application of the reciprocity are reported.

Corollary B.1.3. *Consider the same hypoteses of Lorentz's lemma B.1.2 in free-space. Consider the surface $\partial D = S^2(R)$, where $S^2(R) = \{\mathbf{x} \in \mathbb{R}^3 \text{ s.t. } |\mathbf{x}| = R\}$ is the sphere of radius R centered at the origin. Furthermore, assume that fields $\mathbf{E}_1, \mathbf{H}_1$ and $\mathbf{E}_2, \mathbf{H}_2$ satisfy the Silver-Muller radiation condition at infinity:*

$$\mathbf{E}_1(\mathbf{x}) - Z_0 \mathbf{H}_1(\mathbf{x}) \times \frac{\mathbf{x}}{|\mathbf{x}|} = O(\frac{1}{|\mathbf{x}|^2}) \qquad |\mathbf{x}| \to +\infty \tag{B.3}$$

$$\mathbf{E}_2(\mathbf{x}) - Z_0 \mathbf{H}_2(\mathbf{x}) \times \frac{\mathbf{x}}{|\mathbf{x}|} = O(\frac{1}{|\mathbf{x}|^2}) \qquad |\mathbf{x}| \to +\infty \tag{B.4}$$

uniformly for $\mathbf{x}/|\mathbf{x}| \in S^2$, where $Z_0 = \sqrt{\mu_0/\varepsilon_0}$ is the free space impedance. Then, the following surface integral tends to zero:

$$\lim_{R \to +\infty} \int_{S^2(R)} (\mathbf{E}_1 \times \mathbf{H}_2 - \mathbf{E}_2 \times \mathbf{H}_1) \cdot \mathbf{n} \quad ds = 0 \tag{B.5}$$

Proof. It can be proven using the Silver-Muller radiation condition and the property that

$$\lim_{R \to +\infty} \int_{S^2(R)} O(\frac{1}{|\mathbf{x}|^3}) \quad ds = 0 \tag{B.6}$$

□

Corollary B.1.4. *Consider the same hypoteses of Lorentz's lemma B.1.2. Consider a surface Σ_c and consider the unit normal vector $\mathbf{n}$ to the surface Σ_c. Assuming that Σ_c is the surface of a Perfect Electric Conductor (PEC), i.e. assuming vanishing tangential electric fields $\mathbf{E}_1 \times \mathbf{n} = \mathbf{E}_2 \times \mathbf{n} = 0$ on Σ_c, the following integral is equal to zero:*

$$\int_{\Sigma_c} (\mathbf{E}_1 \times \mathbf{H}_2 - \mathbf{E}_2 \times \mathbf{H}_1) \cdot \mathbf{n} \quad ds = 0 \tag{B.7}$$

Proof. It can be proven using the PEC condition of vanishing tangential electric field. □

Corollary B.1.5 (Lorentz's lemma in free space)**.** *Consider two bounded disjoint smooth domains V_1 and V_2 with normal (outward pointing) unit vector $\mathbf{n}$. Consider an electromagnetic field $(\mathbf{E}_n, \mathbf{H}_n)$ solutions of Maxwell's equations*

$$\begin{cases} \nabla \times \mathbf{E}_n = -j\omega\mu\mathbf{H}_n \\ \nabla \times \mathbf{H}_n = j\omega\varepsilon\mathbf{E}_n \\ \text{on } \mathbb{R}^3 \setminus (V_1 \cup V_2) \\ \text{Silver-Muller radiation condition} \end{cases} \tag{B.8}$$

Then

$$\int_{\partial V_1 \cup \partial V_2} (\mathbf{E}_1 \times \mathbf{H}_2 - \mathbf{E}_2 \times \mathbf{H}_1) \cdot \mathbf{n} \quad ds = 0$$

If $\mathbf{n} \times \mathbf{E}_1 = 0$ on ∂V_1 and $\mathbf{n} \times \mathbf{E}_2 = 0$ on ∂V_2, then

$$\int_{\partial V_1} (\mathbf{n} \times \mathbf{H}_1) \cdot \mathbf{E}_2 \quad ds = \int_{\partial V_2} (\mathbf{n} \times \mathbf{H}_2) \cdot \mathbf{E}_1 \quad ds$$

where the tangential magnetic fiels are sometimes denoted with $\mathbf{J}_{s,1} = \mathbf{n} \times \mathbf{H}_1$ and $\mathbf{J}_{s,2} = \mathbf{n} \times \mathbf{H}_2$.

Proof. It can be proven from lemma B.1.2 in case of free-space. □

B.2 Single Antenna

In this section, the reciprocity theorem (Lorentz's lemma (B.1.2)) is applied to the case of UAV-based antenna measurement of an AUT. Firstly, the simpler case of a single antenna (not an antenna array) is analyzed. Choices of fields $\mathbf{E}_1, \mathbf{H}_1$ and $\mathbf{E}_2, \mathbf{H}_2$ in lemma B.1.2 are analyzed and specified.

Choice of Fields/Sources 1

The electromagnetic field $\mathbf{E}_1, \mathbf{H}_1$ is chosen as the field of the AUT in transmitting (TX) mode with the UAV which is not present. This is the unknown field that has to be determined from measurements. This field is produced by unknown currents $\mathbf{J}_1$ and $\mathbf{M}_1$ at the transmitter level (see Fig. B.1, left part). In lemma (B.2.1) (single antenna case) and lemma (B.3.1) (array case) the field $\mathbf{E}_1$ is assumed to be equivalently produced by an electric current $\mathbf{J}_1^0$ radiating in free-space and defined over the AUT surface (see Fig. B.1, right part).

Choice of Fields/Sources 2

The electromagnetic field $\mathbf{E}_2, \mathbf{H}_2$ is chosen as the field of the UAV in TX mode, in presence of the receiving antenna, i.e., the AUT. The equivalence theorem (Love's version) on the volume of the UAV (denoted with V_{uav}) is applied. This step allows to cancel the presence of the UAV, considering free-space in the UAV volume V_{uav}. In this way, the AUT field $\mathbf{E}_1$ which propagates in free-space (without the UAV structure) can be retrieved (see proof of lemma B.2.1). This can be done because $\mathbf{J}_1$ and $\mathbf{J}_2$ radiate in the same medium, i.e., in presence of the AUT (see Table B.1, left part). Similarly, $\mathbf{J}_1^0$ and $\mathbf{J}_2^0$ radiate in the same medium, i.e., free-space.
For simplicity, the surface $S_{uav} = \partial V_{uav}$ of the UAV is assumed to be a Perfect Electric Conductor (PEC) [2] such that the electric field produced by the UAV-mounted antenna is given by the electric current $\mathbf{J}_2 = (\mathbf{n} \times \mathbf{H}_2)\delta_{S_{uav}} = \mathbf{J}_{s,2}\delta_{S_{uav}}$ over the UAV surface S_{uav}, where $\mathbf{J}_{s,2} = \mathbf{n} \times \mathbf{H}_2$ and $\delta_{S_{uav}}$ is a surface Dirac delta over S_{uav}. The current $\mathbf{J}_2$ radiates a null electromagnetic field in V_{uav}, i.e., $\mathbf{E}_2(\mathbf{r}) = \mathbf{H}_2(\mathbf{r}) = 0$ for $\mathbf{r} \in V_{uav}$. In the next part, $\mathbf{J}_2$ will be approximated with the current $\mathbf{J}_2^0$, i.e., $\mathbf{J}_2 \simeq \mathbf{J}_2^0$, where

[2] we consider the case where the field on the UAV is completely described by an electric current (no magnetic current).

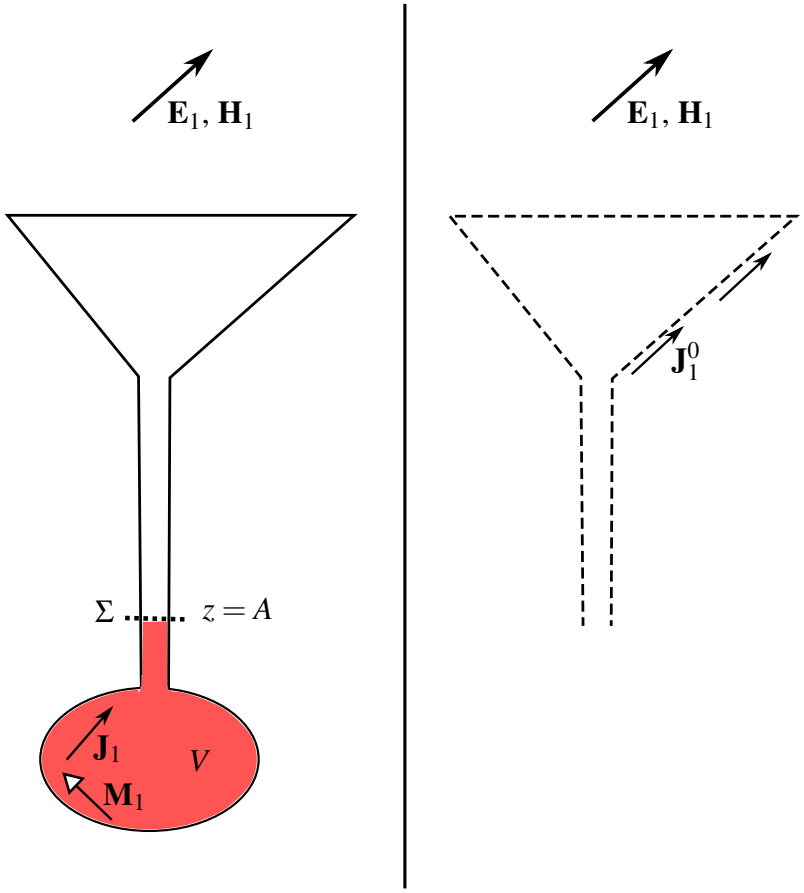

Fig. B.1 The AUT produces an electromagnetic field $\mathbf{E}_1$ and $\mathbf{H}_1$ in transmitting mode. On the left: the transmitter is placed in the volume V (where possible sources $\mathbf{J}_1$ and $\mathbf{M}_1$ are present) highlighted in red (see proof of lemma B.2.1). In V, sources $\mathbf{J}_1$ and $\mathbf{M}_1$ produces fields $\mathbf{E}_1$ and $\mathbf{H}_1$ in presence of the AUT structure. On the right: fields $\mathbf{E}_1$ and $\mathbf{H}_1$ are produced by an electric current $\mathbf{J}_1^0$ defined over the AUT surface S_{AUT} radiating in free-space.

$\mathbf{J}_2^0$ is the current defined over the UAV surface and radiating in free-space, i.e., in absence of the AUT (see Table B.1, right part). The tangential magnetic field is hence approximated with $\mathbf{J}_{s,2}^0 \simeq \mathbf{n} \times \mathbf{H}_2$. This assunption is fulfilled if the mutual coupling between AUT and UAV can be neglected. Finally, the incident electromagnetic field produced by the UAV i.e., produced by the current $\mathbf{J}_{s,2}^0$, is denoted with $\mathbf{E}_2^0$, $\mathbf{H}_2^0$.

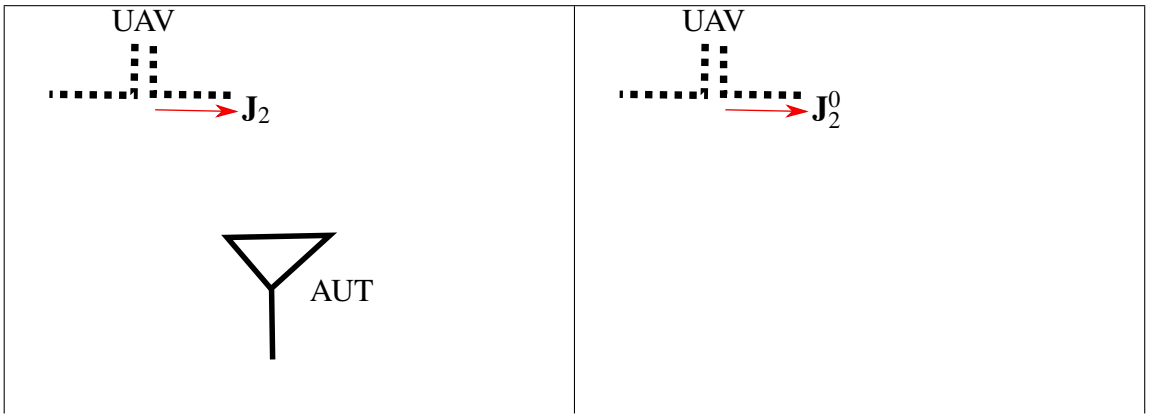

Table B.1 On the left: UAV and AUT. The current $\mathbf{J}_2$ radiates in presence of the AUT structure (in the UAV volume V_{uav} free-space can be placed using the equivalence theorem). On the right: the current $\mathbf{J}_2^0 \simeq \mathbf{J}_2$ radiates in free-space (the AUT is not present).

B.2.1 J on AUT Surface

In this Section reciprocity for a single antenna (not an antenna array) is analyzed. The AUT field $\mathbf{E}_1$ is assumed to be completely described by an electric current $\mathbf{J}_1$ defined over the AUT surface S_{AUT}. Equivalent currents placed over a virtual surface enclosing the AUT will be considered in next Section.

Lemma B.2.1. *Consider the previous assumptions on fields* $\mathbf{E}_1, \mathbf{H}_1$ *and* $\mathbf{E}_2, \mathbf{H}_2$. *Then*

$$c\left[\frac{Z_A}{Z_{RX}}+1\right] I_{TX} V_{RX} = -\int_{S_{uav}} \mathbf{J}_{s,2}^0 \cdot \mathbf{E}_1 dx = -\int_{S_{AUT}} \mathbf{J}_{s,1}^0 \cdot \mathbf{E}_2^0 dx \quad \text{(B.9)}$$

Proof. A reference surface Σ separating the AUT from the transmitter is considered (see Fig. B.2). The volume occupied by the transmitter is denoted with V, see Fig. B.2. It should be noted that V must contain the Low Noise Amplifier (LNA) of the antenna and all other non-reciprocal components. Lorentz's lemma B.1.2 is applied over the volume[3] $D = \mathbb{R}^3 \setminus V$.

The right-hand-side of Lorentz's lemma: This surface integral has to be considered:

$$\int_{\partial V} (\mathbf{E}_1 \times \mathbf{H}_2 - \mathbf{E}_2 \times \mathbf{H}_1) \cdot \mathbf{n} \quad ds \quad \text{(B.10)}$$

[3] more rigorously, we have to apply Lorentz's lemma over a finite volume contained in a sphere of radius R and then, for $R \to +\infty$, the surface integral over $S^2(R)$ tends to zero for corollary B.1.3.

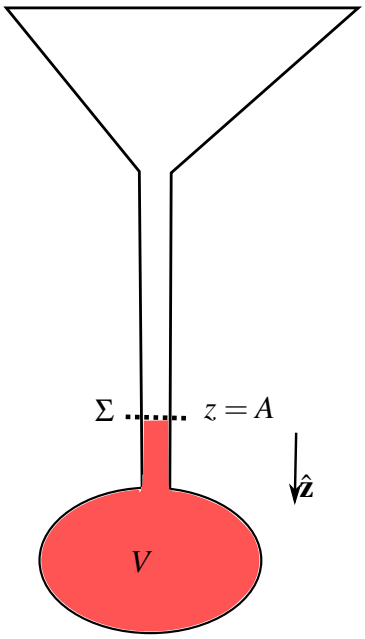

Fig. B.2 The AUT and the volume V considered for the reciprocity (highlighted in red).

Note that because $\partial V = \Sigma_c \cup \Sigma$. The surface Σ_c (i.e., the surface of the transmitter part) is modeled as a PEC. Then

$$\int_{\partial V} = \int_{\Sigma_c} + \int_{\Sigma} = \int_{\Sigma} \tag{B.11}$$

where the integral $\int_{\Sigma_c} = 0$ vanishes for corollary B.1.4. It should be noted that the normal component of fields in the integral over Σ vanishes because, writing each field then:

$$\mathbf{E}_i \times \mathbf{H}_j = (\mathbf{E}_i^t + E_i^n \mathbf{n}) \times (\mathbf{H}_j^t + H_j^n \mathbf{n}) = \mathbf{E}_i^t \times \mathbf{H}_j^t + H_j^n \mathbf{E}_i^t \times \mathbf{n} + E_i^n \mathbf{n} \times \mathbf{H}_j^t$$

where each field $\mathbf{E}_i$ has ben written as a sum of a transverse $\mathbf{E}_i^t$ and a normal $E_i^n \mathbf{n}$ part, i.e., $\mathbf{E}_i = \mathbf{E}_i^t + E_i^n \mathbf{n}$ for $i = 1, 2$, $i \neq j$. Using a scalar product for $\mathbf{n}$ and $\mathbf{n} \cdot (\mathbf{a} \times \mathbf{n}) = 0$ $\forall \mathbf{a}$, next equation is obtained:

$$\mathbf{n} \cdot (\mathbf{E}_i \times \mathbf{H}_j) = \mathbf{n} \cdot (\mathbf{E}_i^t \times \mathbf{H}_j^t) \tag{B.12}$$

The surface integral (B.10) is then

$$\int_{\partial V}(\mathbf{E}_1\times\mathbf{H}_2-\mathbf{E}_2\times\mathbf{H}_1)\cdot\mathbf{n}\quad ds=\int_{\Sigma}(\mathbf{E}_1^t\times\mathbf{H}_2^t-\mathbf{E}_2^t\times\mathbf{H}_1^t)\cdot\mathbf{n}\quad ds=\oslash$$

where the symbol $\oslash$ denotes that all the computations refer to the same quantity, i.e., the surface integral in (B.10).
Consider the z axis as the longitudinal axis along the cable connecting AUT and transmitter whereas x,y axis are the transverse axis. A reference plane at $z=A$ is chosen. If the cable is single-mode and is sufficiently long, then fields can be approximated with only one propagating mode. Then [4] (see Fig. B.3, B.4 for the equivalent circuit of the AUT in receiving and transmitting mode)

$$\begin{cases}\mathbf{E}_1^t(x,y,z=A)=V_{TX}\mathbf{e}(x,y)\\ \mathbf{H}_1^t(x,y,z=A)=-I_{TX}\mathbf{h}(x,y)\end{cases}\qquad\begin{cases}\mathbf{E}_2^t(x,y,z=A)=V_{RX}\mathbf{e}(x,y)\\ \mathbf{H}_2^t(x,y,z=A)=I_{RX}\mathbf{h}(x,y)\end{cases}\tag{B.13}$$

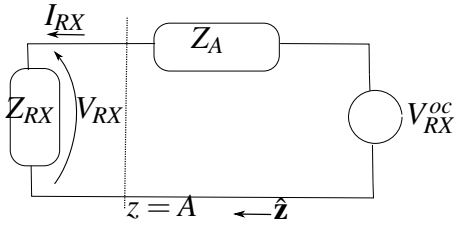

Fig. B.3 Circuit of AUT in receiving (RX) mode with Thevenin equivalent circuit of the antenna and incident field.

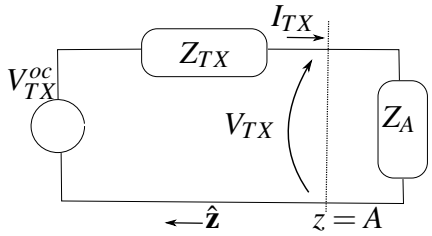

Fig. B.4 Circuit of AUT in TX with Thevenin equivalent circuit of the transmitter.

The surface integral becomes

$$\oslash=\Big[V_{TX}I_{RX}+V_{RX}I_{TX}\Big]\int_{\Sigma}(\mathbf{e}\times\mathbf{h})\cdot\mathbf{n}\quad ds=c\Big[V_{TX}I_{RX}+V_{RX}I_{TX}\Big]=\oslash$$

[4] note the minus sign at I_{TX} for the choice of z axis.

where $c := \int_\Sigma (\mathbf{e} \times \mathbf{h}) \cdot \mathbf{n} \quad ds$ is a dimensionless constant.
In receiving mode, the receiver is seen as a load with impedance Z_{RX}. The receiving voltage (see Fig. B.3) V_{RX} and current I_{RX} are linked by $V_{RX} = Z_{RX} I_{RX}$. On the contrary, in transmitting mode (see Fig. B.4), the voltage V_{TX} and the current I_{TX} at section Σ are linked by $V_{TX} = Z_A I_{TX}$.
In conclusion, the right hand side of Lorentz's lemma is:

$$\int_{\partial V} (\mathbf{E}_1 \times \mathbf{H}_2 - \mathbf{E}_2 \times \mathbf{H}_1) \cdot \mathbf{n} \quad ds = c I_{TX} V_{RX} \left[\frac{Z_A}{Z_{RX}} + 1 \right]$$

The left-hand-side of Lorentz's lemma: The left-hand-side of Lorentz's lemma is

$$\int_D (\mathbf{J}_1 \cdot \mathbf{E}_2 - \mathbf{M}_1 \cdot \mathbf{H}_2) dx - \int_D (\mathbf{J}_2 \cdot \mathbf{E}_1 - \mathbf{M}_2 \cdot \mathbf{H}_1) dx +$$
$$+ j\omega \int_D \mathbf{H}_1 \cdot \left(\underline{\underline{\boldsymbol{\mu}}}_2 - \underline{\underline{\boldsymbol{\mu}}}_1^T \right) \cdot \mathbf{H}_2 \, dx - j\omega \int_D \mathbf{E}_1 \cdot \left(\underline{\underline{\tilde{\boldsymbol{\varepsilon}}}}_2 - \underline{\underline{\tilde{\boldsymbol{\varepsilon}}}}_1^T \right) \cdot \mathbf{E}_2 \, dx = \boxplus$$

where the symbol $\boxplus$ denotes that all the computations refer to the volume integral in the left-hand-side of Lorentz's lemma.
In $D = \mathbb{R}^3 \setminus V$, there are no sources for fields 1, i.e. $\mathbf{J}_1 = \mathbf{M}_1 = 0$ in D. Furthermore, the medium in D is the same for both fields 1 and 2 and is also reciprocal (note that the LNA has been included inside V), i.e.:

$$\begin{cases} \underline{\underline{\tilde{\boldsymbol{\varepsilon}}}}_1(\mathbf{r}) = \underline{\underline{\tilde{\boldsymbol{\varepsilon}}}}_1^T(\mathbf{r}) = \underline{\underline{\tilde{\boldsymbol{\varepsilon}}}}_2(\mathbf{r}) = \underline{\underline{\tilde{\boldsymbol{\varepsilon}}}}_2^T(\mathbf{r}) \\ \underline{\underline{\boldsymbol{\mu}}}_1(\mathbf{r}) = \underline{\underline{\boldsymbol{\mu}}}_1^T(\mathbf{r}) = \underline{\underline{\boldsymbol{\mu}}}_2(\mathbf{r}) = \underline{\underline{\boldsymbol{\mu}}}_2^T(\mathbf{r}) \end{cases} \tag{B.14}$$

$\forall \mathbf{r} \in D$. Then, the left-hand-side of Lorentz's lemma reduces to:

$$\boxplus = -\int_D \mathbf{J}_2 \cdot \mathbf{E}_1 dx = \boxplus \tag{B.15}$$

Note that $\mathbf{J}_2$ is the current over the UAV in presence of the AUT. The current $\mathbf{J}_2$ could be computed from simulations. However, the computation of $\mathbf{E}_1$ would be prohibitive for the time-cost. Because the UAV in practical applications is several wavelengths far from the AUT, the mutual coupling between AUT and UAV can be neglected. More precisely, the current $\mathbf{J}_2$ is approximated with $\mathbf{J}_2^0$ where $\mathbf{J}_2^0$ is the current over the UAV in free space (in absence of the AUT). Hence

$$\boxplus = -\int_{V_{uav}} \mathbf{J}_2 \cdot \mathbf{E}_1 \quad dx = -\int_{S_{uav}} \mathbf{J}_{s,2} \cdot \mathbf{E}_1 \quad ds = -\int_{S_{uav}} \mathbf{J}_{s,2}^0 \cdot \mathbf{E}_1 \quad ds = \boxplus \tag{B.16}$$

The field $\mathbf{E}_1$ is assumed to be produced by an electric current only [5] radiating in free space. In this way, standard reciprocity (see corollary B.1.5) can be applied [6]:

$$\int_{S_{uav}} \mathbf{J}^0_{s,2} \cdot \mathbf{E}_1 dx = \int_{S_{AUT}} \mathbf{J}^0_{s,1} \cdot \mathbf{E}^0_2 dx \tag{B.17}$$

where $\mathbf{E}^0_2$ is the incident field produced by the UAV in free-space, i.e., $\mathbf{E}^0_2$ is the field radiated by $\mathbf{J}^0_2$.
Matching right and left hand side, the result is proved. □

Comparison with Similar Equations in Literature

Because (see Fig. B.3)

$$V_{RX} = \frac{Z_{RX}}{Z_A + Z_{RX}} V^{oc}_{RX} \tag{B.18}$$

then equation (B.9) can be written as

$$cI_{TX}V^{oc}_{RX} = -\int_{V_{uav}} \mathbf{J}^0_2 \cdot \mathbf{E}_1 dx = -\int_{V_{AUT}} \mathbf{J}_1 \cdot \mathbf{E}^{inc}_2 dx \tag{B.19}$$

Enforcing $c = 1$, the previous equation is in line with similar results in literature [70], [94] [7], [95][8].

V_{RX} is not the Actual Measured Voltage

As a last remark, V_{RX} is the voltage before the LNA, hence it is not the actual measured voltage. The LNA and its scattering matrix must be taken into account to obtain a more accurate model.

B.2.2 J and M on Equivalent Surface

In this part, reciprocity with equivalent sources over the virtual surface enclosing the AUT is considered.

[5] We consider the case where the field of the AUT is completely described by an electric current (no magnetic current).
[6] because $\mathbf{J}^0_{s,2} \simeq \mathbf{n} \times \mathbf{H}_2$ and $\mathbf{J}^0_{s,1} \simeq \mathbf{E}_1 \times \mathbf{n}$
[7] there is a minus sign w.r.t. our equation
[8] there is a minus sign w.r.t. our equation

Lemma B.2.2. *Consider the assumptions of this section on* $\mathbf{E}_1, \mathbf{H}_1$ *and* $\mathbf{E}_2, \mathbf{H}_2$. *Then*

$$c\left[\frac{Z_A}{Z_{RX}}+1\right] I_{TX} V_{RX} = -\int_{S_{uav}} \mathbf{J}^0_{s,2}\cdot\mathbf{E}_1 dx = -\int_S \mathbf{J}^0_{s,1}\cdot\mathbf{E}^0_2 - \mathbf{M}^0_{s,1}\cdot\mathbf{H}^0_2 ds \tag{B.20}$$

Proof. The proof of lemma B.2.1 is almost valid. More precisely, only the part after equation (B.17) has to be modified. A closed surface S enclosing the AUT is considered. Equivalent sources $\mathbf{J}^0_1 = \mathbf{J}^0_{s,1}\delta_S$ and $\mathbf{M}^0_1 = \mathbf{M}^0_{s,1}\delta_S$ with $\mathbf{J}^0_{s,1} = \mathbf{n}\times\mathbf{H}_1$ and $\mathbf{M}^0_{s,1} = \mathbf{E}_1\times\mathbf{n}$ are placed over S, where $\mathbf{n}$ is the unit outward directed normal vector of S (see Fig. B.5). Sources $\mathbf{J}^0_{s,1}$ and $\mathbf{M}^0_{s,1}$ radiate a null field inside S and radiate $\mathbf{E}_1, \mathbf{H}_1$ outside S. Applying lemma (B.1.5), next equation is obtanied

$$\int_{V_{uav}} \mathbf{J}^0_2\cdot\mathbf{E}_1 dx = \int_S \mathbf{J}_{s,1}\cdot\mathbf{E}^{inc}_2 - \mathbf{M}_{s,1}\cdot\mathbf{H}^{inc}_2 ds \tag{B.21}$$

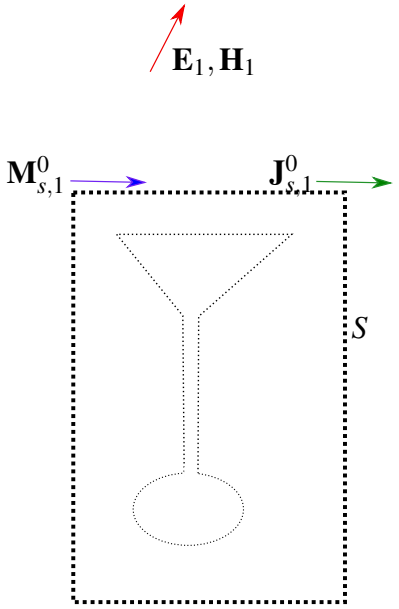

Fig. B.5 The equivalent virtual surface S encloses the AUT. Over S, currents $\mathbf{J}^0_{s,1}$ and $\mathbf{M}^0_{s,1}$ are defined. These currents radiate an electromagnetic field $\mathbf{E}_1, \mathbf{H}_1$ (i.e. the field produced by the AUT) outside S.

□

B.3 Array

In this Section, reciprocity for an antenna array is analyzed. Definitions of quantities used in this Section are here reported.

- $\mathbf{E}_1, \mathbf{H}_1$ is the electromagnetic field of the array in TX mode.
- S_{aut} is the union of the surfaces of all array elements.
- S is a virtual surface enclosing the array. On S, equivalent (Love's version) currents $\mathbf{J}_{s,1}$ and $\mathbf{M}_{s,1}$ are defined. These currents radiate in free space an eletromagnetic field $\mathbf{E}_1, \mathbf{H}_1$ which is the field of the array in TX mode.
- $\mathbf{I}_{TX}$ is the vector containing input currents when the array is in TX mode (see Fig. B.7). The vector $\mathbf{I}_{TX}^T$ denotes its transpose.
- $\mathbf{V}_{RX}$ is the vector containing receiving (measured) voltages when the array is in RX mode, with the UAV in TX mode.
- $\mathbf{Z}_A$ is the impedance matrix of the array.
- $\mathbf{Z}_{RX}$ is a diagonal matrix with load impedances of the array (in RX mode) on the diagonal.
- $\mathbf{I}$ is the identity matrix.

As in the previous Section, S_{uav} is the UAV surface and $\mathbf{J}_{s,2}$ is the electric current over S_{uav} radiating in presence of the array. Then $\mathbf{J}_{s,2}^0$ is the electric current over S_{uav} radiating in free-space fields $\mathbf{E}_2^0, \mathbf{H}_2^0$.

B.3.1 J on AUT Surface

Lemma B.3.1. *Consider the assumptions of this chapter on* $\mathbf{E}_1, \mathbf{H}_1$ *and* $\mathbf{E}_2, \mathbf{H}_2$. *Then*

$$c\mathbf{I}_{TX}^T \left[\mathbf{Z}_A \mathbf{Z}_{RX}^{-1} + \mathbf{I}\right] \mathbf{V}_{RX} = -\int_{S_{uav}} \mathbf{J}_{s,2}^0 \cdot \mathbf{E}_1^0 \, dx = -\int_{S_{aut}} \mathbf{J}_1^0 \cdot \mathbf{E}_2^0 \, dx \tag{B.22}$$

Proof. A reference surface Σ_n, separating the $n-$th antenna from the TX, is considered (see Fig. B.6). The volume V_n is the volume occupied by the TX at antenna number n. Lorentz's lemma B.1.2 is applied over the volume $D = \mathbb{R}^3 \setminus V$ where $V = V_1 \cup V_2 \cup .... \cup V_{N_{ant}}$.

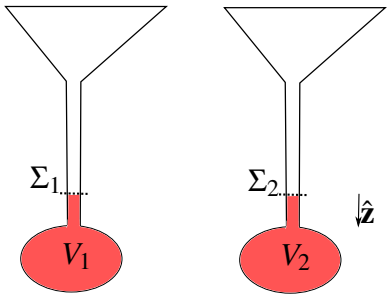

Fig. B.6 Example with $N_{ant} = 2$. Considered volumes V_1 and V_2 for reciprocity.

The right-hand-side of Lorentz's lemma: the next surface integral has to be considered:

$$\int_{\partial V} (\mathbf{E}_1 \times \mathbf{H}_2 - \mathbf{E}_2 \times \mathbf{H}_1) \cdot \mathbf{n} \quad ds = \sum_{n=1}^{N_{ant}} \int_{\Sigma_n} (\mathbf{E}_1 \times \mathbf{H}_2 - \mathbf{E}_2 \times \mathbf{H}_1) \cdot \mathbf{n} \quad ds = \tag{B.23}$$

$$= \sum_{n=1}^{N_{ant}} c_n \left(V_{TX}^n I_{RX}^n + V_{RX}^n I_{TX}^n \right) = \oslash \tag{B.24}$$

where the index n refers to the $n-$th antenna. If all cables are equal then all sections Σ_n coincide and then $c_n = c = \int_\Sigma (\mathbf{e} \times \mathbf{h}) \cdot \mathbf{n} \, ds$ is constant $\forall n = 1, ..., N_{ant}$. Because $V_{RX}^n = Z_{RX}^n I_{RX}^n \ \forall n = 1, ..., N_{ant}$ (see Fig. B.7) and $\mathbf{V}_{TX} = \mathbf{Z}_A \mathbf{I}_{TX}$, next equation is obtained

$$\oslash = c \sum_{n=1}^{N_{ant}} \left(V_{TX}^n I_{RX}^n + V_{RX}^n I_{TX}^n \right) = c \mathbf{V}_{RX}^T \left[\mathbf{Z}_{RX}^{-1} \mathbf{Z}_A + \mathbf{I} \right] \mathbf{I}_{TX} \tag{B.25}$$

Taking the transpose, using that $\mathbf{Z}_{RX}$ is diagonal and $\mathbf{Z}_A = \mathbf{Z}_A^T$ is symmetric, once obtains

$$\mathbf{V}_{RX}^T \left[\mathbf{Z}_{RX}^{-1} \mathbf{Z}_A + \mathbf{I} \right] \mathbf{I}_{TX} = \mathbf{I}_{TX}^T \left[\mathbf{Z}_A \mathbf{Z}_{RX}^{-1} + \mathbf{I} \right] \mathbf{V}_{RX} \tag{B.26}$$

The right-hand-side of Lorentz's lemma: see the proof for the single antenna case, i.e., proof of lemma B.2.1. □

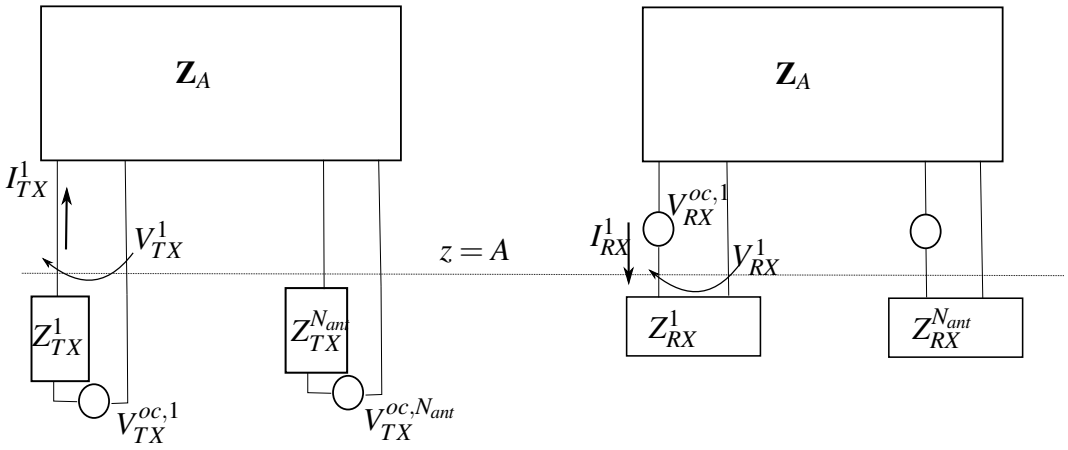

Fig. B.7 On the left: array in transmitting mode. For each element, the Thevenin equivalent of the generator is considered (for the n-th element, an impedance Z_{TX}^n with open circuit voltage $V_{TX}^{oc,n}$ are considered). On the right: array in receiving mode. The horizontal line is the section $z = A$.

B.3.2 J and M on Equivalent Surface

Lemma B.3.2. *Consider the assumptions of this section on* $\mathbf{E}_1, \mathbf{H}_1$ *and* $\mathbf{E}_2, \mathbf{H}_2$. *Then*

$$c\mathbf{I}_{TX}^T \left[\mathbf{Z}_A \mathbf{Z}_{RX}^{-1} + \mathbf{I} \right] \mathbf{V}_{RX} = -\int_{V_{uav}} \mathbf{J}_2^0 \cdot \mathbf{E}_1 dx = -\int_S \mathbf{J}_{s,1}^0 \cdot \mathbf{E}_2^0 - \mathbf{M}_{s,1}^0 \cdot \mathbf{H}_2^0 ds \tag{B.27}$$

Proof. For the right-hand-side of Lorentz's lemma, see the proof of lemma B.3.1. For the right-hand-side of Lorentz's lemma, see the proof for the single antenna case with equivalent sources, i.e., lemma B.2.2 and Fig. B.8. □

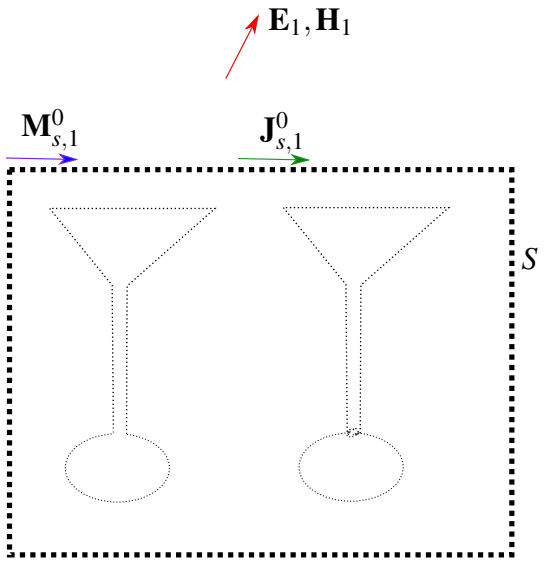

Fig. B.8 Example with $N_{ant} = 2$. Equivalent currents $\mathbf{J}^0_{s,1}$ and $\mathbf{M}^0_{s,1}$ radiate the same field $\mathbf{E}_1$ of the array in TX mode outside S.

B.4 Inverse Source NF-FF Transformation: theoretical implementation

In this Section, reciprocity lemma (B.3.1) is analyzed for the application of the inverse source NF-FF transformation. Dividing the result of lemma (B.3.1) for the source voltage $V_s = I_s Z_s$, next equation is obtained

$$c\mathbf{I}_{TX}^T \left[\mathbf{Z}_A \mathbf{Z}_{RX}^{-1} + \mathbf{I}\right] \frac{\mathbf{V}_{RX}}{V_s} = -\frac{1}{Z_s} \int_{V_{uav}} \frac{\mathbf{J}_2^0}{I_s} \cdot \mathbf{E}_1 dV \tag{B.28}$$

Assuming that the UAV-mounted dipole can be approximated as an elementary dipole at location $\mathbf{r}$ then

$$\mathbf{J}_2^0(\mathbf{y}) = I_s L \hat{\mathbf{u}}(\mathbf{r})\, \delta(\mathbf{r} - \mathbf{y}) \tag{B.29}$$

where L is a constant with unit of length and $\hat{\mathbf{u}}$ is the unit vector which represents the direction of the dipole over the UAV. All array elements are assumed to be loaded on the same impedance, i.e., $\mathbf{Z}_{RX} = Z_{RX}\mathbf{I}$. Furthermore, all elements are assumed to be equal and de-coupled i.e. $\mathbf{Z}_A = Z_A\mathbf{I}$. If the $n-$th array element is excited with a

current I_{TX}, i.e., $(\mathbf{I}_{TX})_m = I_{TX}\delta_{mn}$ [9], substituting (B.29) in (B.28), next equation is obtained

$$cI_{TX}\left[\frac{Z_A}{Z_{RX}}+1\right]\frac{V_{RX,n}(\mathbf{r})}{V_s} = -\frac{L}{Z_s}\hat{\mathbf{u}}(\mathbf{r})\cdot\mathbf{E}_1(\mathbf{r}) \tag{B.30}$$

Hence, the measured voltage divided by the source voltage is proportional to the electric field of the AUT, i.e., $V_{RX,n}/V_s \propto \hat{\mathbf{u}}\cdot\mathbf{E}_1$ where $\mathbf{E}_1$ is the electric field of the array exciting the $n-$th antenna only. It should be noted that $V_{RX,n}/V_s$ is fully known (magnitude and phase) through the procedure described in Chapter 2. Equation (B.30) has been used in the inverse source NF-FF transformation to compute the surface equivalent currents $\mathbf{J}^0_{s,1}$ and $\mathbf{M}^0_{s,1}$ ($\mathbf{E}_1$ depends on $\mathbf{J}^0_{s,1}$ and $\mathbf{M}^0_{s,1}$ through radiation integrals, see Section B.5).

As a further development, (B.27) could be implemented in order to compute the unknown equivalent currents from UAV-based measurements. In this case, the pattern of the UAV-mounted source antenna could be taken into account in the inversion process resulting in a more accurate NF-FF transformation (still not demonstrated).

B.5 Inverse Source NF-FF Transformation: numerical implementation

In this Section, the numerical implementation of the inverse source NF-FF transformation is discussed. For the sake of readability, the field $\mathbf{E}_1$ is here denoted with $\mathbf{E}$ and represents the unknown field produced by an array element. Aim of the inverse source algorithm is to obtain the desired electric field $\mathbf{E}$ through equivalent currents defined over a virtual surface S. For this purpose, (B.30) has been used to compute such unknown currents. The electric field $\mathbf{E}(\mathbf{r}_m)$ along the UAV-dipole direction $\hat{\mathbf{u}}(\mathbf{r}_m)$ on the set of measurement points $\{\mathbf{r}_m \quad , m = 1,...,M\}$ is extracted from the UAV-based measurements by (B.30) ($\mathbf{r}_m$ are points of the UAV path and $\hat{\mathbf{u}}$ is a unit

[9] Note that it is hard to make a physical interpretation of the equality $(\mathbf{I}_{TX})_m = I_{TX}\delta_{mn}$. It seems that the n-th array element is feeded with a current I_{TX} whereas the other elements are loaded with an open circuit. However, because $\mathbf{V}_{TX} = \mathbf{Z}_A\mathbf{I}_{TX}$ hence $(\mathbf{V}_{TX})_m = Z_A I_{TX}\delta_{mn}$. This could be read as the n-th array element is feeded with a voltage $Z_A I_{TX}$ and the other elements are closed on a short circuit. This contradiction arises from the hypotheses that $\mathbf{Z}_A = Z_A\mathbf{I}$, i.e., all elements are de-coupled. Once assumed de-coupled array elements in RX mode, it is not possible to restore coupling in TX mode. In conclusion, $\mathbf{E}_1$ is defined as the electric field of the array with the n-th element feeded. Using this model with de-coupled elements, impedance loads on the other elements do not affect the field $\mathbf{E}_1$, because $\mathbf{E}_1$ is the electric field of the n-th element treated as a single element (not embedded in the array).

vector). For the sake of readability, equivalent currents $\mathbf{J}^0_{s,1}$ and $\mathbf{M}^0_{s,1}$ are denoted with $\mathbf{J}$ and $\mathbf{M}$, respectively. Such currents must satisfy two conditions. First, $\mathbf{J}$ and $\mathbf{M}$ must radiate the measured field $\mathbf{E}\cdot\hat{\mathbf{u}}$ over $\{\mathbf{r}_m \quad , m = 1,...,M\}$. Furthermore, the field radiated by $\mathbf{J}$ and $\mathbf{M}$ inside S must be null. The electric field $\mathbf{E}$ is linked to currents $\mathbf{J}$ and $\mathbf{M}$ through radiation integral operators, i.e.,

$$\mathscr{L}(\mathbf{J})(\mathbf{r}) + \mathscr{K}(\mathbf{M})(\mathbf{r}) = \mathbf{E}(\mathbf{r}) \tag{B.31}$$

where $\mathscr{L}$ and $\mathscr{K}$ are radiation operators of electric and magnetic currents, respectively. Hence, enforcing equality between the radiated field on measurement points $\mathbf{r}_m$ along $\hat{\mathbf{u}}$ and the measured field, one obtains

$$\hat{\mathbf{u}}(\mathbf{r}_m)\cdot\left[\mathscr{L}(\mathbf{J})(\mathbf{r}_m) + \mathscr{K}(\mathbf{M})(\mathbf{r}_m)\right] = \hat{\mathbf{u}}(\mathbf{r}_m)\cdot\mathbf{E}(\mathbf{r}_m) \quad \forall m = 1,...,M \tag{B.32}$$

In order to improve the inverse source algorithm, a set of weights $w_m \in \mathbb{R}$ is used

$$w_m\,\hat{\mathbf{u}}(\mathbf{r}_m)\cdot\left[\mathscr{L}(\mathbf{J})(\mathbf{r}_m) + \mathscr{K}(\mathbf{M})(\mathbf{r}_m)\right] = w_m\,\hat{\mathbf{u}}(\mathbf{r}_m)\cdot\mathbf{E}(\mathbf{r}_m) \quad \forall m = 1,...,M \tag{B.33}$$

Considering a triangular tessellation of the surface S, currents $\mathbf{J}$ and $\mathbf{M}$ are approximated as linear combination of Rao Wilton Glisson (RWG) basis functions of order zero [78], i.e.,

$$\mathbf{J} = \sum_{n=1}^{N} j_n\mathbf{f}_n \qquad \mathbf{M} = \sum_{n=1}^{N} m_n\mathbf{f}_n \tag{B.34}$$

In this way, (B.33) can be stated as

$$\mathbf{WTx} = \mathbf{WE} \tag{B.35}$$

where $\mathbf{x}$ contains the unknown coefficients j_n and m_n, the matrix $\mathbf{T}$ is derived by $\mathscr{L}$ and $\mathscr{K}$ whereas matrix $\mathbf{W}$ is the diagonal matrix containing the weights $(\mathbf{W})_{mm} = w_m$. It should be noted that (B.35) is not the final linear system that will be solved. Currents $\mathbf{J}$ and $\mathbf{M}$ must satisfy Love's condition (null field inside S), i.e.,

$$\mathscr{L}(\mathbf{J})(\mathbf{r}) + \mathscr{K}(\mathbf{M})(\mathbf{r}) = \mathbf{0} \tag{B.36}$$

$\forall \mathbf{r}$ inside the surface S. This equation is discretized in the matrix vector multiplication (see the theoretical remark below for the details)

$$\mathbf{T}_L \mathbf{x} = \mathbf{0} \tag{B.37}$$

Finally, conditions (B.35) and (B.37) can be casted in a single linear system

$$\mathbf{A}\mathbf{x} = \mathbf{b} \tag{B.38}$$

where $\mathbf{A} = [\mathbf{T}_L; \mathbf{WT}]$ and $\mathbf{b} = [\mathbf{0}; \mathbf{WE}]$ with $\mathbf{A} \in \mathbb{C}^{(N+M)\times 2N}$ and $\mathbf{b} \in \mathbb{C}^{N+M}$. Once solved (B.38) in a least squares sense, equivalent currents $\mathbf{J}$ and $\mathbf{M}$ are known. The FF pattern of the AUT is hence computed through radiation integrals of such currents.

Theoretical remark (choice of inner surface for Love's condition): Love's condition must be enforced, i.e., the field radiated by $\mathbf{J}$ and $\mathbf{M}$ must be null inside S. An arbitrary closed surface Q completely enclosed by S is considered. It should be noted that if the tangential electric field is zero on Q, then the electric field inside Q must be zero (if the considered frequency f_0 is not a resonance for the cavity Q). Moreover, enforcing null field inside Q is equivalent to enforce null field inside S. This is because if the field is null inside S then it is null inside Q (trivial). However, the converse is also true. If the field is null inside Q, from the analicity of the electric field inside S (see appendix A), then the electric field must be null everywhere inside S. In conclusion, the choice of the surface Q where tangential null field is enforced is theoretically arbitrary. In fact, an arbitrary (but closed) surface Q inside S can be chosen. However, a proper choice of Q is fundamental from a numerical point of view.

In order to enforce null field inside S, the surface $Q = S_\tau$ is defined in the following part. Consider the normal (outward pointing) unit vector $\mathbf{n}$ to the surface S. Chosen a positive $\tau > 0$, the surface S_τ is defined as:

$$S_\tau = \{\mathbf{x} - \tau\,\mathbf{n}(\mathbf{x}), \quad \mathbf{x} \in S\} \tag{B.39}$$

A null tangential field is enforced over S_τ. This is equivalent to enforce that the field is null inside S_τ and then the field must be null everywhere inside S. Considering a triangular mesh over S_τ with RWGs $\{\mathbf{g}_n, n = 1, ..., N\}$, next condition is considered

$$(\mathscr{L}(\mathbf{J}) + \mathscr{K}(\mathbf{M}), \mathbf{g}_n) = 0 \quad \forall n = 1, ..., N \tag{B.40}$$

where the symmetric product is defined as $(\mathbf{f},\mathbf{g}) = \int_{S_\tau} \mathbf{f}\cdot\mathbf{g}\, ds$. In this way, (B.37) is obtained. The choice of τ is dictated by the considered wavelength λ (e.g., $\tau = \lambda/10$ [96]). It should be noted that the choice $\tau > 0$ allows to avoid singularities in the test integral (B.40).